論文 / 著書情報
Article / Book Information

題目(和文)	
Title(English)	Toward Formation of Rocky Planetesimals: Evolution of Local Dust-Gas Density Structure and Growth of Dust Particles at Radial Pressure Bump in Protoplanetary Disks
著者(和文)	瀧哲朗
Author(English)	Tetsuo Taki
出典(和文)	学位:博士(理学), 学位授与機関:東京工業大学, 報告番号:甲第10265号, 授与年月日:2016年6月30日, 学位の種別:課程博士, 審査員:井田 茂,長井 嗣信,綱川 秀夫,中本 泰史,野村 英子
Citation(English)	Degree:Doctor (Science), Conferring organization: Tokyo Institute of Technology, Report number:甲第10265号, Conferred date:2016/6/30, Degree Type:Course doctor, Examiner:,,,,
学位種別(和文)	博士論文
Type(English)	Doctoral Thesis

Toward Formation of Rocky Planetesimals: Evolution of Local Dust-Gas Density Structure and Growth of Dust Particles at Radial Pressure Bump in Protoplanetary Disks

Tetsuo Taki

Tokyo Institute of Technology

Acknowledgments

I deeply thank to my supervisor, Shigel Ida. His extensive discussions around my study have been very helpful for this thesis. I am heartily thankful to Masaki Fujimoto, whose encouragement, guidance and support from the initial to the final level enabled me to develop an understanding the subject. I would like to express my gratitude to Satoshi Okuzumi. His suggestions were invaluable. I would also like to thank Taishi Nakamoto. He gives insightful comments and suggestions. Lastly, I owe thanks to my friend and my family. Without their support, it would have been impossible for me to finish my thesis.

Abstract

We investigate the simultaneous evolution of dust and gas density profiles at a radial pressure bump located in a protoplanetary disk. In addition, we include the effect of the dust growth to the dust and gas dynamics self-consistently. In a framework where dust particles are treated as test particles, a radial pressure bump has been known to trap dust particles that drift radially inward otherwise under non-zero pressure support in a gas disk. As the dust particles are concentrated at the gas pressure bump, however, the drag force from dust to gas, which is ignored in a test-particle approach, may deform the gas profile. Indeed we find that the pressure bump is completely deformed by the dust drag force when the dust-to-gas mass ratio reaches ~ 1 in the case of slower bump restoration. Direct gravitational instability of dust particles is inhibited by the bump destruction. In the dust enriched region of the dust-to-gas mass ratio ~ 1, the radial pressure support becomes $\sim 10 - 100$ times smaller than the global value set initially. Although the pressure bump is a favorable place for streaming instability (SI), the flattened pressure gradient inhibits SI from forming large particle clumps corresponding to $100 - 1000$ km-sized bodies, which has been previously proposed. If streaming instability occurs there, the dust clumps formed would be $10 - 100$ times smaller than previously thought. The estimated size of the resultant planetesimal is $\sim 1 - 100$ km. On the other hand, the dust dense region which has small pressure gradient and relatively high dust-to-gas ratio is favorable location for the direct sticking of dust particles. We conduct simplified 1-D simulations which include effects of dust growth. We confirm that the dust dense region formed by the radial pressure bump encourages the dust growth. Dust particles quickly pass the size corresponding to $\mathrm{St} = 1$ at the pressure bump, and the gas drag law also changes into Stokes law. Even if the dust dense region is destroyed by the global disk evolution, the growth timescale of such dust particles is smaller than the radial drift timescale in the nominal minimum mass solar nebula model. Therefore a pressure bump may be a good location for the formation of *classic* planetesimals due to streaming instability or direct sticking.

Contents

Chapter 1

Introduction

1.1 Difficulties in Planetesimal Formation

It is conventionally considered that planetesimals are building blocks of planets. However, the processes where dust grains in a protoplanetary disk grow to become planetesimals are poorly understood. There are many theoretical difficulties in understanding the planetesimal formation processes.

The radial drift barrier is one of the most serious problems. The disk is at hydrostatic equilibrium, in which the pressure and the centrifugal force balance against the gravity of the central star. Therefore the dust particles under Keplerian motion feel the gas flow as a headwind. The dust particles lose their angular momentum and drift inward due to gas drag (Whipple 1972; Adachi et al. 1976; Weidenschilling 1977). Model calculations show that the time scale for dust growth is significantly slower than the radial inward drift and dust particles are lost from the disk.

There have been many ideas to bypass the radial drift barrier. A straightforward one is rapid formation of planetesimals. Recently, evolution of internal density of dust aggregates during collisional growth was considered and it has been proposed that fluffy aggregates may grow quickly to become icy planetesimals (Okuzumi et al. 2012; Kataoka et al. 2013b,a). Another mechanism for rapid planetesimal formation is strong particle clumping by the Streaming Instability (SI; Youdin and Goodman (2005); Youdin and Johansen (2007); Johansen and Youdin (2007)). The SI is excited by dust inward radial drift due to gas pressure support. The instability modulates the spatial pattern of dust density and forms many dust clumps. When concentrated enough, due to self-gravity, these dust clumps may become planetesimals. Note that the SI does not work for small dust grains. The growth rate of SI is at its greatest when the particles are frictionally coupled with the gas on an orbital time scale. For instance, particles with a radius of 30 cm are most favorable for SI growth at the orbital distance $r = 5$ AU in the minimum mass solar nebula (MMSN; Hayashi et al. (1985)) model (Johansen and Klahr 2011).

Intercepting the dust radial drift is another class of ideas to bypass the radial drift barrier. When a protoplanetary disk has a local pressure maximum, called “radial pressure bump”, dust particles are trapped at the point where the pressure is radially maximized (Whipple 1972; Haghighipour and Boss 2003b,a). Radial pressure bumps are considered to form at some parts of protoplanetary disks, e.g. a disk inner edge, a dead zone inner edge, and an evaporation front of water ice (Johansen et al. 2014). By recent sub-millimeter observations, some protoplanetary disks have asymmetric dust profile (Casassus et al. 2013; Pérez et al. 2014), some of which are considered as candidates of a radial pressure bump (van der Marel et al. 2013).

It should be mentioned that the back-reaction of the drag force from dust onto gas, plays a critical role but has not been taken into consideration in many of the previous works. The dust drag force may become crucial at the radial pressure bump, but this is not necessarily true in other parts of a protoplanetary disk. A typical dust-to-gas mass ratio in a protoplanetary disk is considered to be ~ 0.01. Since the dust drag force is proportional to the dust-to-gas mass ratio, neglecting the dust drag force is a good approximation for dust and gas motion in a general situation. Indeed, Haghighipour and Boss (2003b,a) considered the disk gas and thus a pressure bump as a steady structure. When a pressure bump accumulates dust particles, however, the dust drag force becomes stronger and eventually the back-reaction from the dust may alter the gas profile (Kato et al. 2012) which is the critical element that determines its capability of trapping dust particles. Therefore to study gas pressure profile evolution is important in understanding dust accumulation processes at a radial pressure bump. It implies that we should investigate the dust and gas motion including the dust drag force self-consistently.

In Kato et al. (2009, 2010, 2012), effects of the back-reaction are partly confirmed. They investigated inhomogeneous growth of magneto-rotational instability (MRI) in a local area embedded in a protoplanetary disk. They found that an inhomogeneous growth of MRI formed a quasi-steady radial pressure bump and meter-sized boulders were trapped at the pressure bump. Then they compared two cases: the case with and without the dust drag. In the case with dust drag, the maximum dust density was significantly lower than the case without dust drag. The drag force, when included, made the gas azimuthal velocity to become close to the Keplerian rotation in the dust dense region, which was not favorable for further concentration of dust particles. Their simulations, however, are computationally expensive and including many complex settings. Then, they could not investigate the long-term evolution of the dust and gas motion. Especially, the gas profile evolution under the pure effect of dust drag (without the effects of MRI) is not clear at present.

The other serious problem for planetesimal formation is the fragmentation barrier. At least in initial phase of the planetesimal formation, the dust grains are grown by the direct sticking. When the relative velocity of dust particles is larger than the critical value, the dust particles undergo the fragmentation rather than the coagulation. Especially, the silicate (rocky) particles have the small critical velocity, i.e., a few cm/s $\sim$ 30 m/s (Guttler et al. 2010; Seizinger and Kley 2013; Kelling et al. 2014; Wada et al. 2011, 2013; Meru et al. 2013), which is smaller than the relative velocities induced in protoplanetary disks. Earth-like planets may be formed by rocky planetesimals. The construction of the rocky planetesimal formation theory is imperative for planetary system formation theory.

In this thesis, we investigate the simultaneous evolution of the dust and gas density profile at a simplified radial pressure bump. For simplicity, we treat the disk gas in the (non-magnetized) hydrodynamic frame work, and set the pressure bump as an initial condition. The initial pressure balance is maintained by the Coriolis force from azimuthal velocity. Then the pressure bump is steady in the absence of the dust drag force, even without the source to have produced the bump (e.g. MRI zonal flows, edges of the MRI dead zone, a snow line, etc.). In the case of Kato et al. (2009, 2010, 2012), MRI turbulence due to radially inhomogeneous external magnetic field is the source to produce the pressure bump and MRI does not occur any more after the bump structure with local rigid rotation is established.

The dust and gas motion are mutually coupled by the drag forces self-consistently. The dust particles tend to be accumulated at the point of the pressure maximum, while the dust accumulation alters the gas pressure profile. Since the altered gas profile also affects the dust motion, the simultaneous evolution of the dust and gas dynamics must be investigated. In addition, the self-consistent approach enables us to consider effects of the SI. Since the SI becomes more effective at the dust dense region (e.g., Youdin and Johansen (2007); Johansen and Youdin (2007)), the pressure bump is expected to be a good candidate location for the growth of the SI.

Further more, we also include the dust growth process to the dynamics of dust and gas self-consistently. The dust growth affects the dust motion because of the change of the aerodynamic properties of dust particles. On the other hand, the dust and gas density evolution affect the dust growth due to the variation of the dust density distribution. Therefore these two processes evolve by mutually affected. Especially at the pressure bump, dust particles are trapped and the dust density increases. The pressure bump may encourage the collisional growth of dust particles.

The structure of this thesis is as follows. We first explain the basics for our study in following subsections of this chapter. In Chap. 2, we unveil the mechanisms of bump deformation and formation of dust dense region. We also investigate the property of the streaming instability in the dust dense region. Chap. 3 shows the effect of the vertical inhomogeneity of dust layer on the dust and gas motion at the pressure bump. In Chap. 4, we show the results of simulations including dust growth in the dynamics of dust and gas. Chap. 5 is a general discussion and Chap. 6 is the summary of the thesis.

1.2 Dust Dynamics in Protoplanetary Disks

The dust particles moving in the gas flow exchange the momentum with gas in characteristic time. The characteristic time for a dust particles to reduce its relative velocity to the gas is called frictional time $\tau_{\rm f}$. It expresses the degree of coupling between the dust particles and the gas. The frictional time is given by

$$\tau_f = \begin{cases} \dfrac{\rho_{\rm int} a}{\rho_g v_{\rm th}}, & a < \dfrac{9}{4}\lambda_{\rm mfp} \quad \text{(Epstein regime)}, \\ \dfrac{4\rho_{\rm int} a^2}{9\rho_g v_{\rm th}\lambda_{\rm mfp}}, & a > \dfrac{9}{4}\lambda_{\rm mfp} \quad \text{(Stokes regime)}, \end{cases} \tag{1.1}$$

where $\rho_{\rm int}$ is the internal density of the dust particle, v_{th} is the thermal velocity of the disk gas, and $\lambda_{\rm mfp}$ is the mean free path of the disk gas, respectively. The two lows are separated by the dust size against the mean free path of the disk gas $\lambda_{\rm mfp}$. Note that the Stokes drag is for low Reynolds number ${\rm Re} \sim a\Delta v / c_s \lambda_{\rm mfp} \gg 1$. For the case with high Reynolds number, the gas should be treated as the ideal gas, and the frictional timescale is

$$\tau_f = \frac{8\rho_{\rm int} a}{3\rho_g \Delta u}, \tag{1.2}$$

where Δu is the relative velocity between dust and gas.

In this thesis, we use the dimensionless stopping time $\tau_s \equiv \tau_f \Omega$ where Ω is the Keplerian frequency. It is sometimes called the Stokes number St. Now we consider the Epstein and Stokes regime, the Stokes number can be expressed as (Sato et al. 2016)

$$\tau_s = \frac{\rho_{\rm int} a}{\rho_g v_{\rm th}} \max\left\{1,\ \frac{4a}{9\lambda_{\rm mfp}}\right\} = \sqrt{\frac{\pi}{8}} \frac{\rho_{\rm int} a}{\rho_g c_s} \max\left\{1,\ \frac{4a}{9\lambda_{\rm mfp}}\right\}. \tag{1.3}$$

For the MMSN model, we obtain

$$\begin{aligned} \tau_s \approx 1.8 \times 10^{-8} \left(\frac{\rho_{\rm int}}{2{\rm g/cm}^3}\right) \left(\frac{r}{1{\rm AU}}\right)^{3/2} \left(\frac{a}{0.1\mu{\rm m}}\right) \times \\ \max\left\{1, 4 \times 10^{-6} \left(\frac{r}{1{\rm AU}}\right)^{-11/4} \left(\frac{a}{0.1\mu{\rm m}}\right)\right\}. \end{aligned} \tag{1.4}$$

Therefore the dust radius which is the transition between Epstein and Stokes regime is

$$a \approx 2.5\mathrm{cm} \times \left(\frac{r}{1\mathrm{AU}}\right)^{11/4}, \tag{1.5}$$

and the Stokes number is

$$\tau_s \approx 4.5 \times 10^{-3} \left(\frac{r}{1\mathrm{AU}}\right)^{17/4} \left(\frac{\rho_{\mathrm{int}}}{2.0\mathrm{g/cm}^3}\right). \tag{1.6}$$

In Chap. 2 and 3, we fix the radius of dust particles. It means that the particles are only characterized by the Stokes number.

The dust particles and gas have the relative velocities because of the negative pressure gradient in radial direction. We write gas and dust velocity by $\mathbf{v}$ and $\mathbf{u}$, and Keplerian velocity and Kepler angular velocity are represented by v_{K} and Ω. Also, we consider the steady state ($\partial/\partial t = 0$) and the axisymmetric structure ($\partial/\partial\phi = 0$). Then the gas and dust particle's equations of motion are

$$v_r \frac{\partial v_r}{\partial r} + v_z \frac{\partial v_r}{\partial z} - \frac{v_\phi^2}{r} = -\varepsilon \frac{v_r - u_r}{\tau_{\mathrm{f}}} - \frac{GM_*}{r^2} - \frac{1}{\rho_{\mathrm{g}}}\frac{\partial P}{\partial r}, \tag{1.7}$$

$$v_r \frac{\partial v_\phi}{\partial r} + v_z \frac{\partial v_\phi}{\partial z} + \frac{v_r v_\phi}{r} = -\varepsilon \frac{v_\phi - u_\phi}{\tau_{\mathrm{f}}}, \tag{1.8}$$

$$v_r \frac{\partial v_z}{\partial r} + v_z \frac{\partial v_z}{\partial z} = -\varepsilon \frac{v_z - u_z}{\tau_{\mathrm{f}}} - \frac{GM_*}{r^3} z - \frac{1}{\rho_g}\frac{\partial P}{\partial z}, \tag{1.9}$$

$$u_r \frac{\partial u_r}{\partial r} + u_z \frac{\partial u_r}{\partial z} - \frac{u_\phi^2}{r} = -\frac{u_r - v_r}{\tau_{\mathrm{f}}} - \frac{GM_*}{r^2}, \tag{1.10}$$

$$u_r \frac{\partial u_\phi}{\partial r} + u_z \frac{\partial u_\phi}{\partial z} + \frac{u_r u_\phi}{r} = -\frac{u_\phi - v_\phi}{\tau_{\mathrm{f}}}, \tag{1.11}$$

$$u_r \frac{\partial u_z}{\partial r} + u_z \frac{\partial u_z}{\partial z} = -\frac{u_z - v_z}{\tau_{\mathrm{f}}} - \frac{GM_*}{r^3} z, \tag{1.12}$$

where $\varepsilon = \rho_d/\rho_g$ is dust-to-gas density ratio (Nakagawa et al. 1986). In this regard, however, we neglect the second or higher order term of z/r on account of disk thinness, i.e. $r \gg H$. For the moment, we neglect the turbulence and the backreaction of dust particles to gas with $\rho_d \ll \rho_g$. Therefore, the first term in the right hand side in Eq. (1.7) - (1.9) and v_r, v_z are removed. From Equation (1.7),

$$\frac{v_\phi^2}{r} = -\frac{GM_*}{r^2} - \frac{1}{\rho_{\mathrm{g}}}\frac{\partial P}{\partial r}. \tag{1.13}$$

We solve this in term of v_ϕ, then

$$v_\phi = v_{\mathrm{K}}\left(1 + \frac{1}{\rho_g v_{\mathrm{K}}^2}\frac{\partial P}{\partial \ln r}\right)^{\frac{1}{2}} \tag{1.14}$$

$$\approx v_{\mathrm{K}} + \frac{1}{2\rho_{\mathrm{g}} v_{\mathrm{K}}}\frac{\partial P}{\partial \ln r}. \tag{1.15}$$

Then we obtain the difference of the gas angular velocity from the local Keplerian velocity v_{K} with

$$\begin{aligned} \eta_{\mathrm{g}} v_{\mathrm{K}} &\equiv v_{\mathrm{K}} - v_\phi \qquad (1.16) \\ &\approx -\frac{1}{2\rho_{\mathrm{g}} v_{\mathrm{K}}}\frac{\partial P}{\partial \ln r}, \qquad (1.17) \end{aligned}$$

$$\frac{\eta_{\mathrm{g}} v_{\mathrm{K}}}{c_s} \equiv 0.06\left(\frac{r}{1\mathrm{AU}}\right)^{\frac{1}{4}}. \tag{1.18}$$

It shows that the gas azimuthal velocity is slightly slower than the Keplerian velocity because of the pressure gradient.

The sub-Keplerian rotation of the gas drives the dust inward drift. We rewrite the dust velocity as the relative velocity to the Kepler motion $u_\phi = v_{\mathrm{K}} + \delta u_\phi$ and we assume that $|\delta u_\phi|, u_r, u_z \ll v_{\mathrm{K}}$ in Equation (1.10), (1.11). Then the dust velocities derived (Adachi et al. 1976; Weidenschilling 1977) as

$$u_r \approx -\frac{2\eta_{\mathrm{g}}\Omega r}{(1/\tau_{\mathrm{f}}\Omega) + \tau_{\mathrm{f}}\Omega}, \tag{1.19}$$

$$\delta u_\phi \approx -\frac{\eta_\mathrm{g}\Omega r}{1+(\tau_\mathrm{f}\Omega)^2}. \tag{1.20}$$

Hence, the dust particles have the negative radial drift speed. The infall timescale of dust particles is

$$t_\mathrm{infall} \sim \frac{r}{u_r} \sim \frac{1+(\tau_\mathrm{f}\Omega)^2}{\tau_\mathrm{f}\Omega}\frac{1}{\eta_\mathrm{g}\Omega}. \tag{1.21}$$

We rewrite the infall timescale as

$$t_\mathrm{infall} \sim 90 \times \left(\frac{1+\tau_s^2}{\tau_s^2}\right)\left(\frac{\eta}{1.8\times 10^{-3}}\right)^{-1} t_\mathrm{K}. \tag{1.22}$$

The inward migration is fastest when the dust size satisfies $\tau_\mathrm{f}\Omega = 1.0$, and its timescale is $\sim (\eta_\mathrm{g}\Omega)^{-1} \sim 100(r/\mathrm{AU})^{3/2}$ yr.

This short time scale means that the dust particles would be depleted from the protoplanetary disks before planets are formed. The dust growth time is estimated by the growth equation

$$\frac{\mathrm{d}m}{\mathrm{d}t} = f_\mathrm{s}\rho_\mathrm{d}\pi a_\bullet^2 \mathit{\Delta} u, \tag{1.23}$$

where f_s and $\mathit{\Delta} u$ are the probability of sticking between dust particles and the relative velocity of dust velocities. The timescale in which the dust particles grow their size by mutual sticking is

$$t_\mathrm{grow} \sim \frac{\rho_\bullet a_\bullet}{f_\mathrm{s}\varepsilon\rho_\mathrm{g}\mathit{\Delta} u}. \tag{1.24}$$

The dust relative velocity tends to be smaller in the collision between similar size particles. We consider the case of fastest growth which caused by the collision between the dust particles which have different sizes: one is marginally coupling with gas and the other is coupling strongly so that it has the same velocity with gas. If the relative velocity between these particles could estimate the difference of sedimentation velocity $u_z = -\Omega^2\tau_\mathrm{f} z$, which is obtained from equation of motion, the growth timescale of Equation (1.24) is

$$t_\mathrm{grow} \sim \frac{1}{f_\mathrm{s}\varepsilon\Omega}, \tag{1.25}$$

where $\tau_{\rm f} = \rho_\bullet a_\bullet/(\rho_{\rm g} c_s)$, and $z \sim H = c_s/\Omega$. Therefore

$$\frac{t_{\rm infall}}{t_{\rm grow}} \sim \frac{1+(\tau_{\rm f}\Omega)^2}{\tau_{\rm f}\Omega}\left(\frac{f_{\rm s}}{0.1}\right)\left(\frac{\varepsilon}{0.01}\right)\left(\frac{\eta_{\rm g}}{10^{-3}}\right)^{-1}. \tag{1.26}$$

From $t_{\rm infall} \sim t_{\rm grow}$, the dust particles move inward quickly before they increase their own size when $\tau_{\rm f}\Omega$ closes to unity in the process of dust growth. Weidenschilling (1977); Adachi et al. (1976) presented more detailed analysis. This is the well-known problem as the radial drift barrier and the issue needs to be resolve for planetesimal formation.

Dust trapping at the radial pressure bump is one of the promising process to bypass the radial drift barrier (Whipple 1972; Haghighipour and Boss 2003b,a). The radial pressure bump is a local gas pressure enhancement in protoplanetary disks. The radial drift of dust particles is driven by the negative pressure support. The pressure bump, however, has a point of a pressure maximum and a region where the pressure gradient is positive. Because of the pressure profile of the bump, the dust particles trapped at the pressure maximum (Whipple 1972). Detailed explanation of this process is in Sec. 1.4.

Now, we consider the dust drag force which is the backreaction from the dust particles to the gas. We rewrite the motion equations (1.7)- (1.12) with denoting gas and dust velocity relative to Kepler motion by **v** and **u** at the moment as

$$v_r\frac{\partial v_r}{\partial r} + v_z\frac{\partial v_r}{\partial z} - \frac{v_\phi^2}{r} = -\varepsilon\frac{v_r - u_r}{\tau_{\rm f}} + 2\Omega v_\phi + 2\eta_{\rm g} r\Omega^2, \tag{1.27}$$

$$v_r\frac{\partial v_\phi}{\partial r} + v_z\frac{\partial v_\phi}{\partial z} + \frac{v_r v_\phi}{r} = -\varepsilon\frac{v_\phi - u_\phi}{\tau_{\rm f}} - \frac{1}{2}\Omega v_r, \tag{1.28}$$

$$v_r\frac{\partial v_z}{\partial r} + v_z\frac{\partial v_z}{\partial z} = -\varepsilon\frac{v_z - u_z}{\tau_{\rm f}} - \Omega^2 z - \frac{1}{\rho_{\rm g}}\frac{\partial P}{\partial z}, \tag{1.29}$$

$$u_r\frac{\partial u_r}{\partial r} + u_z\frac{\partial u_r}{\partial z} - \frac{u_\phi^2}{r} = -\frac{u_r - v_r}{\tau_{\rm f}} + 2\Omega u_\phi, \tag{1.30}$$

$$u_r\frac{\partial u_\phi}{\partial r}+u_z\frac{\partial u_\phi}{\partial z}+\frac{u_r u_\phi}{r}=-\frac{u_\phi-v_\phi}{\tau_{\rm f}}-\frac{1}{2}\Omega u_r, \tag{1.31}$$

$$u_r\frac{\partial u_z}{\partial r}+u_z\frac{\partial u_z}{\partial z}=-\frac{u_z-v_z}{\tau_{\rm f}}-\Omega^2 z. \tag{1.32}$$

Then, with the approximation that $|\mathbf{v}|, |\mathbf{u}| \ll |v_{\rm K}|$, velocities of the gas and dust particles are

$$v_r=\frac{2\varepsilon\tau_{\rm f}\Omega}{(1+\varepsilon)^2+(\tau_{\rm f}\Omega)^2}\eta_{\rm g}v_{\rm K}, \tag{1.33}$$

$$v_\phi=-\left[1+\frac{\varepsilon(\tau_{\rm f}\Omega)^2}{(1+\varepsilon)^2+(\tau_{\rm f}\Omega)^2}\right]\frac{\eta_{\rm g}v_{\rm K}}{1+\varepsilon}, \tag{1.34}$$

$$u_r=-\frac{2\tau_{\rm f}\Omega}{(1+\varepsilon)^2+(\tau_{\rm f}\Omega)^2}\eta_{\rm g}v_{\rm K}, \tag{1.35}$$

$$u_\phi=-\left[1-\frac{(\tau_{\rm f}\Omega)^2}{(1+\varepsilon)^2+(\tau_{\rm f}\Omega)^2}\right]\frac{\eta_{\rm g}v_{\rm K}}{1+\varepsilon}. \tag{1.36}$$

These solutions are derived by Nakagawa et al. (1986), and sometimes called NSH equilibrium solution.

The NSH solution depends on the dust-to-gas ratio. In general situation ($\epsilon \ll 1$), the dust radial drift velocity is almost same with the case with no back-reaction. On the other hand, the higher dust-to-gas ratio decreases the radial speed of the dust particles. Therefore this feature is important in the dust accumulation processes as we perform in Chap. 2.

1.3 Formation Mechanism of Pressure Bump

Pressure bumps are the local and long-lived gas structures in the protoplanetary disk, which are theoretically predicted. The formation mechanism of pressure bumps is unclear at present. There are many candidates for the pressure bump formation process (Johansen et al. 2014, reviewed). In this section, we introduce the theoretical studies for the pressure bump formation.

The magnetorotational instability (Balbus and Hawley 1992, MRI) forms long-lived pressure bumps surrounded by a super-Keplerian/sub-Keplerian zonal flow. It is observed by both local shearing box simulations (Johansen et al. 2009a; Simon et al. 2012) and global simulations (Fromang and Nelson 2005; Lyra et al. 2008a). Dittrich et al. (2013) confirmed that the dust particles are accumulated at the pressure bump by using the test particle approach.

Kato et al. (2009, 2010) suggest the other bump formation process by the MRI. They considered the inhomogeneous growth of the MRI. They set the narrow MRI active region sandwiched by the MRI inactive region. After the MRI turbulence is dissipated, the quasi-steady pressure bump lies near the transition of the MRI active/inactive zone. They confirmed that the dust particles are accumulated at the bump (Kato et al. 2010, 2012). In Kato et al. (2012), they also considered the effect of the dust drag force to the dust accumulation process at the pressure bump. The effect of the dust drag force is discussed more detail in Sec. 2.3.1.

A sudden jump in the global gas accretion rate also forms the pressure bump. The difference in gas accretion rates means the difference in gas surface densities. The steep pressure gradient would exist at the jump of the gas surface density. It seems that the gas accretion of protoplanetary disks is driven by angular momentum redistribution due to a turbulent viscosity. Therefore the edge of the MRI dead zone, where the ionization rate is too low for coupling the disk gas and the magnetic field, is an example of such a jump. Lyra et al. (2008a) showed that the inner and outer edges of the dead zone develop steep pressure gradients as the gas piles up in the low-viscosity region. The inner edge of the MRI dead zone has the pressure transition from low to high. Thus there is the pressure maximum which can trap the dust particles. On the other hand, at the outer edge of the MRI dead zone, there is the pressure transition from high to low and no pressure maximum.

The evaporation front of the water (the water snow line) is also a candidate of the pressure bump formed by the sudden jump of the gas accretion rate.

The particle density changes steeply, and hence the ionization rate changes at the evaporation front of the water. It means that the evaporation front would form the transition of the MRI active/inactive region. Therefore the evaporation front acts as a particle trap similar to the dead zone inner edge (Kretke and Lin 2007; Brauer et al. 2008b; Drazkowska et al. 2013). However the mechanism is not confirmed yet by magnetohydrodynamical simulations.

High-pressure anticyclonic vortices have a similar azimuthal velocity pattern as pressure bumps, hence the vortices concentrate particles in the same manner as pressure bumps (Barge and Sommeria 1995). Such anticyclonic vortices may be formed by the baroclinic instability, which is driven by the global entropy gradient (Klahr and Bodenheimer 2003). However, the baroclinic instability is sensitive to the gas cooling time (Lesur and Papaloizou 2010; Raettig et al. 2013). And the presence of other sources of turbulence may affect the growth of the baroclinic instability (Lyra and Klahr 2011). Hence the expression of the baroclinic instability is not clear yet.

An embedded planet or star in protoplanetary disks forms a gap structure in gas surface density, and an outer edge of the gap structure is a candidate of the pressure bump. Lyra et al. (2008b) found that the edge of the gap formed by the Jupiter-mass planet acts as the pressure bump. It is confirmed that the pressure bump concentrates dust particles very efficiently, though the pressure bump underwent the Rossby wave instability (Lovelace et al. 1999; Li et al. 2000, 2001).

Fig. 1.1 is a sketch of the particle concentration region in a wedge of a protoplanetary disk, which is taken from Fig.7 of Johansen et al. (2014). Red regions represent the MRI active zone, and a blue region represents the MRI dead zone in a nominal protoplanetary disk model. The MRI, the dead zone inner edge, the baroclinic instability, the evaporation front, and the planet gap edge are candidates of the mechanism to form the bump structure in planet formation region.

Fig. 1.2 represents the observation result of the Oph IRS 48 (van der Marel et al. 2013). This object is a candidate of the pressure bump. The observed sub-millimeter-sized particles have the significant asymmetric structure while the micron-size particles have no asymmetry. This divided feature can be explained by the filtration effect of the pressure bump.

Note that differences between pressure bumps formed by various mechanisms are not clear. However, the lifetime of pressure bumps is expected to be at least longer than the radial drift timescale of marginally coupled dust particles. Therefore, if we neglect the back-reaction from dust onto gas, we can regard the pressure bump as being in quasi-steady state of equilibrium during dust trapping process. In this thesis, we do not consider the formation mechanism of the pressure bump but we assume the bump having a comparable size to those in the results of Kato et al. (2009).

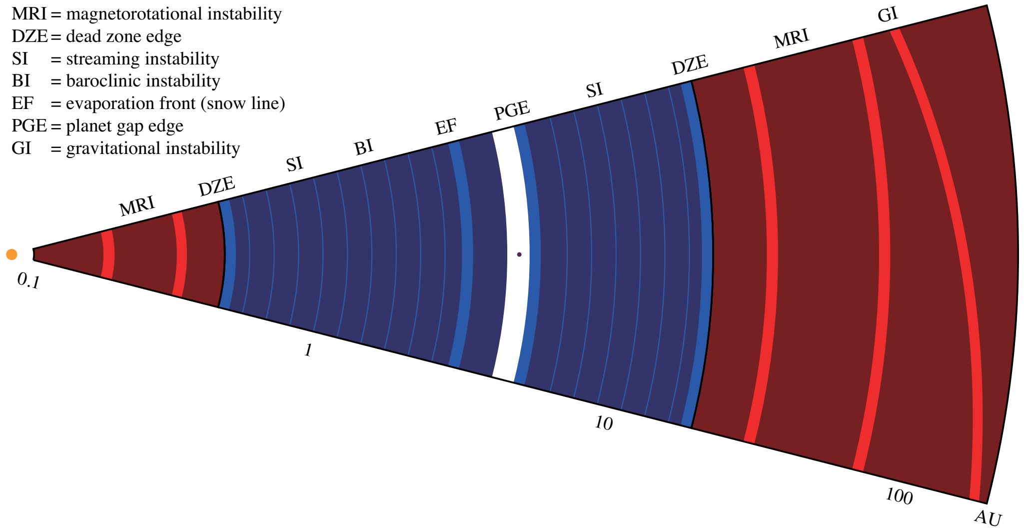

FIGURE 1.1: Sketch of the particle concentration region in a wedge of a protoplanetary disk seen from above. Regions where the magnetorotational instability is expected to be active are marked with red, while the extent of the dead zone in a nominal protoplanetary disk model is marked with blue. In this thesis, we take notice of the pressure bump (or pressure bump like) structure at the planet formation region: the magnetorotational instability, the inner dead zone edge, the baroclinic instability, the evaporation front of water, and the outer side of the planet gap edge. This figure is taken from Figure 7 of Johansen et al. (2014).

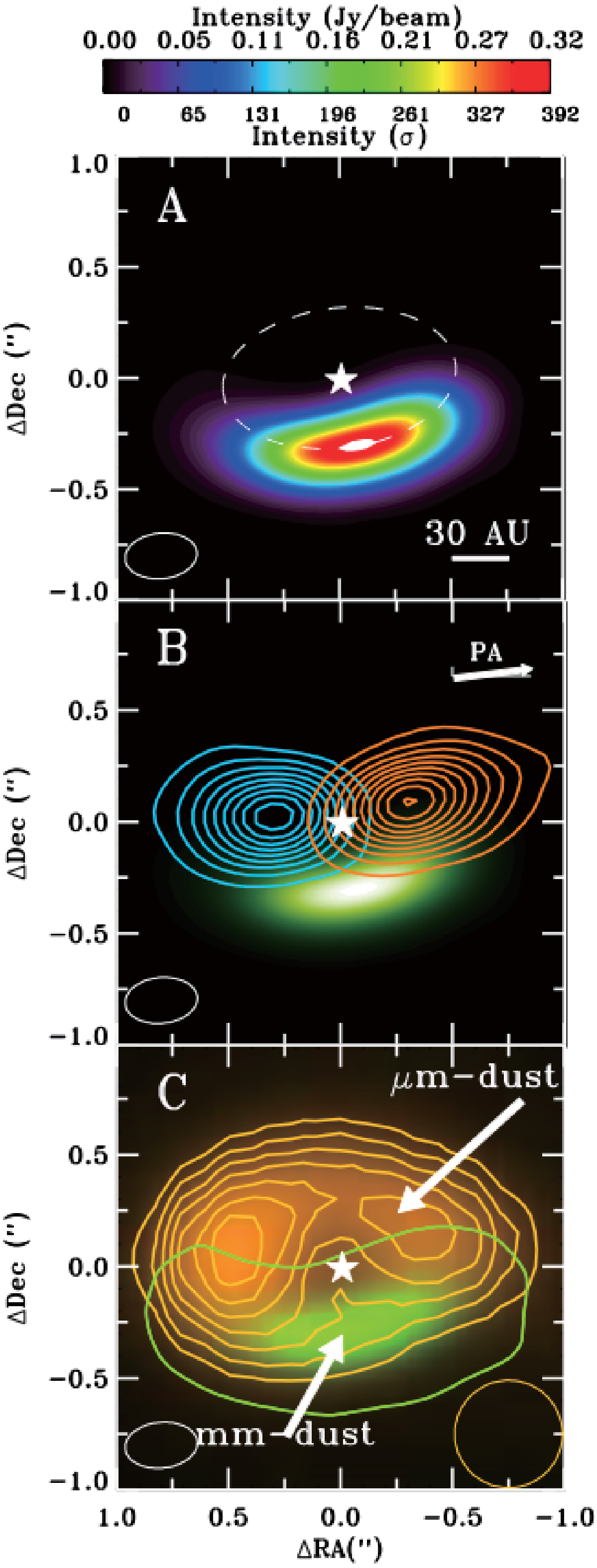

FIGURE 1.2: Dust and gas observations of the inclined disk around IRS 48. (A) the 0.44-mm (685 GHz) continuum emission. The dashed line shows that $r = 63$ AU. (B) The integrated CO 6-5 emission, showing a symmetric gas disk with Keplerian rotation at an inclination $i = 50°$. The green background shows the 0.44-mm continuum. (C) The Very Large Telescope Imager and Spectrometer for the midinfrared (VISIR) 18.7-μm emission in orange contours overlayed on the 0.44-mm continuum in green colors. This figure is taken from Figure 1 of van der Marel et al. (2013)

1.4 Dust Trapping at the Radial Pressure Bump

Dust trapping mechanism by the local gas structure like pressure bump is suggested by Whipple (1972). In general, the disk gas has the negative pressure gradient in radial direction. Then the disk gas rotates at the sub-Keplerian velocity due to the radial pressure support. Since the dust particles feel the gas flow as a "head wind", the dust particles lose angular momentum and move inward radially. If there is the local gas pressure enhancement, the disk has the point of pressure maximum and the region which has the positive radial pressure gradient. In the positive pressure gradient region, the gas rotates as the super-Keplerian flow. Then the dust particles receive the angular momentum and move outward. Finally, the dust particles accumulate at the point of maximum pressure.

Haghighipour and Boss (2003b,a) confirmed the dust trapping by simulation. They conduct the 2-D, 3-D hydrodynamic simulations with dust particles which treated as the test particle approach. In their simulations, the disk gas structure is treated as the steady background. They artificially set the Gaussian pressure bump corresponding to the disk inner edge (see Fig. 1.3). The point of the pressure maximum is at the $r = 1$ AU. Fig. 1.4 shows the time evolution of the dust orbital radius. The dust particles accumulate to $r = 1$ AU at which the gas pressure is maximized.

However the actual dust accumulation process may be more complex. In general protoplanetary disks, the dust-to-gas ratio is considered as ~ 0.01. So the test particle approach is good approximation for the protoplanetary disk. This situation is changed at the radial pressure bump. The concentration of the dust particles means that the inertia of the dust becomes stronger. Finally, the pressure bump becomes the dust dominated region. It means that the dust drag force alter the gas profile. The dust drag force is important in the region where the dust density increases, e.g., the radial pressure bump.

Kato et al. (2012) partly confirm that the maximum dust density becomes lower if the dust drag force is included (see Fig. 1.5). And this bump deformation process is investigated by Taki et al.(submitted). In Sec. 2.3, we also explain the mechanism of pressure bump deformation in detail.

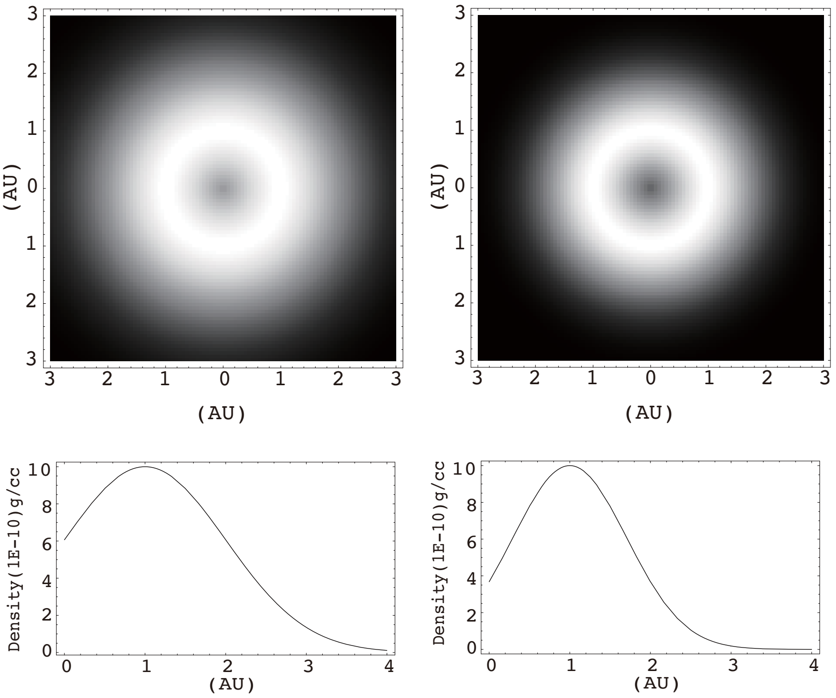

Figure 1.3: Assumed gas density distribution by Haghighipour and Boss (2003b). Top two panels show the contour of the gas density and bottom two panels show the gas density profile from the center to outside. The difference between left and right row is the coefficient for the power of assumed Gaussian gas density profile. This figure is taken from Figure 1 of Haghighipour and Boss (2003b).

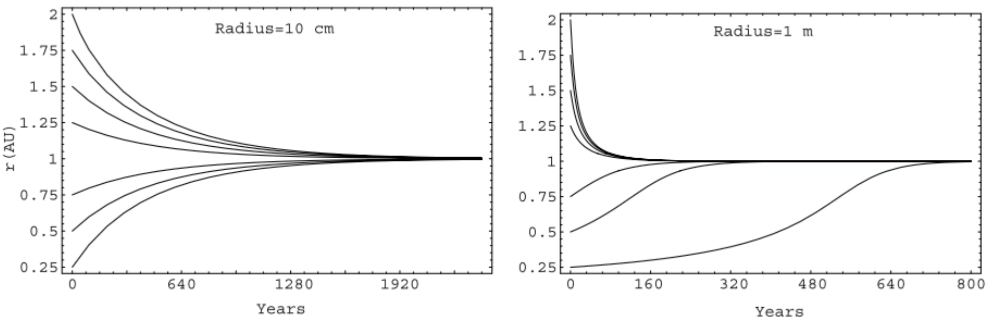

Figure 1.4: Time evolution of the dust orbital radius. The left panel shows the case in which the dust radius is 10 cm, and the right panel shows the case with 1 m. Each lines represent the dust position for various initial orbital radius. This figure is taken from Figure 4 of Haghighipour and Boss (2003b).

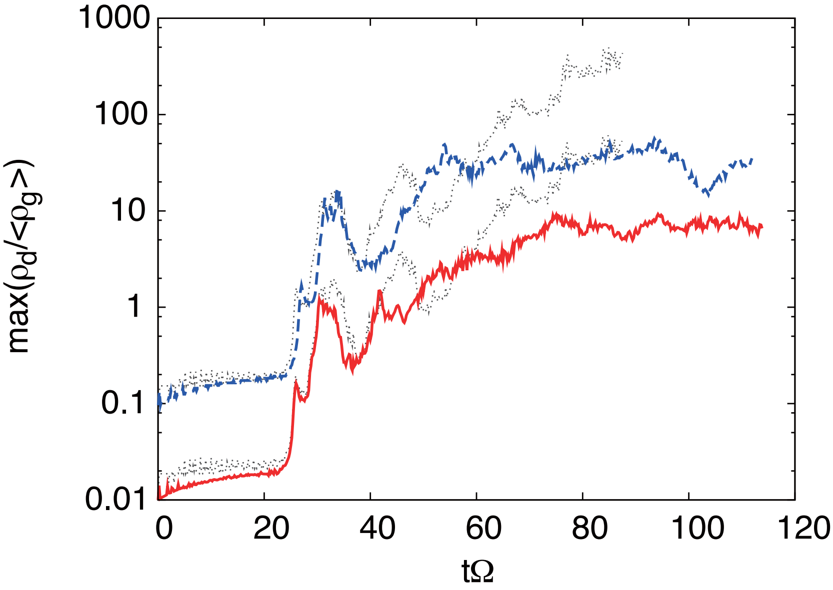

Figure 1.5: Comparison of the maximum dust density between the cases with and without dust drag force. All lines represent the dust density in the cell having the highest density in the whole computational domain, which is normalized by the gas density averaged over the whole region. Upper two lines show the case with $\epsilon_0 = 0.1$ and lower two lines show the case with $\epsilon_0 = 0.01$. The thin dotted lines are results without dust drag force. Blue and red lines are results with dust drag force. This figure is taken from Figure 3 of Kato et al. (2012).

1.5 Streaming Instability

The streaming instability is a linear instability of the dust and gas (Youdin and Goodman 2005; Jacquet et al. 2011). The linear growth of the streaming instability is confirmed by the Johansen and Youdin (2007); Youdin and Johansen (2007) numerically. Johansen and Youdin (2007) also investigate the non-linear growth of the streaming instability. Fig. 1.6 shows that the typical dust density pattern formed by the streaming instability. Fig. 1.7 shows the peak growth rate of the streaming instability as a function of the dust-to-gas ratio. Note that the peak growth rate has the steep gradient at $\epsilon \sim 1$, especially for the case with small stopping time. Fig. 1.8 is the linear growth rate of the streaming instability as a function of radial and vertical wavelength. The wavelengths are normalized by ηr.

Following studies include the more complex effects to the simulation of the streaming instability. Johansen et al. (2009b); Bai and Stone (2010) include the vertical gravity of host star and simplified dust size distribution. Additionally, Johansen et al. (2012) include the effect of the particle collision between the dust particles with in the dense particle clumps. Fig. 1.9 shows that the dust density pattern of the Johansen et al. (2012). The gravitationally bound clumps are formed. These clumps correspond to $\sim 100 - 1000$ km-sized bodies at $r = 3$ AU of the MMSN model. And $30 - 50\%$ of total dust mass is bound by self-gravity.

Drazkowska and Dullemond (2014) investigate whether the streaming instability really occur or not in protoplanetary disks. Fig. 1.10 shows the region where the streaming instability occurs for MMSN model. They argue that the rocky dust particles cannot drive the streaming instability. This is because the rocky particles, which has the small fragmentation velocity, cannot grow to the required size to drive the streaming instability.

Note that properties of streaming instability strongly depend on the particle size, the dust-to-gas mass ratio and the radial pressure support. In pressure bumps, these are drastically changed with these in the nominal MMSN model. Since pressure bumps tend to trap dust particles, it is expected that the pressure bumps are the favorable location for streaming instability. In Sec. 2.3.2, we discuss the detailed properties of streaming instability in the radial pressure bump.

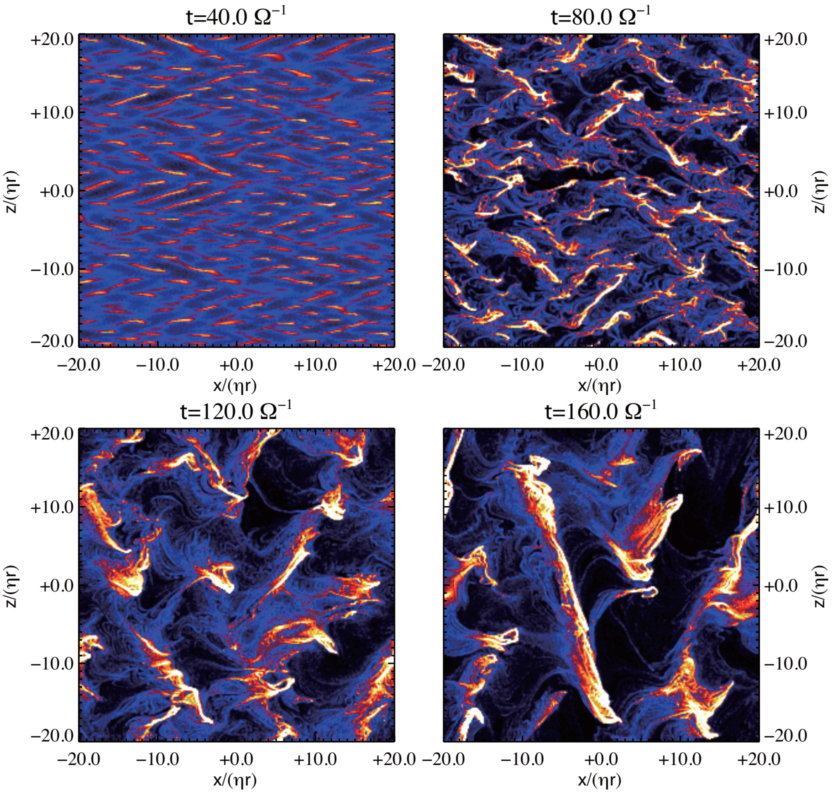

FIGURE 1.6: Snapshots of the dust density pattern produced by the streaming instability at $t\Omega = 40, 80, 120$, and 160. Dust densities increases from black (zero density) to bright yellow/white (dust-to-gas of unity or higher). The calculation is conducted with the dimensionless stopping time $\tau_s = 1.0$ and the dust-to-gas density ratio $\epsilon = 0.2$. At $t\Omega = 40$, the linear growth pattern of the streaming instability is observed. Following panels show that the nonlinear cascade of dense particle clumps into larger filament structures. This figure is taken from Figure 2 of Johansen and Youdin (2007).

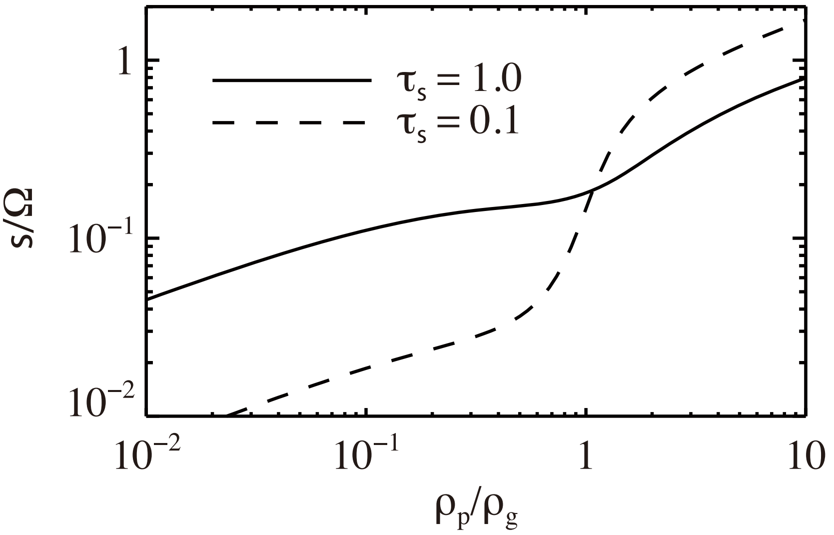

FIGURE 1.7: Peak growth rate s of the streaming instability as a function of the dust-to-gas ratio $\epsilon \equiv \rho_{\mathrm{p}}/\rho_{\mathrm{g}}$ for dimensionless stopping times of $\tau_{\mathrm{s}} = 1.0$ (solid line) and 1.0 dashed line. The steep rise in growth rate is observed when $\tau_{\mathrm{s}} = 0.1$ around $\epsilon = 1.0$. This figure is taken from Figure 1 of Johansen and Youdin (2007).

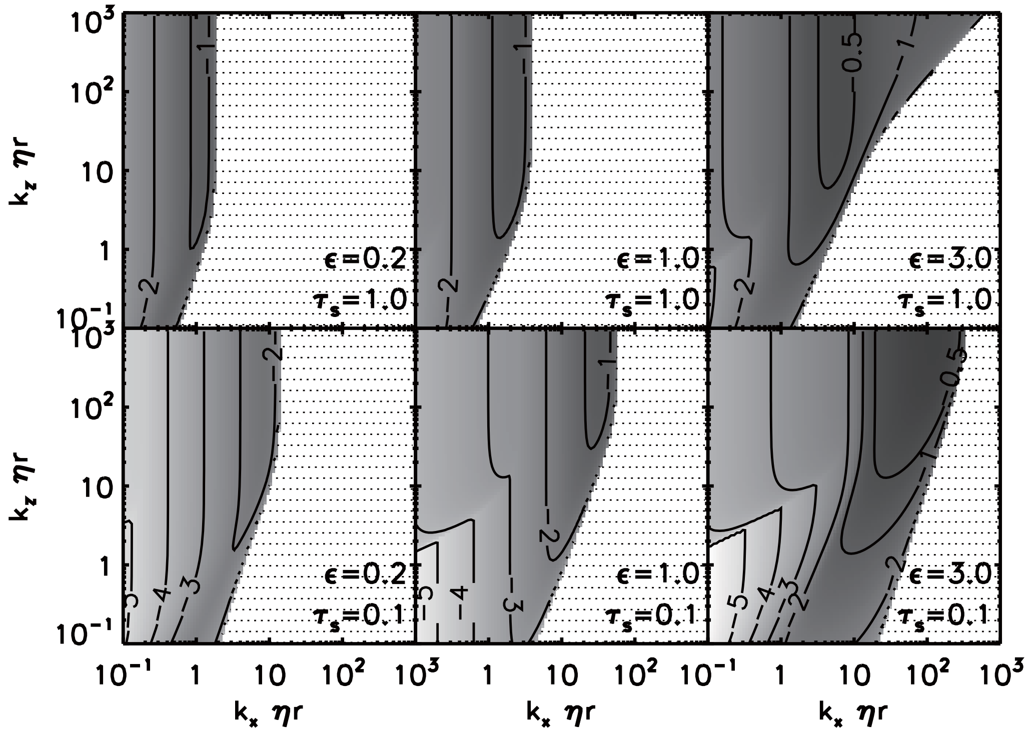

FIGURE 1.8: Linear growth rate s of the streaming instability as a function of the radial and vertical wavenumbers $(k_x\eta r, k_z\eta r)$ for a dimensionless stopping time $\tau_s = 1.0$ (top row) and 0.1 (bottom row). Three values of the dust-to-gas density ratio $\epsilon = 0.2, 1.0$, and 3.0, are considered along the columns. Contours label $\log_{10}(s/\Omega)$, darker shading corresponds to faster growth rates, while the dotted regions contain only damped modes. This figure is taken from Figure 1 of Youdin and Johansen (2007).

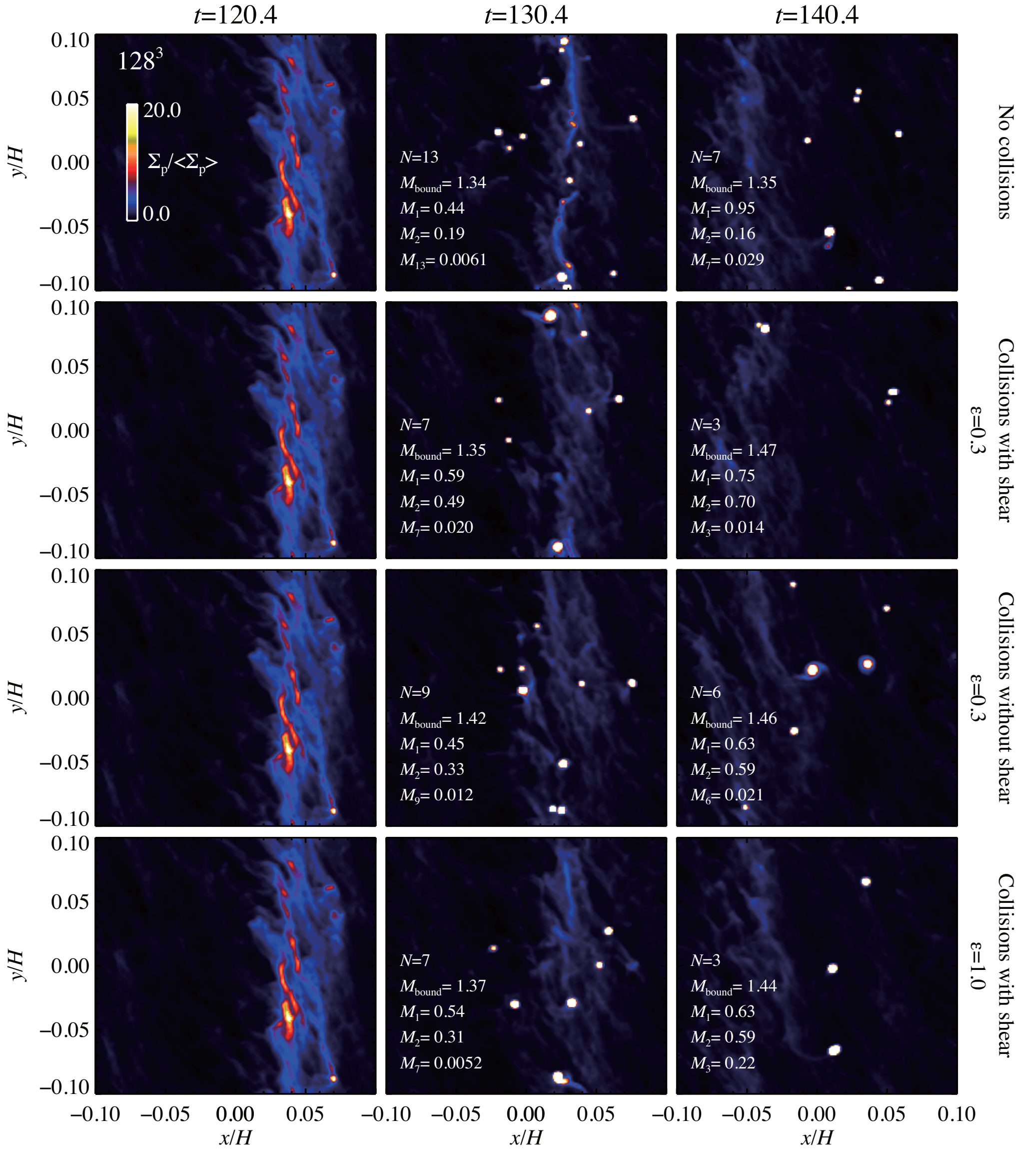

FIGURE 1.9: Snapshots of the dust column density pattern at $t\Omega = 120.4,\ 130.4,\ 140.4$. The dust self-gravity is turned on at $t\omega \sim 119$. An overdense sheet forms by the streaming instability and breaks up in a number of gravitationally bound clumps. In center and right row, the inset numbers represents the number of clumps (N), and the total/individual clump mass ($M_{\rm bound}, M_i$) normalized by the mass of the dwarf planet Ceres. The clumps merge and reduce the number with time in all cases. The energy dissipation due to the collision between particles enhances this tendency. This figure is taken from Figure 12 of Johansen et al. (2012).

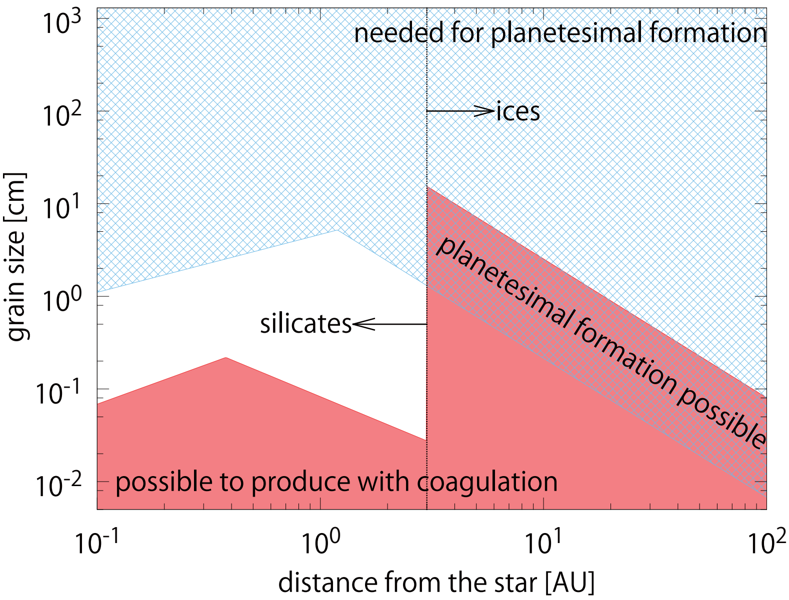

Figure 1.10: Comparison of the maximum dust size produced by coagulation (red shaded region) and minimum dust size required to drive the streaming instability (blue crosshatched region). The particle growth is limited by the relative velocity due to the dust radial drift, ignoring turbulence which corresponds to the dead zone. This figure is taken from Figure 2 of Drazkowska and Dullemond (2014).

1.6 Vertical Width of the Dust Layer

The dust scale height is smaller than the gas scale height, when the dust particles grow. In initial stage of dust growth, the dust particles have small radii. Then the dust particles are well-coupled to the disk gas and have the same scale height with gas. As dust particles undergo the sticking and growth, the dust particles decouple with gas and start settling. In initial stage, settling is faster than the radial drift, sedimentation dominate the dust density evolution (Nakagawa et al. 1986). The dust particles form the thin dust layer which has the high dust density. The classical GI scenario, which consider the thin dust layer gravitationally unstable, expect the infinitesimal settling. However the thin dust layer drags the disk gas, and the azimuthal velocity of the disk gas will have the shear in vertical direction (Weidenschilling 1980). The Kelvin-Helmholtz instability (KHI) is driven in such situation. The KHI turbulence mixes the dust particles.

The vertical width of the dust layer is determined by the equilibrium between the vertical settling and the turbulent diffusion. Carballido et al. (2006) obtained the dust scale height for loose coupling case and Dubrulle (1995) derived the dust scale height for tightly coupled dust particles. Then Youdin and Lithwick (2007) derived the dust scale height including the effect of the orbital oscillation. The scale height of Youdin and Lithwick (2007) is

$$H_{\rm p}^2 = \frac{D_{g,z}}{\Omega\tau_{\rm s}}\frac{1}{\xi}, \tag{1.37}$$

$$\xi \equiv 1 + \frac{\tau_{\rm s}\tau_{\rm e}^2}{\tau_{\rm s}+\tau_{\rm e}}, \tag{1.38}$$

where $D_{g,z} =< w_g^2 > t_{\rm eddy}$. Fig. 1.11 shows that the dust scale height as a function of the $\tau_{\rm s}\Omega$. For turbulence of $\tau_{\rm eddy}\Omega = 1$ and $\alpha_z \equiv D_{g,z}/(H_g^2\Omega)$, we obtain the dust scale height as (Okuzumi et al. 2012)

$$H_{\rm d} = H_{\rm g}\left(1 + \frac{\tau_{\rm s}\Omega}{\alpha_z}\frac{1+2\tau_{\rm s}\Omega}{1+\tau_{\rm s}\Omega}\right)^{-1/2}. \tag{1.39}$$

The α_z is the dimensionless parameter for turbulent diffusion, which is not the same with the Shakura and Sunyaev (1973) α-parameter for diffusion of angular momentum. If the gas diffusion coefficient is of the same order as the turbulent viscosity, α_z is equivalent to the Shakula & Sunyaev α-parameter. For simplicity, we assume that $\alpha_z = \alpha$ in this thesis.

The vertical settling of the dust particles is important to the planetesimal formation process. In the case with no dust settling, Johansen and Youdin (2007) shows that the SI requires the high dust-to-gas mass ratio, $\gtrsim$1, especially for the small dust particles. Johansen et al. (2009b); Bai and Stone (2010) shows that the dust settling drives the strong dust clumping due to the the streaming instability, even if the dust surface density is comparable to the MMSN. Settled dust particles form the thin dust layer at the midplane. This dust layer has the high dust density and drive the strong SI.

In addition, the dust settling may change the pressure bump evolution. The angular momentum redistribution between dust and gas occurs near the disk midplane. We investigate this situation in Chap. 3.

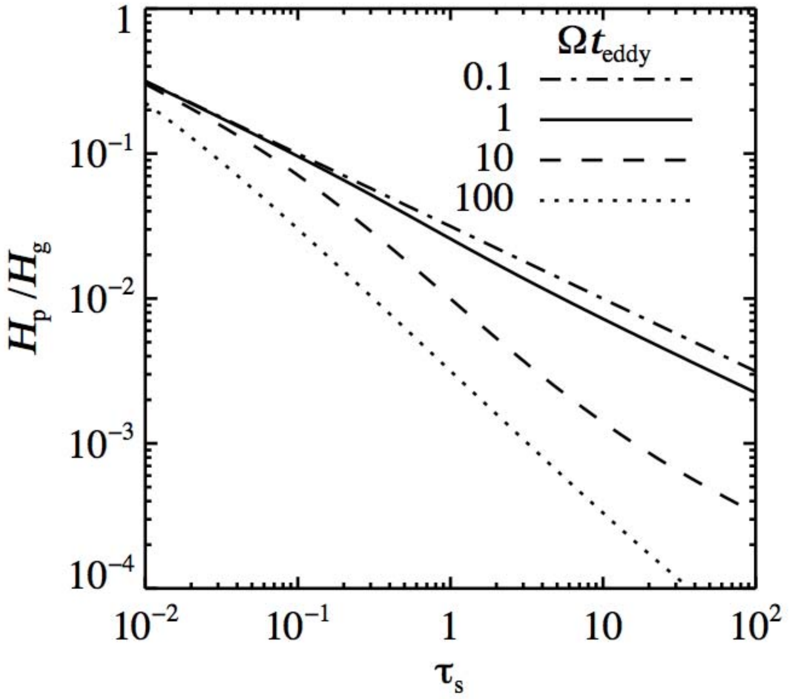

FIGURE 1.11: Particle scale height $H_{\rm p}$ relative to gas as a function of the dimensionless stopping time $t_{\rm s} \equiv t_{\rm f}\Omega$. Different lines show the different eddy turnover times $\omega t_{\rm eddy}$, which is the turnover time of the largest eddy. The turbulent parameter α is 10^{-3}. Note that we assumed that $\Omega t_{\rm eddy} = 1$ in this thesis. This figure is taken from Figure 4 of Youdin and Lithwick (2007).

1.7 Collisional Growth of Dust Particles

Because of the large fragmentation velocity, the icy particles can be formed by the direct sticking or the streaming instability. Okuzumi et al. (2012) show that the fluffy aggregate can grow to icy planetesimals. When the porosity evolution is included, the growth of dust particles faster than the radial drift timescale (Fig. 1.12). Then Kataoka et al. (2013b,a) consider the static compression of fluffy aggregates. They presented the pathway of the dust density evolution which can form the icy planetesimals which have the realistic internal density (Fig. 1.13). On the other hand, Drazkowska and Dullemond (2014) shows that the icy particles can grow to the sizes which can drive the streaming instability. Then they calculate the total planetesimal mass formed by the streaming instability.

On the other hand, the maximum size of rocky dust particles are significantly smaller than the ice due to the small fragmentation velocity. Birnstiel et al. (2012) conduct the evolution of the dust size distribution due to both the coagulation and the fragmentation. Fig. 1.14 shows that the size of dust particles are limited by the fragmentation velocity in inner part of the protoplanetary disk. The maximum size of rocky particles is ~ 1 cm at $r = 1$ AU. By Fig. 1.10, also the streaming instability does not occur at the inner part of the streaming instability.

Taki et al. (submitted) and Chapter 2 of this thesis suggest that the radial pressure bump might solve the this problem. This is because the dust dense region formed by the pressure bump has the small pressure gradient. The dust radial drift velocity becomes small in such region. In addition, the velocity scale of the streaming instability also become small due to the gas density evolution. Therefore the dust dense region formed by the radial pressure bump may be favorable location for the dust coagulation even for the rocky particles.

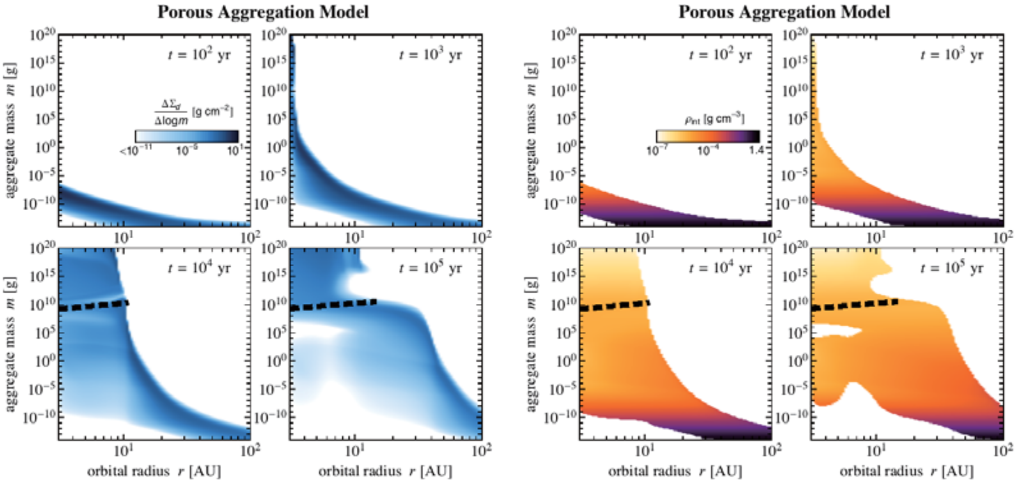

FIGURE 1.12: The snapshots of aggregate size (left four panels) and internal density (right four panels) distributions at $t = 10^2, 10^3, 10^4, 10^5$ yr for icy particles as a function of the orbital radius r and aggregate mass m. The calculation includes the porous aggregation model and radial drift. The dashed lines mark the aggregate size which $t_f\Omega$ is unity. This figure is taken from Figure 5 of Okuzumi et al. (2012).

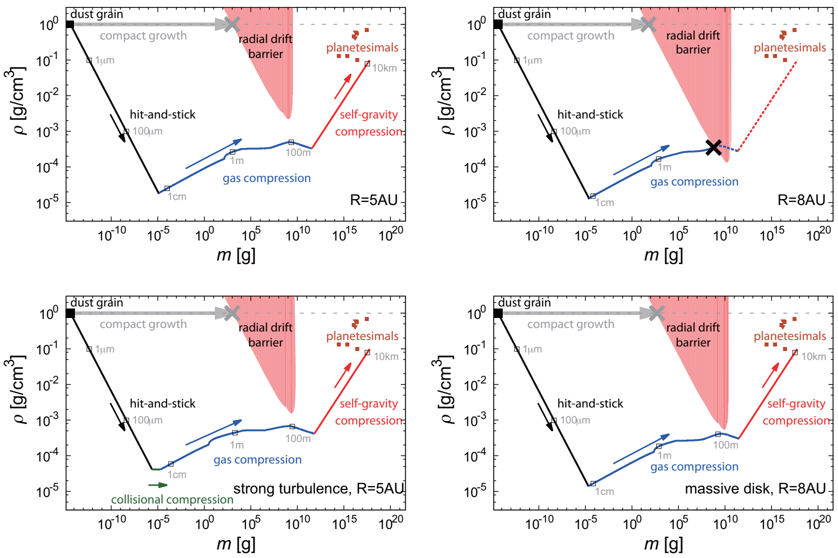

Figure 1.13: Pathways of the dust internal density evolution for icy particles as a function of the aggregate mass at orbital radius $R = 5$AU (left row) and 8AU (right row). The gray line shows the evolutional track of the compact growth. The black, green, blue, and red lines are the evolutional track through dust coagulation via fluffy aggregates. The red shaded region represents where the radial drift timescale is less than the growth timescale, which is equivalent to radial-drift region. The cross point at top right panel represents where the dust falls onto the central star. The disk parameters are assumed as MMSN model and turbulent parameter $\alpha = 10^{-3}$ except for bottom left panel ($\alpha = 10^{-2}$) and bottom right panel (two times as massive as MMSN). This figure is taken from Figure 3 of Kataoka et al. (2013a).

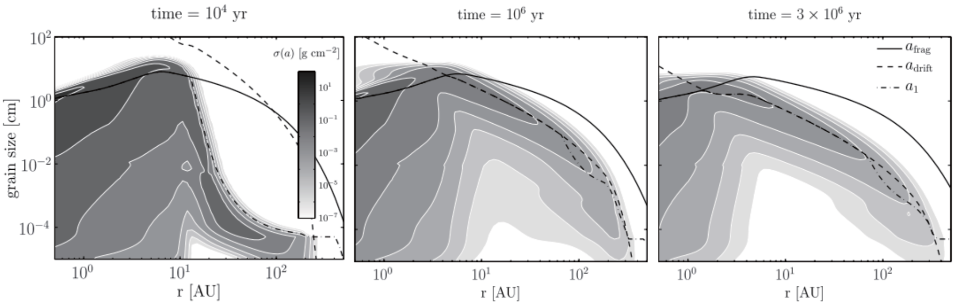

Figure 1.14: Dust surface density distributions including dust coagulation/fragmentation and radial drift as a function of radius r and grain size at 10^4, 10^6,and 3×10^6 years. The turbulence parameter α was taken to be 10^{-3}. Overlayed lines are the representative sizes for a fragmentation limited size distribution (solid black lines) and for a drift limited size distribution (dashed black lines), respectively. This figure is taken from Figure 1 of Birnstiel et al. (2012).

Chapter 2

Dust and Gas Density Evolution at a Radial Pressure Bump

2.1 Method

2.1.1 Basic Equations

We consider a small region around the midplane which is rotating the Keplerian frequency Ω at a distance r from a central star to study local dust motion and hydrodynamics of disk gas. The local Cartesian coordinates are (x, y, z) where x is the radial distance from r, y is tangential distance, and z is vertical distance from the disk midplane. We assume the axisymmetric disk, then we conduct the 1-D (radial) and 2-D (radial-vertical) simulations. The dust and gas move in radial direction due to the angular momentum redistribution, however, we calculate the azimuthal velocities at each grid cell in 1-D or 2-D simulations.

For the disk gas, we use the isothermal hydrodynamic equations,

$$\frac{\partial \rho_g}{\partial t} + \nabla \left(\rho_g \mathbf{v} \right) = 0, \tag{2.1}$$

$$\frac{\partial \mathbf{v}}{\partial t} + (\mathbf{v}\cdot\nabla)\,\mathbf{v} = -\frac{1}{\rho_g}\nabla P + 3\Omega^2 x\hat{\mathbf{x}} - 2\boldsymbol{\Omega}\times\mathbf{v} - \beta c_s \Omega \hat{\mathbf{x}} - \frac{\epsilon}{\tau_f}(\mathbf{v}-\mathbf{w}'), \tag{2.2}$$

$$P = c_s^2 \rho_g, \tag{2.3}$$

where ρ_g is the density of the disk gas, $\mathbf{v}$ is the gas velocity, P is the gas pressure, and c_s is the constant sound speed, $\epsilon = \rho_d/\rho_g$ is the dust to gas mass ratio, respectively. The gas pressure gradient term is separated from global one $-\beta c_s \Omega$. We assume that $\rho_g \propto r^q$, then the global pressure gradient term is

$$-\frac{1}{\rho_g}\frac{\partial P_0}{\partial r} \cong -\frac{1}{\rho_g}\frac{P_0}{r}q \cong -\frac{H}{r}q c_s \Omega = -\beta c_s \Omega, \tag{2.4}$$

where $H = c_s/\Omega$ is the disk scale height. In our local model, $\beta \equiv qH/r = -0.04$ or 0 is approximated to be constant. Then the gas rotation angular velocity is

$$\Omega_g = \Omega\left(1 + \frac{1}{2}\left[\frac{H}{r}\right]^2 \frac{\mathrm{d}\ln P}{\mathrm{d}\ln r}\right) = \Omega\left(1 + \frac{1}{2}\frac{H}{r}\beta + \frac{1}{2}\left[\frac{H}{r}\right]^2 \frac{\mathrm{d}\ln \delta P}{\mathrm{d}\ln r}\right), \tag{2.5}$$

where δP is the local gas pressure which is caused by local density inhomogeneity. The last term of right hand side of Eq.(2.2) is the dust frictional force. The description $\mathbf{w}'$ is the allocated dust velocity at grid point. We use the cloud-in-cell (CIC) model to allocate the averaged dust velocity. We assume that the stopping timescale $\tau_s \equiv \tau_f \Omega = 1.0$ is constant. And dust particles are only characterized by the stopping timescale. The timescale $\tau_s = 1$ means that we consider cases with the dust particles are marginally coupled to gas and with the dust radial drift is fastest (Nakagawa et al. 1986).

We include meter-size dust boulders as super-particles. Total number of the super-particles is $O(10^5 - 10^6)$ and each super-particle represents $O(10^7)$ boulders. The equation of motion of the i-th particle is given by

$$\frac{\mathrm{d}\mathbf{u}_i}{\mathrm{d}t} = -2\boldsymbol{\Omega}\times\mathbf{u}_i + 3\Omega^2 x_i \hat{\mathbf{x}} - \frac{1}{\tau_f}\left(\mathbf{u}_i - \mathbf{v}'_i\right), \tag{2.6}$$

Run	$L_x \times L_z$	$N_x \times N_z$	N_p	β	$T_{\rm end}$
β04-1D	$10.0H \times -$	10000×1	2.7×10^5	-0.04	$500\Omega^{-1}$
β04-2D	$7.5H\times0.25H$	1500×50	1.875×10^6	-0.04	$500\Omega^{-1}$
β00-1D	$4.0H \times -$	4000×1	1.08×10^5	0.0	$500\Omega^{-1}$

TABLE 2.1: Setup of individual runs. L_x, L_z are the radial and vertical width of computational region. N_x, N_z are the grid numbers in radial and vertical direction. N_p is the number of super-particles. β is the global pressure gradient coefficient. $T_{\rm end}$ is the total run time.

where $\mathbf{v}'_i$ is the gas velocity at the location of the i-th particle, which is interpolated using $\mathbf{v}$ at the neighbor grid points.

In simulations, the gas equations are solved by the CIP scheme (Yabe and Aoki 1991),which is one of the method of grid-hydrodynamics. The dust density and velocities are allocated to the closest four (2-D) or two (1-D) grid points in the computational region using cloud-in-cell interpolation. This algorithm strictly conserve angular momentum transfer between the dust and the gas. We use the local simulation box, then the boundary conditions are periodic in all directions. For the radial boundary, however, we use the shearing-box approximation which consider Keplerian differential rotation (Wisdom and Tremaine 1988; Hawley et al. 1995). These methods are similar to Kato et al. (2012).

2.1.2 Initial Conditions

We conduct numerical simulations with three setups. First one is a 1-D (radial) simulation with a bump. In this run, we test the 1-D evolution of the bump in radial direction. Second one is a 2-D (radial-vertical) simulation with a bump. This is the main results of this paper. We investigate the pressure bump evolution and the growth of the SI at the same time. Third one is a 1-D simulation without the global pressure gradient. This setup is the same as the first one except for the global pressure gradient, in order to check the effect of the global pressure gradient on time evolution of the radial pressure bump. Other parameters and settings for the cases are presented in table 2.1. In all type of calculations, we set the pressure bump as the initial condition. Our pressure bump is sustained by the azimuthal velocity profile given by Eq. (2.8). Therefore, the pressure bump is steady if there is no dust frictional force. Note that we do not include the source to have produced the pressure bump for simplicity. This approximation corresponds to the simulation that the timescale to produce the bump structure is longer than the deformation timescale due to dust drag. The expression of pressure bump is

$$P = P_0 \left\{ 1 + a \exp\left(\frac{-x^2}{2h^2} \right) \right\}, \tag{2.7}$$

where a and h is the arbitrary parameter for the height and width of a pressure bump. We set $a = 0.2, h = \sqrt{1/4}H$ in our simulations. And the expression of initial azimuthal velocity profile is

$$v_y = -\frac{3}{2}\Omega x + \frac{1}{2\Omega} \left\{ \beta c_s \Omega - \frac{1}{\rho_g} \frac{a P_0 x}{h^2} \exp\left(-\frac{x^2}{2h^2} \right) \right\}, \tag{2.8}$$

which is derived by the radial force balances. In the 2-D simulation, we assume the uniform distribution in vertical direction because of the narrow computational boxes in that direction.

In all cases, the dust particles rotate as Keplerian flow in whole computational region, initially. The dust density profile is uniform and the initial dust-to-gas mass ratio is $\epsilon = 0.1$. We suppose that the large dust particles settle on midplane, then the initial dust-to-gas mass ration is higher than the ratio in the MMSN. When we start the calculation, the dust particles go to the Nakagawa-Sekiya-Hayashi equilibrium solution (Nakagawa et al. 1986) in a few frictional timescales. And the dust particles drift to the peak of the pressure bump initially. In the regions other than the bump region, the radial drift velocity of the dust particles is (Nakagawa et al. 1986)

$$u_{r,\mathrm{NSH}} = \frac{\tau_f \Omega}{(\tau_f \Omega)^2 + (\epsilon + 1)^2} \beta c_s. \tag{2.9}$$

It is required that the computational box is wide enough to be passed over by the dust particles for computational time. Since the radial drift velocity is $u_{r,\mathrm{NSH}} = -0.018 c_s$ in our 1-D simulation, the drift length is $9H$. In our 2-D simulation, the dust radial velocity decreases by $\sim 40\%$ due to the SI (Johansen and Youdin 2007), the drift length is $\sim 5.4H$. Then the box size in radial direction is $L_x = 10H$(1-D simulations), $7.5H$(2-D simulation) which is larger than the drift length. The vertical box size is $L_z = 0.25H$ which is enough smaller than the disk scale height.

2.2 Results

2.2.1 1-D Dust Density Evolution

First, we describe the 1-D view of the pressure bump evolution. The pressure bump halts inward accreting dust particles at the point of the pressure maximum. If there is no drag force from dust to gas, the pressure bump is steady and the dust density increases unlimitedly at this point, which is the picture in a test-particle approach. When the dust drag is taken into account, the pressure bump is deformed by the angular momentum exchange and the dust particles are not concentrated at the point but are distributed over a radial range.

Figure 1.1 shows that the time evolution of the maximum dust density which is the dust density in the cell having the highest density over the whole computational region. In figure 2.1, the green line represents the result of the run β04-1D. The maximum dust density increases until $t\Omega \sim 10$ due to the dust trapping by the pressure bump. At $t\Omega \gtrsim 10$, the density stops increasing and the saturated dust density is $\sim \rho_0$. The mechanism of this saturation is the same with the 2-D simulation (run β04-2D) or with the simpler 1-D simulation without global pressure (run β00-1D) and will be discussed in subsequent sections.

The dust dense region has the dust-to-gas mass ratio of the order of unity. Although much higher dust-to-gas ratio is required for a simple Toomre-type self-gravitational instability to occur, Johansen and Youdin (2007) suggests that, when two-dimensionality is introduced, the SI makes strong clumping of dust particles in such a dust dense region. That is, a pressure bump is one of the most probable regions where the SI is excited and dust clumps are formed. In our simulations to be described in the next subsection, however, the behavior of the SI is found to be different from previously studied cases due to the pressure bump deformation.

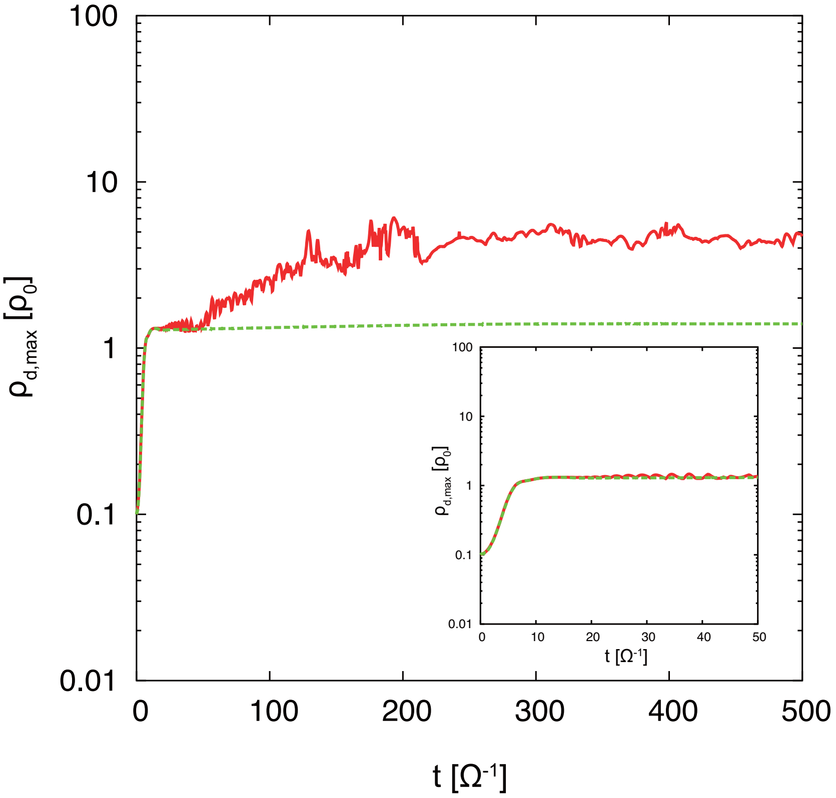

FIGURE 2.1: Time evolution of the maximum dust density in run β04-2D (2-D w/ bump; red line) and β04-1D (1-D w/ bump; green dashed line). All the lines represent the dust density in the cell having the highest density over the whole computational region, normalized by the background gas density ρ_0. The initial dust accumulation due to the bump structure is almost the same in the two runs (see inset).

2.2.2 2-D Dust Density Evolution

From 2-D simulation results, we confirm the formation of the dust dense region due to the dust trapping and growth of the SI in the dust dense region. Figure 2.2 shows snapshots of the dust density profile at the bump. In panel (a, b) of figure 2.2, which are the snapshots at $t\Omega = 50, 100$, the dust dense region is formed by the radial pressure bump. The region has a nearly unity dust-to-gas mass ratio as in the 1-D simulation. In panel (c), we can see the density spatial pattern that indicates the linear growth of the SI. In panel (d), the saturated state of the instability is shown. There are some large dust clumps whose densities are over $2\rho_0$.

In figure 2.1, the red line shows the time evolution of the maximum dust density in the whole computational region from the 2-D simulation. Until $t\Omega \sim 50$, the maximum dust density evolves as in the 1-D case. Then, the red line surpasses the green one indicating that the linear growth of SI is started. The dust concentration is saturated by $t\Omega \sim 200$, with the maximum dust density converging at $\sim 5\rho_0$. On the other hand, in Johansen and Youdin (2007), the maximum dust density created by clumping by the SI is $\sim 100\rho_0$. In this other case, initially uniform dust density of $\sim \rho_0$ is distributed over the whole computational domain. Our maximum density is quite low compared with the value obtained from the other case even though the dust-to-gas ratio that excites the SI is equally high ~ 1. The reason for this weaker clumping in our case will be discussed in subsequent sections.

Figure 2.3 shows the snapshot of the vertically averaged or maximum values of dust and gas densities from the 2-D result at $t\Omega = 500$. The orange and the pink lines show the maximum and the vertically-averaged dust density at each radial location, respectively. The deviation between the orange and the pink lines shows that the SI is excited throughout the dust dense region. The averaged dust density at the pressure bump is $\sim \rho_0$ and is almost the same with the 1-D results. It means the basic dust density radial structure is due to the 1-D dynamics and the SI adds modulation along the vertical direction.

The blue and the cyan lines in figure 2.3 show the vertically averaged and maximum gas densities at each radial location, respectively. There is small difference between the two implying that the SI does not result in strong vertical variation of gas density.

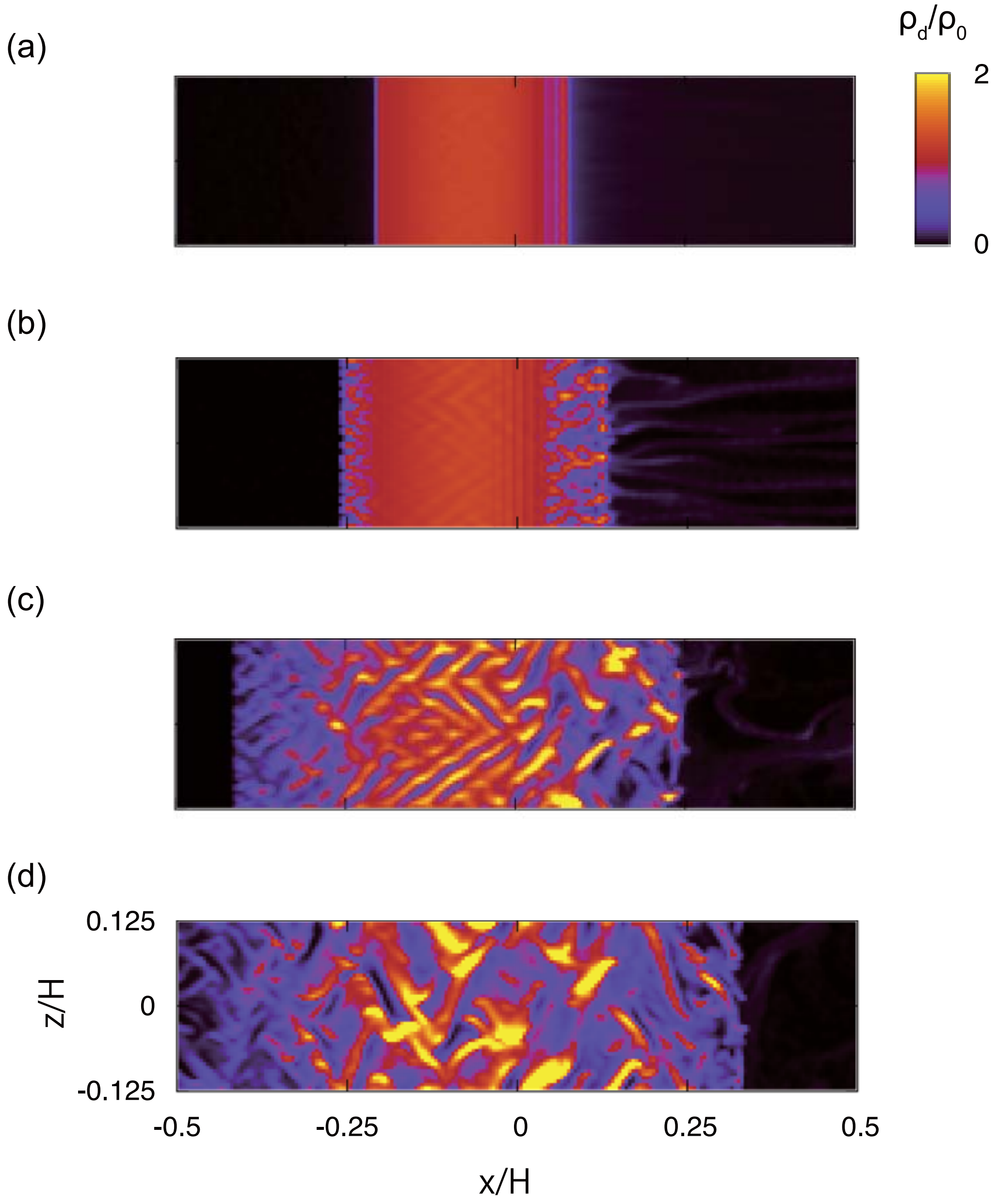

Figure 2.2: Dust density pattern obtained from run β04-2D (2-D w/ bump). Each panels represent the snapshot at (a) $t\Omega = 50$, (b) 100, (c) 250, (d) 500, respectively. Dust densities increase from black (zero density) to bright white ($\rho_d = 2\rho_0$). Initially, the pressure bump makes the dust particles to concentrate with the dust-to-gas mass ratio being nearly unity (panel (a)). Subsequent panels show the growth of the SI in this dust dense region. Note that the region near the pressure bump is zoomed-in and the whole computational domain is wider in radial direction.

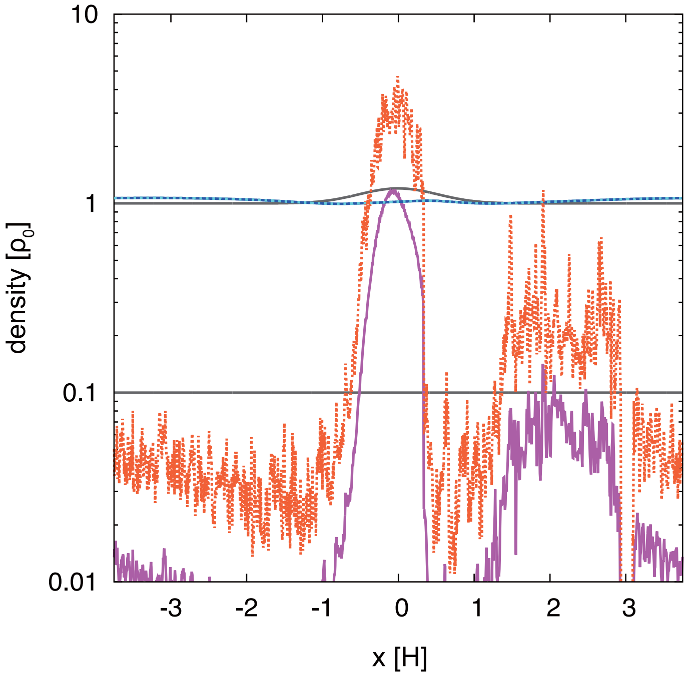

Figure 2.3: The dust and gas density radial profile from run β04-2D (2-D w/ bump). Each line is a snapshot at $t\Omega = 500$. Gray solid lines show the initial profile of gas (upper line) and dust (lower line) densities. The orange dotted line and the pink solid lines show the maximum and vertically-averaged dust densities at each x. The vertically averaged dust density stays ~ 1 as in the 1-D run, while the upward deviation of the orange line from the pink one shows the growth of SI in the 2-D case. The cyan solid and blue dotted lines showing the gas densities (maximum and vertically-averaged, respectively) show small differences implying that the gas density has a nearly uniform distribution in the vertical direction.

2.2.3 Evolution of the Gas Pressure Profile

In our simulations, the evolution of the local gas pressure is followed in time under the steady presence of constant the global pressure gradient. Here we inspect the evolution of the total pressure gradient force in the dust dense region. Expressions for these are

$$P_{\text{total}} = P + \beta c_s \Omega \rho_0 x, \tag{2.10}$$

$$-\frac{1}{\rho_g}\frac{\partial P_{\text{total}}}{\partial x} \cong -\frac{1}{\rho_g}\frac{\partial P}{\partial x} - \beta c_s \Omega. \tag{2.11}$$

Figure 2.4(a) shows the snapshots of the total pressure at $t\Omega = 0, 50, 500$ from the 2-D case. At the pressure bump, the total pressure profile tends to become flat in time. And finally at $t\Omega = 500$, whole dust dense region has almost zero total pressure gradient. In figure 2.4(b), to confirm the pressure flattening, we check the evolution of the pressure gradient force in the dust dense region ($-0.2H < x < 0.1H$). The spatially averaged pressure gradient converges to ~ 0.0013 while the initial value of the global pressure gradient is $\mid \beta \mid = 0.04$. Therefore the pressure gradient force at the dust dense region is $\sim 10 - 100$ times smaller than what is initially set for the region outside the bump. As we will discuss later, the significantly smaller pressure gradient plays an important role for initial clump size and following pebble accretion onto the clumps.

To investigate a simpler case without the global pressure gradient, we conduct a 1-D simulation with $\beta = 0$. In this case, there is no accretion of radially drifting dust particles from outside the pressure bump, but dust concentration happens within the pressure bump towards the point of the pressure maximum. Figure 2.5 shows that snapshots of the gas profile evolution ($t\Omega = 50, 250, 500$). Panel (a, b) shows the gas pressure profile and the gas azimuthal velocity profile (deviation from Keplerian rotation). Panel (c) shows the dust density profile. These panels show that the system puts on a steady profile by $t\Omega \sim 250$. In the dust dense region, the dust density is $\sim \rho_0$, the gas azimuthal velocity is ~ 0, and the gas pressure profile is flattened. That is, gas is also making a Kepler motion due to strong drag from dust particles. This happens in the area where dust-to-gas ratio is ~ 1. This clearly depicts the essential nature of what are seen in the 2-D or 1-D simulations with the global pressure gradient. The only difference is that, in the simulations with global pressure gradient, the completely flattened pressure profile (the dust dense region) expands outward due to the continuous dust inward radial drift.

Note that we call this type of gas density evolution “deformation” of the pressure bump in this thesis. As seen in this section, the pressure bump is flattened but the deformed state of gas profile is not same with gas profile of the nominal MMSN model. The pressure bump becomes a local region which is in certain “dust dominated phase” (Nakagawa et al. 1981, 1986) due to dust trapping.

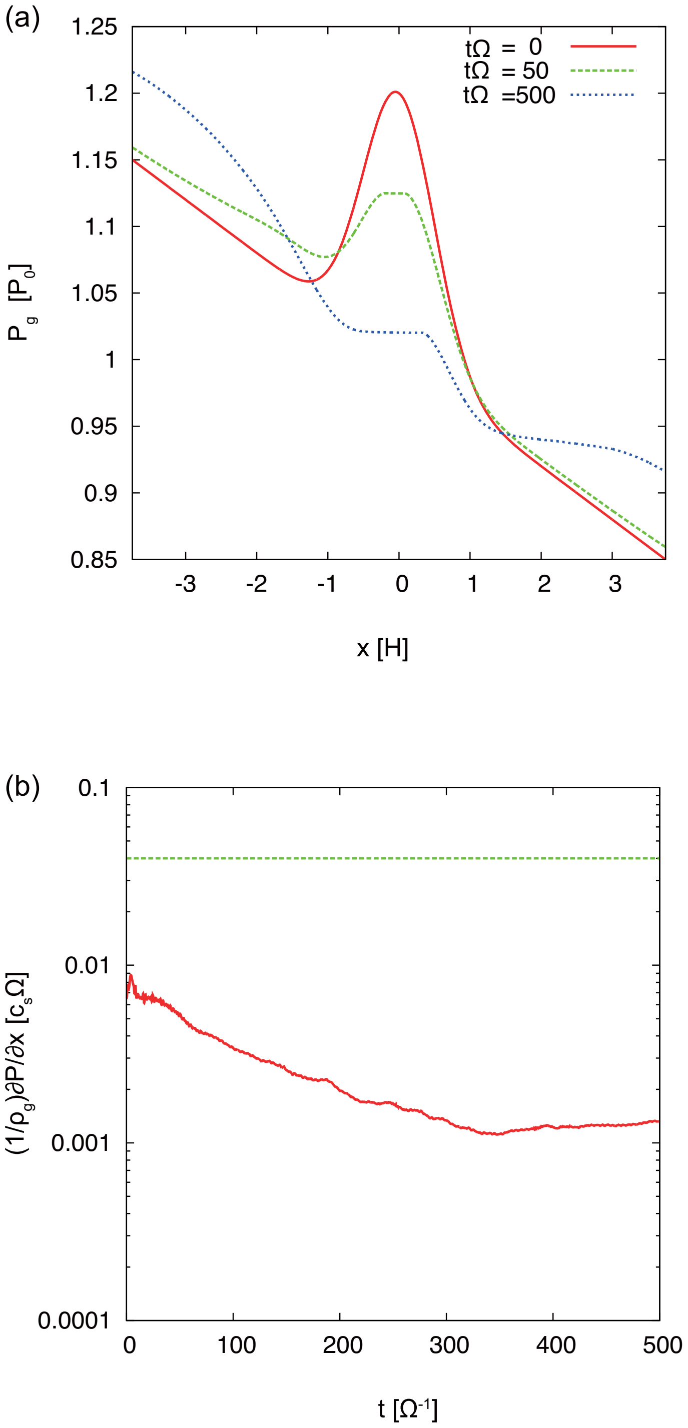

FIGURE 2.4: (a) Vertically averaged gas pressure profile and (b) time evolution of the radial pressure gradient force averaged spatially in the dust dense region from run β04-2D (2-D w/ bump). As the dust particles accumulate at the bump, the total gas pressure profile is flattened. Then the pressure gradient force at the bump converges to ~ 0.0013, which is smaller than the global pressure gradient $\beta = -0.04$ set initially (green dashed line).

2.3 Discussion

2.3.1 Schematic of the Pressure Bump Evolution

In this sub-section, we discuss the mechanism for dust and gas density evolution at the radial pressure bump. First, we describe a 1-D picture of the evolution in the radial direction. The 1-D evolution can be separated into two parts. One is the saturation of the dust density due to the pressure gradient evolution. The second is the deformation of the entire pressure profile due to the continuous dust inward accretion to the outer-edge of the pressure bump from the outer-part of the disk.

The saturation of the dust density occurs when the dust and gas achieve the equilibrium state near the center of the radial pressure bump. Initially, the growth of the dust density is faster than the gas density evolution. The reason is that the dust inward drift velocity is faster than the gas outward flow velocity when the dust-to-gas mass ratio is smaller than unity. As the dust density increases near the center of the pressure bump, the dust-to-gas mass ratio achieves ~ 1. Then the gas radial velocity becomes comparable to the dust radial drift velocity, meaning that the timescale of the gas density evolution is equalized with the timescale of the dust density increase. The outward gas flow flattens the pressure bump and continues until the total pressure gradient force becomes ~ 0. Upon reaching the state where the pressure gradient force is ~ 0, the dust and gas have almost zero radial velocity and achieve a steady state. The equilibrium is such that both dust and gas are mostly in the Kepler rotation state. Since further density concentration cannot be expected, the maximum dust concentration saturates at the dust-to-gas mass ratio ~ 1.

Regarding the second point, the entire pressure bump deformation is brought about by the continuous dust accretion onto the outer part of the pressure bump. On the inner side of the pressure maximum, there are no dust particles except for the left-over from the initial condition. There is no local cause to modify the pressure structure of the inner part. When there is continuous dust accretion onto the outer edge, however, the gas pressure in the outer part keep leaking outward. The radial profile of the gas pressure is modified and the force balance in the inner part is also broken. The result is that the super-Keplerian rotating gas in the inner-part is shifted outward to fill the void created by the leak in the outer part. This outward flowing mechanism continues until the dust accretion at the outer-edge ceases or the pressure bump is destroyed entirely.

The simpler 1-D calculation with no global pressure gradient helps us very clearly understand the bump evolution since the final stage does not change in time and thus the interpretation becomes easier. Since there is no global pressure gradient $\beta = 0$, there is no dust accretion from outside the pressure bump but the dust particles which existed initially inside the pressure bump accumulate at the super-/sub-Keplerian transition point. The results shown in Fig. 2.5 indicate that the maximum dust density of $\rho_{\mathrm{d,max}} \sim 1.4\rho_0$, which is the same with the case $\beta = -0.04$, is obtained in the region where the gas pressure gradient is nearly 0. The flattened pressure profile in the dust dense region is in a steady equilibrium state. That is, the dust concentration stops when the state in which both gas and dust are in Kepler rotation is achieved. Dust-to-gas mass ratio of ~ 1 is when the dust drag becomes strong enough to enforce the gas motion to Kepler rotation. On the other hand, Fig. 2.6 shows that results of a case with the global pressure gradient and the pressure bump is completely flattened in all part. A difference between these two cases is only an existence of the global pressure gradient. This indicates that the deformation of the inner side of the pressure maximum is induced by the continuous dust accretion produced by the global pressure gradient.

Results of the 2-D simulation are explained by the 1-D picture added with the vertical modulation due to the SI. After the formation of a dust dense region with the dust-to-gas ratio of ~ 1 due to the 1-D dynamics, the SI is excited because of the high dust density and the presence of non-vanishing pressure support in the disk. Note that the pressure gradient in the dust dense region is highly reduced from the initial condition. The detailed property of the SI that is excited in this environment is discussed in the following section.

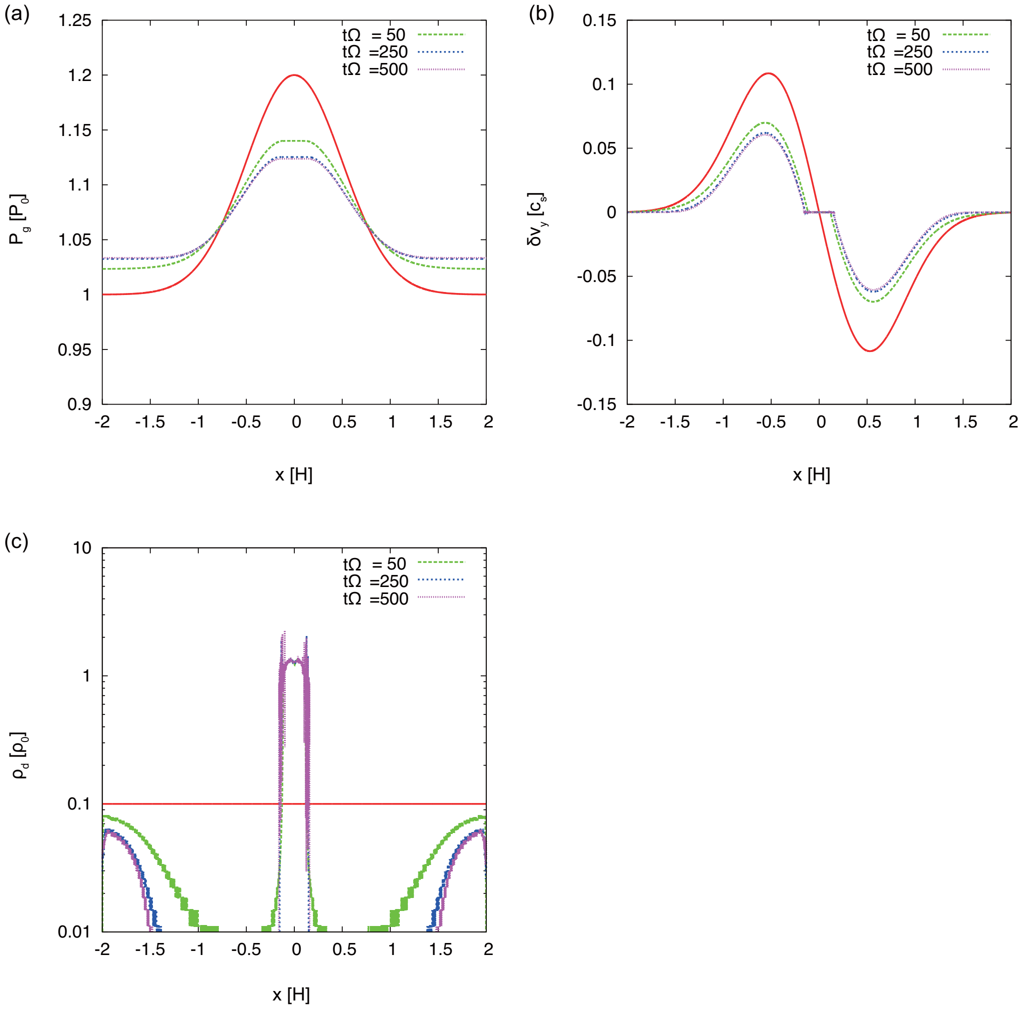

FIGURE 2.5: Results from the model without the global pressure support (run β00-1D). (a) gas pressure, (b) gas azimuthal velocity (the deviation from the Keplerian rotation), and (c) dust density, respectively. The essential physics of dust enriched region can be learned from this simple simulation results.

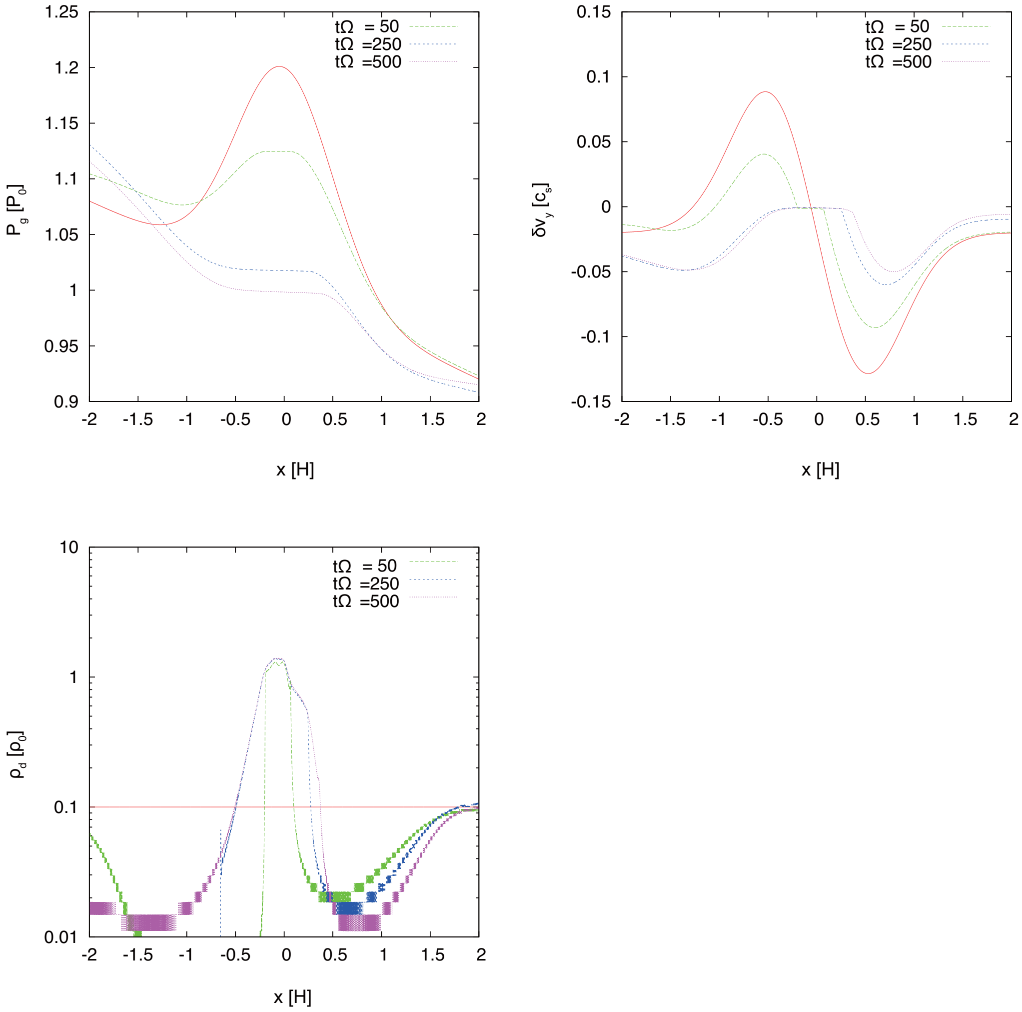

FIGURE 2.6: Similar to Figure 2.5 except that the global pressure gradient $\beta = -0.04$.

2.3.2 Property of the SI in the Dust Dense Region

In this section, we discuss the detailed property of the SI excited in the dust dense region formed by the radial pressure bump. The dust dense region formed by the radial pressure bump can be regarded as the initial condition of the SI. We found that in the dust dense region, (i) the dust-to-gas mass ration is ~ 1 and (ii) η is reduced by $10-100$ times from the nominal value of MMSN.

The relatively high dust-to-gas ratio is favorable for SI (Youdin and Johansen 2007). Especially when the frictional timescale τ_f is short, the pressure bump may be important for SI to occur. The bump deformation mechanism does not depend on the frictional timescale strongly. Then, in the dust dense region formed by the pressure bump, the dust-to-gas mass ratio does not change when the dust particles are small. However, for short frictional timescales, the growth rate of SI rises drastically at the dust-to-gas mass ratio $\gtrsim 1$. Therefore, the pressure bump may be a good location for the planetesimal formation, even for the small dust particles.

Because spatial and velocity scales of SI are respectively normalized by ηr and $\eta v_{\rm K}$, the size of dust clumps predicted at the pressure bump is also $10 - 100$ times smaller than that given by Johansen and Youdin (2007). Johansen et al. (2012) conducted simulations including many effects (e.g., vertical gravity, particle self-gravity, particle collision) to find that the SI forms $\sim 100 - 1000$ km sized clumps gravitationally bound. The clumps size at the pressure bump is estimated as $\sim 1 - 100$ km, which is similar to the classically predicted planetesimal size. On the other hand, thanks to the small η, pebble accretion rate onto the planetesimals would become more efficient than in the case of original when the planetesimals grow to enter "settling regime" (e.g. Guillot et al. (2014)).

Note that spatial resolution of our calculations is insufficient to resolve the SI at the dust dense region. We assume that the width of the radial pressure bump is comparable in size to the gas pressure scale height. To ensure a sufficient width for the dust drift and accumulation, our computational box has ~ 10 scale heights in radial direction. However, the short wavelength of the SI at the dust dense region requires higher resolution. While we noticed that higher resolution leads to stronger clumping, we have not achieved a saturation of dust clumping. A simple prediction is that the maximum dust density is similar to the results of Johansen and Youdin (2007).

2.3.3 Lifetime of the Dust Dense Region

In the previous subsections, we found that the relatively broad dust dense region is formed at the pressure bump, while the pressure bump is deformed by the dust accumulation. The dust-to-gas ratio at the dense region, however, is too low to drive the gravitational instability which directly forms the planetesimals in an orbital time. While the dust-to-gas mass ratio ~ 1 is a favorable condition for the streaming instability (see Sec.). In addition, the velocity scale of the streaming instability becomes small at the dust dense region (Sec. 2.3.2) and the radial drift velocity also small because of the small pressure gradient (see Fig. 2.4). This indicates that the relative velocity of dust particles is likely to be small enough for direct sticking.

Then, to form the planetesimals, the lifetime of the dust dense region should be longer than the growth timescale of the dust particles due to the streaming instability or the direct sticking. Fig. 2.7 represent the dust density distribution as a function of the time and the radial coordinate. The life time of the dust dense region is at least $\sim 100 t_{\rm K}$. The region where the dust-to-gas ratio is unity or higher (colored in yellow) keeps an almost same width with time after $t\Omega \sim 100$. This is induced by a balance between the mass fluxes: the inflow from outer side of the bump and the outflow from inner side of the bump.

The required time for the linear growth of the streaming instability is $\sim 10 t_{\rm K}$ (Johansen and Youdin 2007) which is enough shorter than the lifetime of the dust dense region. Actually, we partly confirmed the growth of the streaming instability in Sec. 2.2.2. In addition, an expectancy of the dust growth is estimated as follows. The bump crossing time of the dust particles which have the fastest drift velocity ($\tau_{\rm s} = 1$) is estimated as $t_{\rm cross} \sim H/(\eta v_{\rm K}) \sim 10 - 40 t_{\rm K}$, where the width of the dust dense region is assumed to $\sim H$ and the global pressure gradient η is $10 - 100$ times smaller than the MMSN model. For the Epstein regime, the growth time of the particles having the $\tau_{\rm s} = 1$ is,

$$t_{{\rm grow}|\tau_{\rm s}=1} = m \left(\frac{{\rm d}m}{{\rm d}t} \right)^{-1} \approx 30 \left(\frac{\epsilon}{0.01} \right)^{-1} t_{\rm K}, \tag{2.12}$$

where m is the particle mass (Okuzumi et al. 2012). Therefore the ratio between two timescales at the dust dense region ($\epsilon \sim 1$) is $t_{\rm grow}/t_{\rm cross} \sim 1/30 - 1/100$, and a mass of dust particles which pass through the dust dense region can increase $2^{30} - 2^{100}$ times larger than the initial state by the naive estimate.

In this regard, the dust dense region formed by the pressure bump may be a favorable location for the planetesimal formation. We investigate the effect of the dust growth to the dust and gas density evolution at the radial pressure bump in Chap. 4.

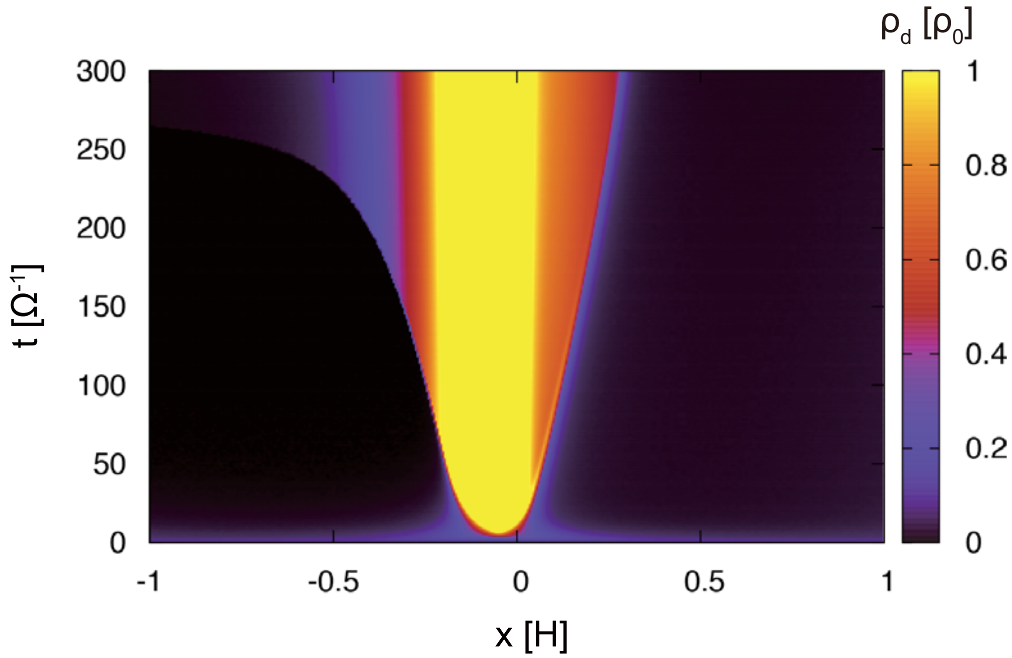

FIGURE 2.7: Time evolution of the dust dense region in run β04-1D. The panel shows the dust density as a function of a radial coordinate x and time t. The yellow region has the dust-to-gas ratio more than unity and keeps an almost same width after $t\Omega \sim 100$. At $t\Omega \sim 150$, the super-Keplerian region is deformed completely and dust particles restart the radial inward drift from the inner edge of the pressure bump. Note that the region near the pressure bump is zoomed-in and the whole computational domain is wider in radial direction.

Chapter 3

Pressure Bump Evolution Due to the Thin Dust Layer

3.1 Numerical Model and Initial Conditions

In this chapter, we investigate the dust and gas density evolution at the pressure bump when the vertical width of the dust layer is thinner than the gas disk. We use the same physical and numerical model with Chap. 2. The gas equations are Eq. (2.1)- (2.3), and the dust equations are Eq. (2.6). These equations are approximated by the local shearing box. The dust particles are treated as the super-particle approach. We assume that the protoplanetary disk is axisymmetric and isothermal in our local model. At this moment, a computational domain is 2-D (radial-vertical) in all simulations. Note that we neglect the vertical gravity of the host star, and do not use the stratified disk model.

In our fiducial model, column density of the dust particles is assumed to $\Sigma_d = 0.01$. The half width of the dust layer is $0.05H$ supposed that the marginally sedimented midplane dust layer for $\tau_s \sim 1$ (Youdin and Lithwick 2007). Therefore, the spatial density of dust layer is $0.2\rho_0$. For simplicity, we neglect the vertical gradation of the dust layer. The dust spatial density is uniform in defined dust layer.

We set the same pressure bump with Sec. 2.1.2 as an initial condition. The pressure bump is steady state sustained by the azimuthal velocity distribution except for the dust drag force. Since the vertical width of our numerical domain is smaller than the gas scale height, the initial gas profile is uniform in vertical direction. Note that the global pressure gradient β is set to 0 in the fiducial model for simplicity.

Fig. 3.1 represents the initial condition of the dust and gas density distribution in our fiducial model. Other parameters and settings are summarized in Table 3.1.

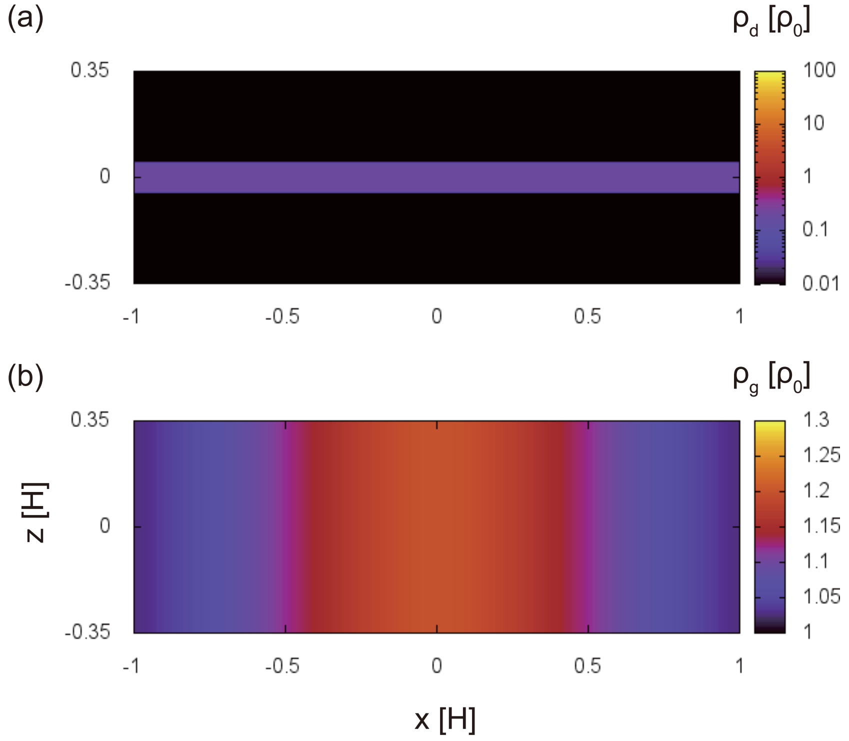

Figure 3.1: Initial conditions of (a) dust density and (b) gas density distributions in run –. The dust particles are located near the midplane. A width of the dust layer is 0.1H and the density is $0.2\rho_0$. It means that the dust surface density is $0.01\rho_g$. The gas density has the pressure bump in radial direction, and has the uniform distribution in vertical direction. A peak value of the gas density is $1.2\rho_0$. A center of the pressure bump is located at a center of the computational domain.

Run	$L_x[H] \times L_z[H]$	$L_p[H]$	ϵ_0	β	τ_s	dust at bump
C4-01	4×0.7	0.1	0.2	0	1.0	yes
C4-02	4×0.7	0.1	0.2	-0.04	1.0	yes
C4-03	6×0.7	0.1	0.2	-0.04	1.0	no
C4-04	4×0.7	0.1	0.1	0	1.0	yes
C4-05	4×0.7	0.2	0.1	0	1.0	yes
C4-06	4×1.0	0.2	0.1	0	1.0	yes
C4-07	4×0.3	0.1	0.1	0	0.1	yes
C4-08	4×0.3	0.1	0.1	0	0.01	yes
C4-09	4×0.3	0.1	0.1	0	1.0	yes
C4-10	4×0.5	0.1	0.1	0	1.0	yes
C4-11	4×0.7	0.1	0.1	0	1.0	yes
C4-12	4×0.9	0.1	0.1	0	1.0	yes
C4-13	4×1.1	0.1	0.1	0	1.0	yes
C4-14	4×1.3	0.1	0.1	0	1.0	yes

TABLE 3.1: Setup of individual runs. L_x, L_z are the radial and vertical width of computational region. L_p is the width of the initial dust layer. ϵ_0 is the initial dust-to-gas ration at the dust layer. τ_s is the dimensionless stopping time of dust particles. β is the global pressure gradient coefficient. The"dust at bump" means that the initial dust position is uniformly configured though at the pressure bump or not (see Fig. 3.9). A size of the grid cell is fixed at $0.005H \times 0.005H$ in all runs. At the initial dust layer, the number of dust particles at each grid cells is also fixed in 25 particles. The total run time t_end is fixed in $500\Omega^{-1}$ except for run C4-06 ($t_\mathrm{end} = 200\Omega^{-1}$).

3.2 Results

3.2.1 Result of the Fiducial Model

To investigate the basic property of the dust and gas evolution due to a dust accumulation in the thin dust layer, we assume the simplest settings in this subsection. The initial dust layer is regarded as an uniform dust belt near the midplane. Since the global pressure gradient is neglected, the computational domain is actually symmetric about the center in radial direction.

Fig. 3.2 represents the snapshots of the dust density pattern at $t\Omega = 10, 50, 100, 500$. The dust particles start accumulation toward the pressure maximum in the same manner as Chap. 2. Until $t\Omega = 10$, the dust-to-gas ratio achieves ~ 1 and the vertical compression is observed near the center of the pressure bump. Almost all particles trapped by the pressure bump until $t\Omega = 100$. The region which has the highest dust density is thinner than the initial dust layer. A formation mechanism of this thinner region is explained in Sec. 3.3.1. Note that the highest density is significantly higher than ρ_0 (see also Fig. 2.1). At the final state when the gas pressure profile achieves quasi steady, the dust particles are mixed in vertical direction.

Fig. 3.3 shows that the snapshots of the velocity field of dust and gas at $t\Omega = 10$. Panel (a) represents the dust velocity field which is the mean velocity of the super-particles at each grid cell. The dust velocities actually face toward the center of the pressure bump, as we observed in Fig. 3.2. The region where the dust-to-gas ratio is unity or higher (cyan region) have small velocity. This is the natural tendency of the dust radial drift at the region which has the high dust density and/or small pressure gradient. Around the cyan region, the dust velocities slightly have the vertical component. Panel (b) represents the gas velocity field. We can observe vortex like structures. This vortex flow, especially a vertical flow from upper part to midplane, compress the dust layer in vertical direction. Therefore the dust density becomes higher than the simply radial accumulation. The detailed mechanism of this compression process is discussed in Sec. 3.3.1.

The dust accumulation process induces a deformation of gas pressure profile at the radial pressure bump. When the dust-to-gas ratio achieves ~ 1, the dust drag force is large enough to deform the gas density structure. Fig. 3.4 shows that the gas pressure profile at $t\Omega = 100$. The purple line is the initial state of the pressure bump which is uniform in vertical direction by definition. The green solid, red dashed-dotted, and yellow dashed lines represent the gas pressure at the $z = -0.35H, 0$, and $0.35H$, respectively. In this figure, we found that there is no vertical variation of the evolved gas pressure profile, although the dust layer is thinner than the gas disk (see also Sec. 3.3.4).

Evolution of the maximum dust density is shown in Fig. 3.5. The purple line represents the result of our fiducial run in this chapter. As we have already seen in Fig. 3.2, the maximum dust density $\rho_{\rm d} \sim 50$ is significantly higher than the 1-D case (green line; almost same settings with run β04-1D of Chap. 2). Until the dust-to-gas ratio achieves ~ 1, however, these two cases undergo a similar evolution (see panel (b) of Fig. 3.5). It is consistent behavior with the explanation that the dust density enhancement is produced by the vertical gas flow induced by the pressure bump deformation (see also Sec. 3.3.1).

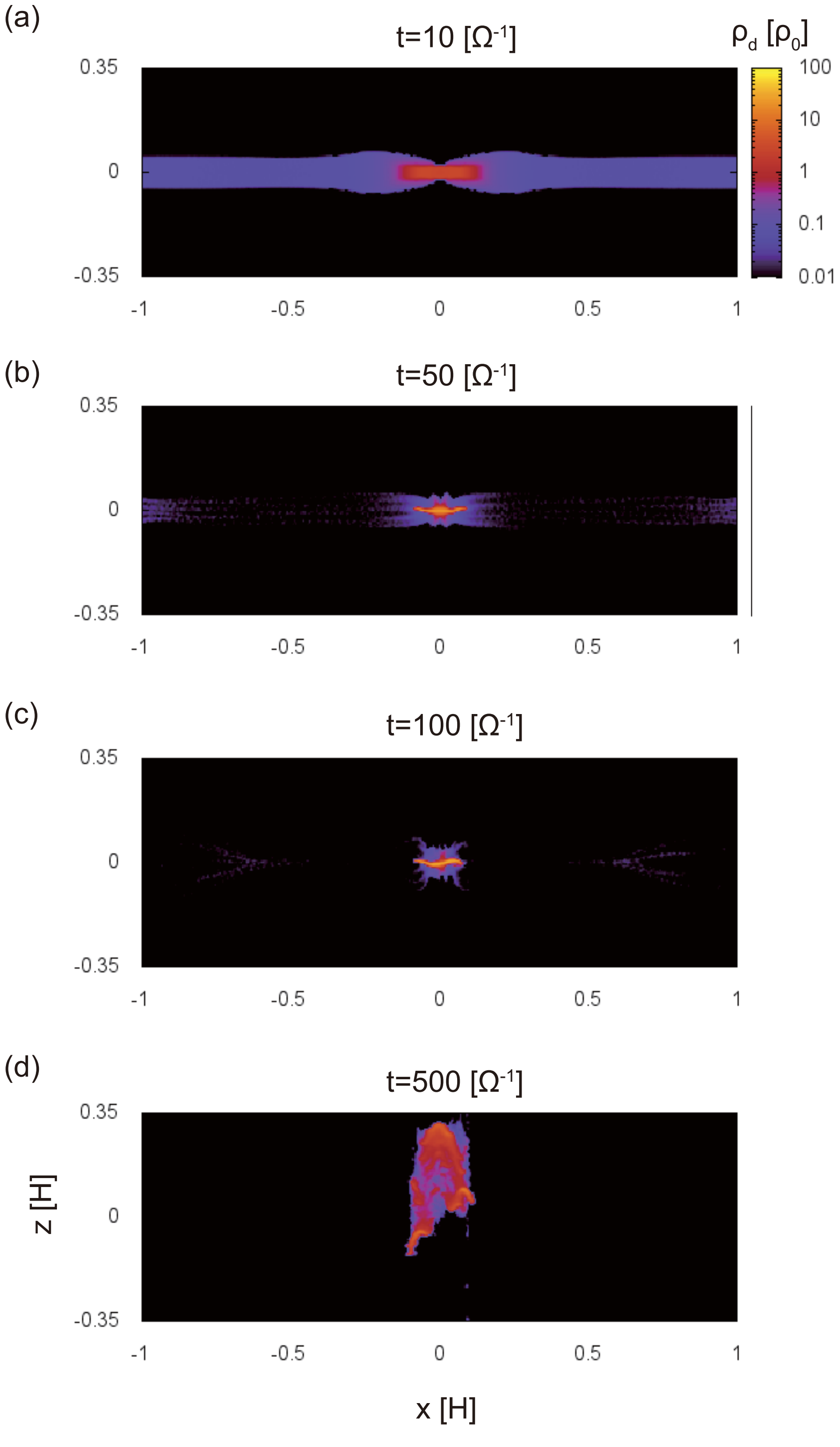

Figure 3.2: Dust density pattern from run –. Each panels represent the snapshots at (a) $t\Omega = 10$, (b) 50, (c) 100, (d) 500, respectively. The dust particles accumulate at the center of the pressure bump. A dust dense region formed by the trapped dust particles is compressed in vertical direction due to the vertical gas flow. Therefore the dust density has the peak value at the midplane transiently (see panels (b) and (c)). The peak value of the dust density is over $\sim 50\rho_0$ (see Fig.–). The dust dense region diffuses in vertical direction until the end of the simulation.

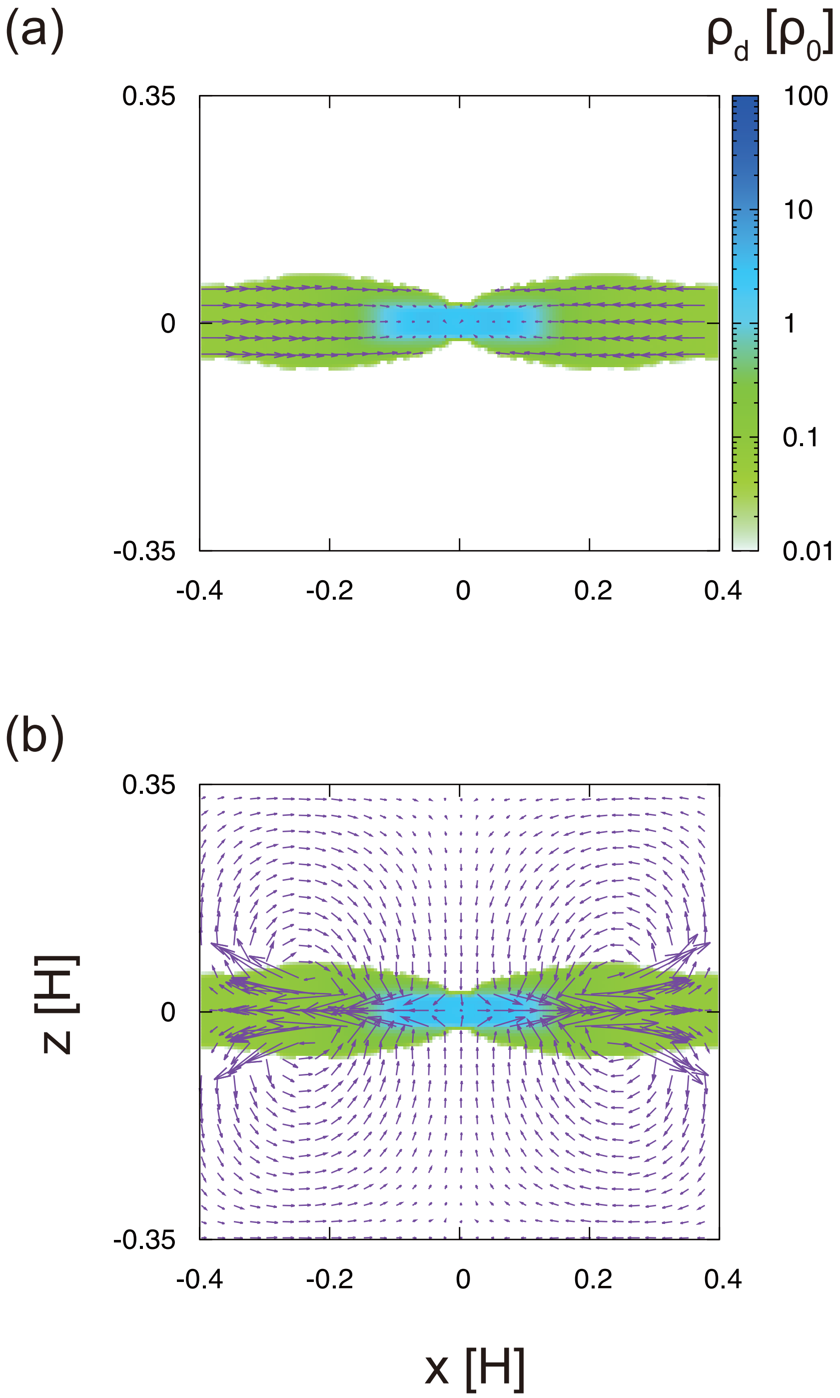

Figure 3.3: Snapshots of the velocity field of (a) the dust and (b) the gas at $t\Omega = 10$. The dust velocity field is defined by the mean velocity of the super-particles at each grid cell. Contours represent the dust density distribution in both panels. The dust particles tend to drift toward the point of the pressure maximum. In the midplane, the gas moves outward from the pressure bump due to the dust accumulation. The radial motion drives the vertical flow of the gas and the vertical compression of the dust layer. Note that the scale of dust velocity arrows is 10 times larger than the gas velocity arrows.

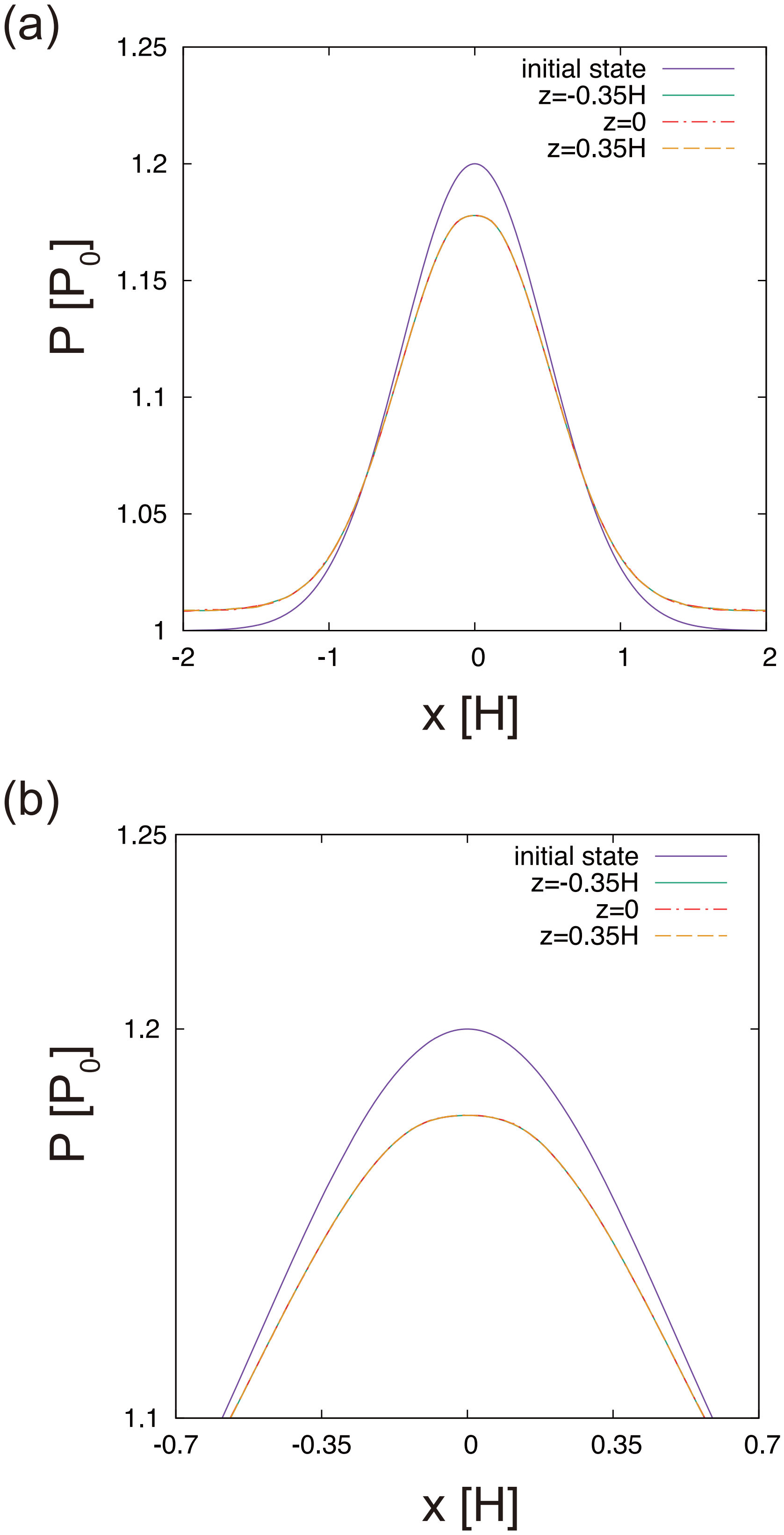

FIGURE 3.4: Snapshots of the gas pressure distribution at $t\Omega = 100$ in radial direction. Each lines shows the gas pressure at the plane $z = -0.35H$ (green solid line), 0 (orange dotted-dashed line), and $0.35H$ (yellow dashed line), respectively. Panel (b) is the enlarged view of the center of panel (a).

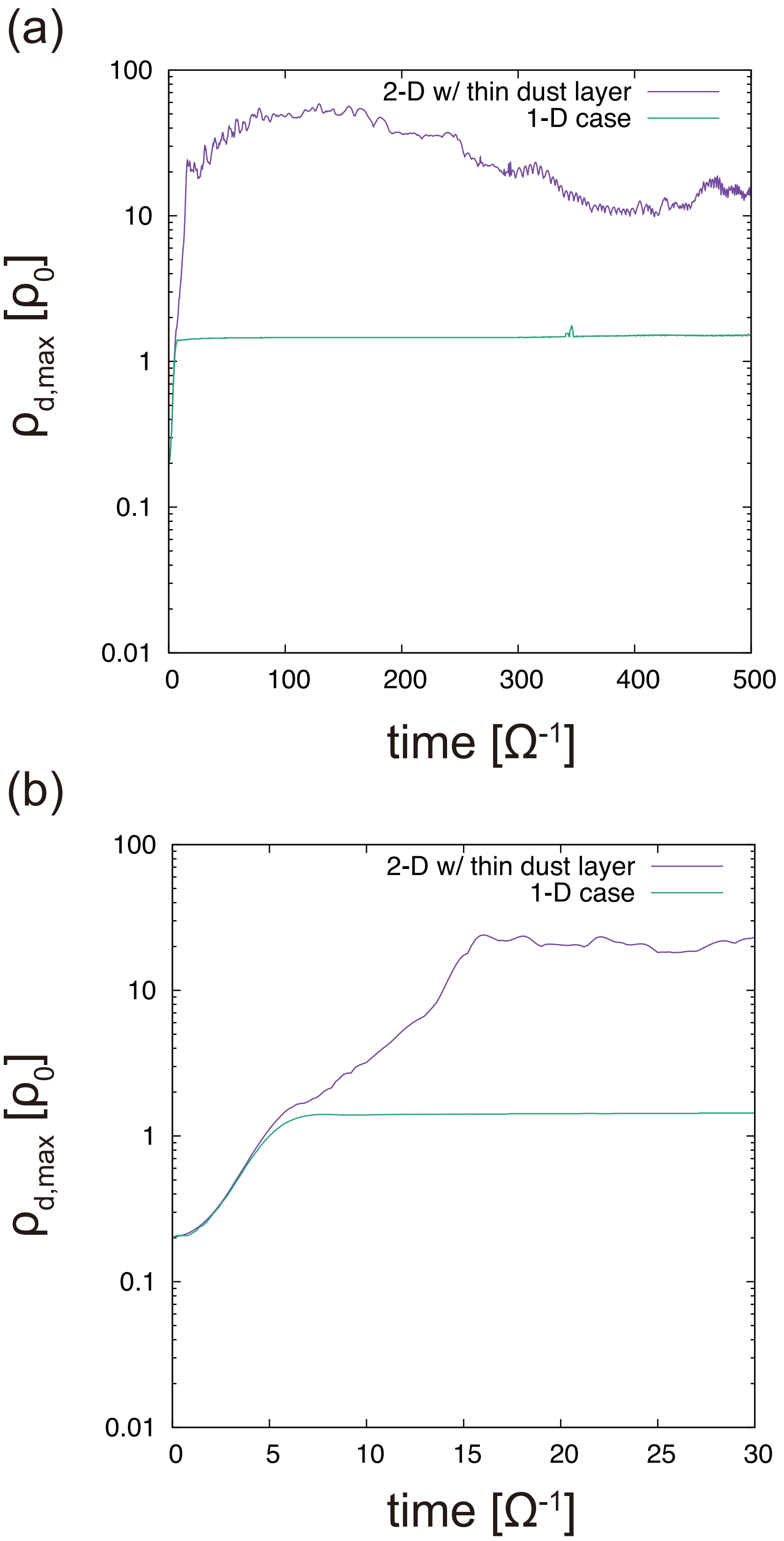

FIGURE 3.5: Time evolution of the maximum dust density in run C4-01 (purple line) and run $\beta 04 - 1D$ (1-D case in Chap. 2; green line). All lines represent the dust density in the cell having the highest density over the whole computational region, normalized by the background gas density ρ_0. Panel (b) is the enlarged view of the initial phase of the panel (a). The initial dust accumulation due to the bump structure is almost the same in the two runs (see panel (b)). In run C4-01, the dust density increases to ~ 50 due to the vertical compression by gas flow.

3.2.2 Case with the Global Pressure Gradient

In the previous subsection, we found the vertical compression of the dust layer at the radial pressure bump. The compression is driven by the vertical gas flow due to the accumulation of the dust particles near the midplane. However, the fiducial run is conducted with the simplest settings. Then we should check the dependency of our assumption (and we summarized the dependency in Sec. 3.3.3). First, we confirm the effect of the global pressure gradient to the pressure bump evolution. The global pressure gradient may produce the asymmetric evolution of the pressure bump.

Fig. 3.6 represents the snapshots of the dust density pattern. In panel (b) and (c), the asymmetric evolution of dust density is observed. However the evolution path is not changed qualitatively: the vertical compression of dust dense region is occur, and the dust dense region is diffused in vertical direction at final state of our simulations.

Other properties in run C4-02 are also similar to the fiducial run. The evolution of the maximum dust density is showed in Fig. 3.7. Until $\rho_{\mathrm{d,max}} \sim 1$ (i.e., $t\Omega \sim 7$), the radial dust accumulation by the pressure bump increases the dust density. Following dust vertical flow produces the more enhanced dust density. The peak value of the maximum dust density is ~ 50. At the end of the simulation, the maximum dust density decreases ~ 10 because of the vertical diffusion. Fig. 3.8 shows that the snapshot of the (a) dust and (b) gas velocity field at $t\Omega = 10$. The dust velocities face toward the pressure maximum and the gas velocity field forms the vortex like structure. Because of the generic radial inward drift velocity (i.e., a velocity in a negative direction of our computational domain) due to the global pressure gradient $\beta = -0.04$, the absolute value of velocities at right-hand side of the computational domain is larger than the left-hand side.

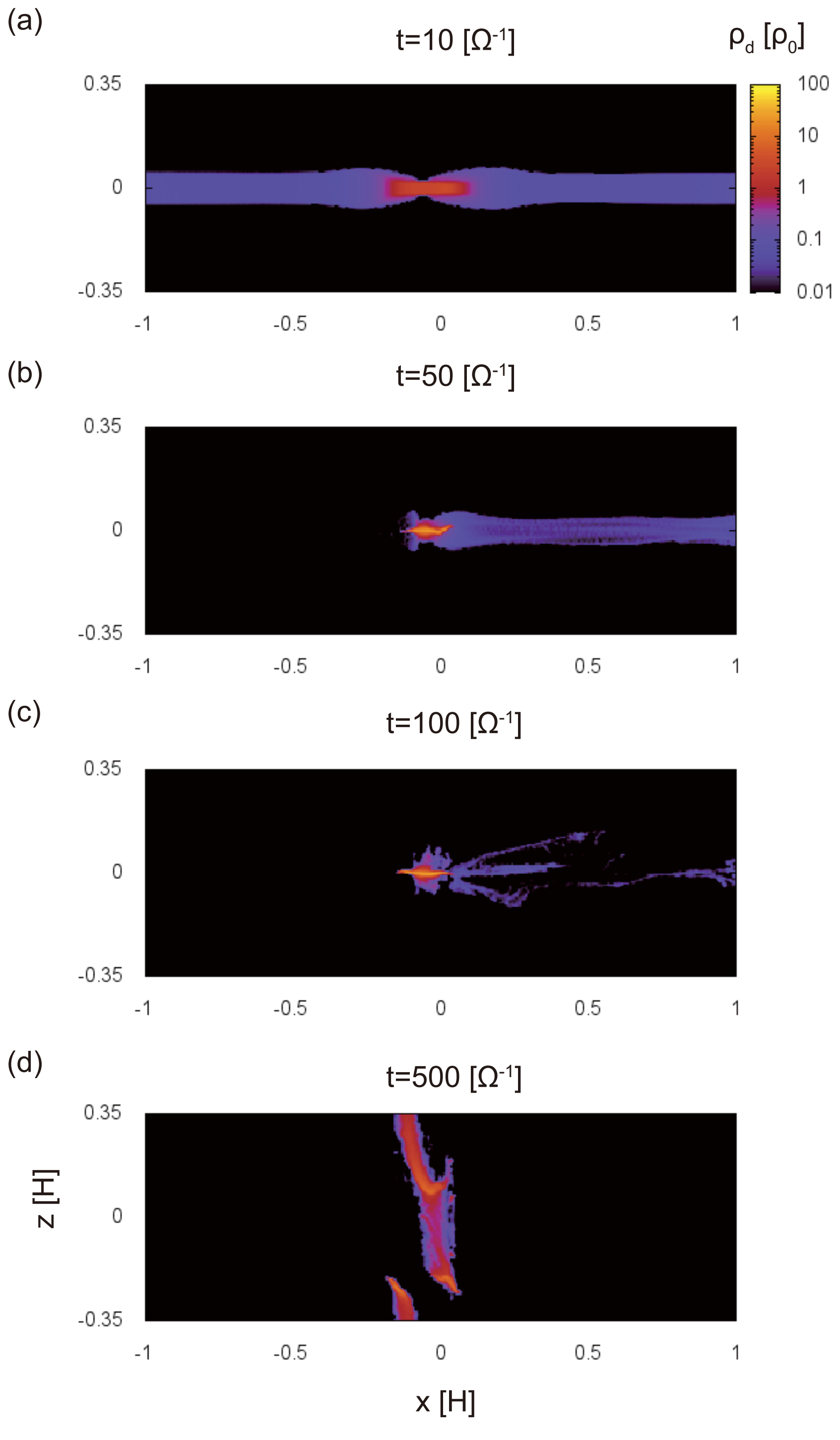

FIGURE 3.6: Same plots as Fig. 3.2 except that the global pressure gradient $\beta = -0.04$. There are an asymmetric dust radial flow due to the global pressure gradient (see panel (b), (c)). The shape of the dust dense region is almost same with the result of run – (case without global pressure gradient).

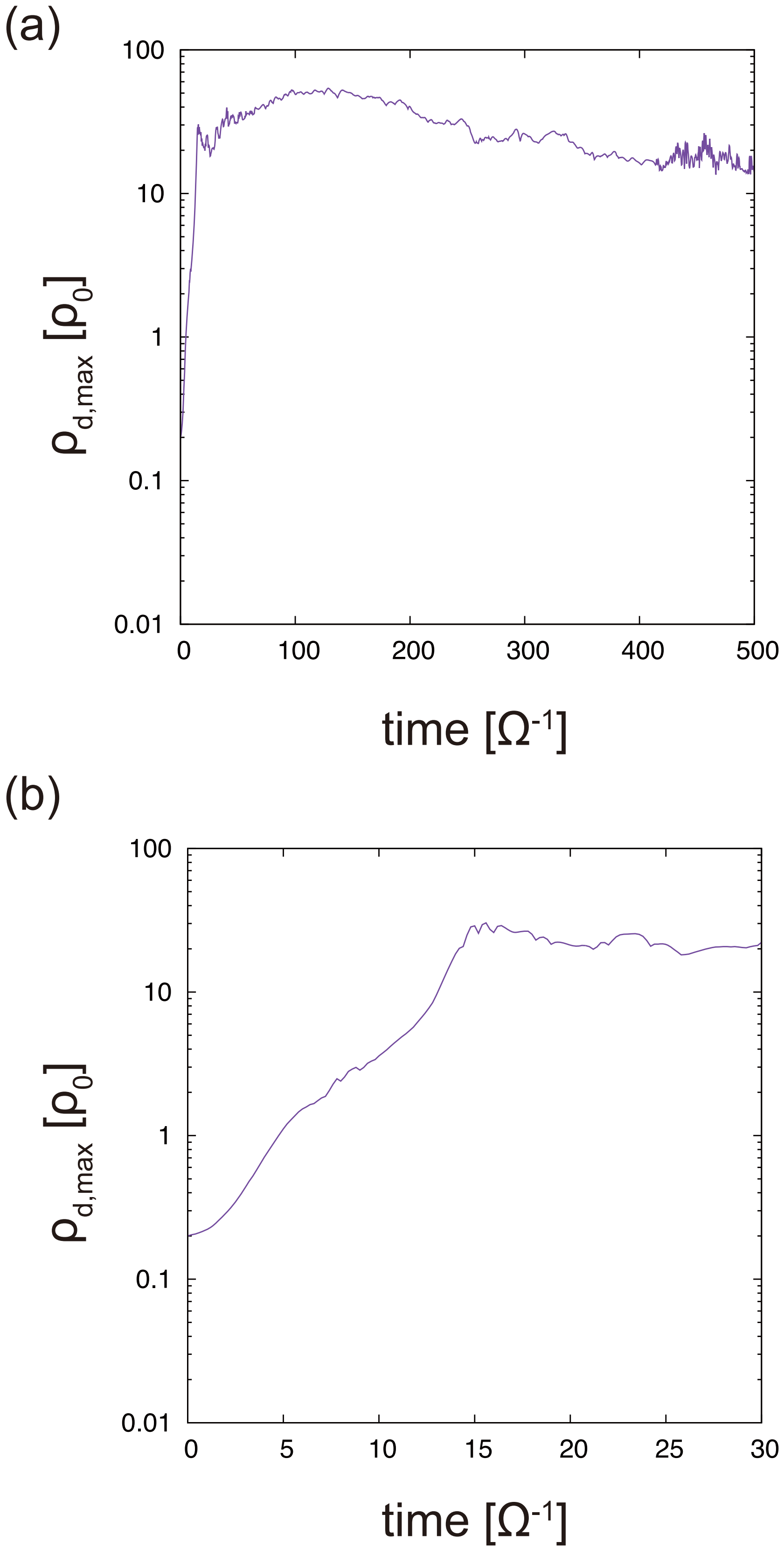

Figure 3.7: The same plot as Fig. 3.5 but for run – (case with global pressure gradient). Panel (b) is the enlarged view of the initial phase of the panel (a). The evolution of the maximum dust density is similar to Fig. 3.5.

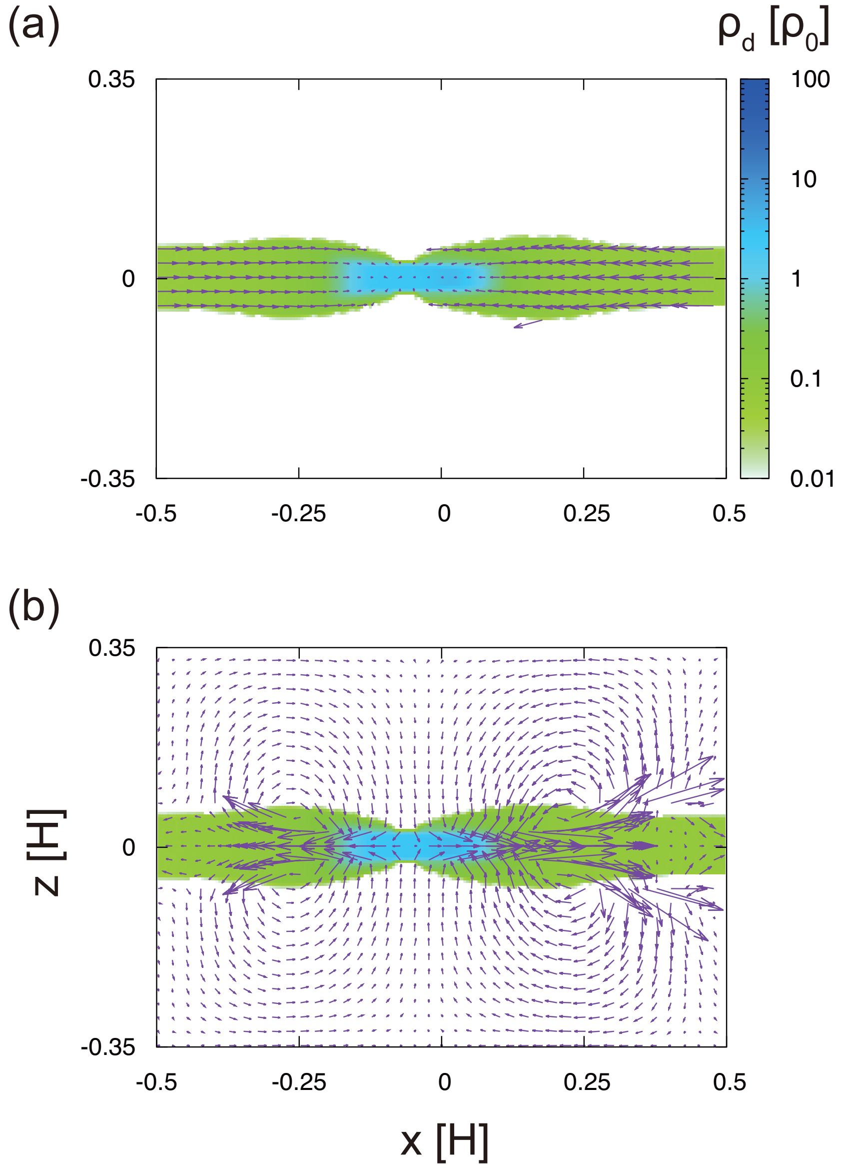

FIGURE 3.8: Same plots as Fig. 3.3 but for run – (case with global pressure gradient). Flows are almost same with Fig. 3.3, except for the radial asymmetry due to the global pressure gradient.

3.2.3 Case with No Dust Particles at the Pressure Bump

Next, we consider the case without dust particles at the pressure bump. The dust particles which is located in the pressure bump at the initial state is quickly accumulated at the pressure maximum all together. This concurrently accumulation and quick bump deformation has a possibility to overestimate the maximum dust density.

Fig. 3.9 represents the initial (a) dust and (b) gas density distribution of run C4-03. The initial gas profile is actually same with the fiducial run. We do not set the dust particles at the pressure bump ($\pm 1H$ from the center). To equalize the total mass of the dust particles, the radial length of the computational domain ($6H$) is longer than the fiducial run ($4H$).

The evolution of the dust density pattern is shown in Fig. 3.10. The dust inward drift deliver the dust particles to the pressure bump which has no dust particles at initial state. The dust dense region is formed around the pressure maximum. The vertical compression (panel (b),(c)) and diffusion (panel (d)) of the dust dense region also occur same with the fiducial run.

The existence of vertical compression is confirmed in Fig. 3.11. Since the dust particles do not achieve the pressure maximum, the vertical compression does not occur yet at $t\Omega = 10$. At $t\Omega = 20$, however, the subset of dust particles are trapped at the pressure maximum and the dust density increases to ~ 1. Since the dust dense region where dust-to-gas ration ~ 1 deforms the pressure bump, the gas vortices are induced by the outward gas flow at the midplane (see also Sec. 3.3.1). Although there is of course the significantly asymmetric properties, the qualitative evolution of the dust and gas profiles are not changed.

A peak value of the maximum dust density is slightly lower than the fiducial run. Fig. 3.12 shows that the peak value is $\sim 40\rho_0$, which is 20% lower than the fiducial case. Panel (b) of Fig. 3.12 is the initial phase of the maximum density evolution. An increase of dust density starts at $t\Omega \sim 12$ when the inner edge of the dust layer achieves the pressure maximum.

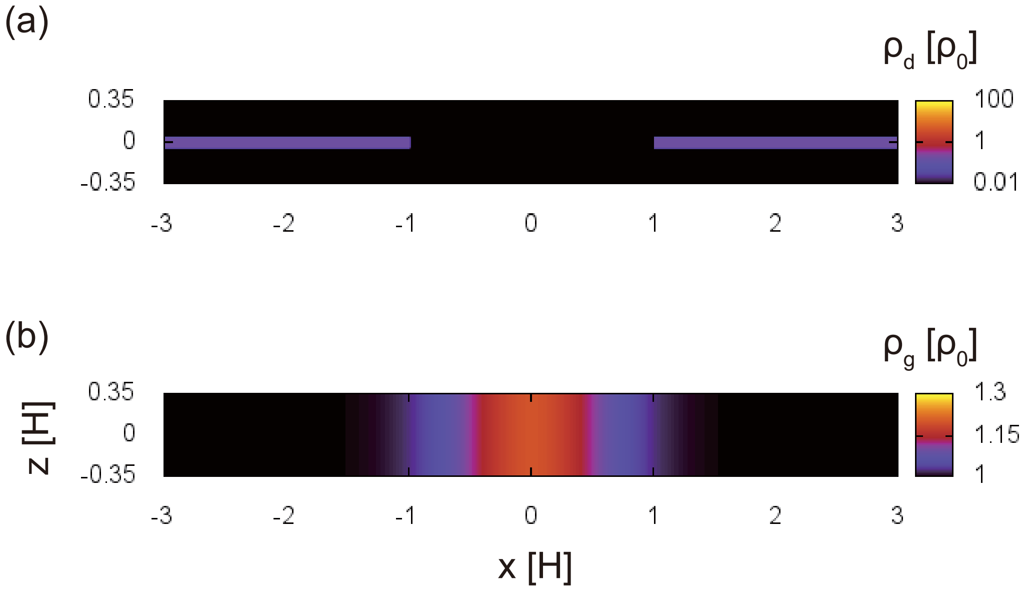

FIGURE 3.9: Initial conditions of (a) dust density and (b) gas density distributions in run –. The dust particles are located near the midplane outside the pressure bump. A width of the dust layer is 0.1H and the density is $0.2\rho_0$. It means that the dust surface density is $0.01\rho_g$. The gas density has the pressure bump in radial direction, and has the uniform distribution in vertical direction. A peak value of the gas density is $1.2\rho_0$. A center of the pressure bump is located at a center of the computational domain.

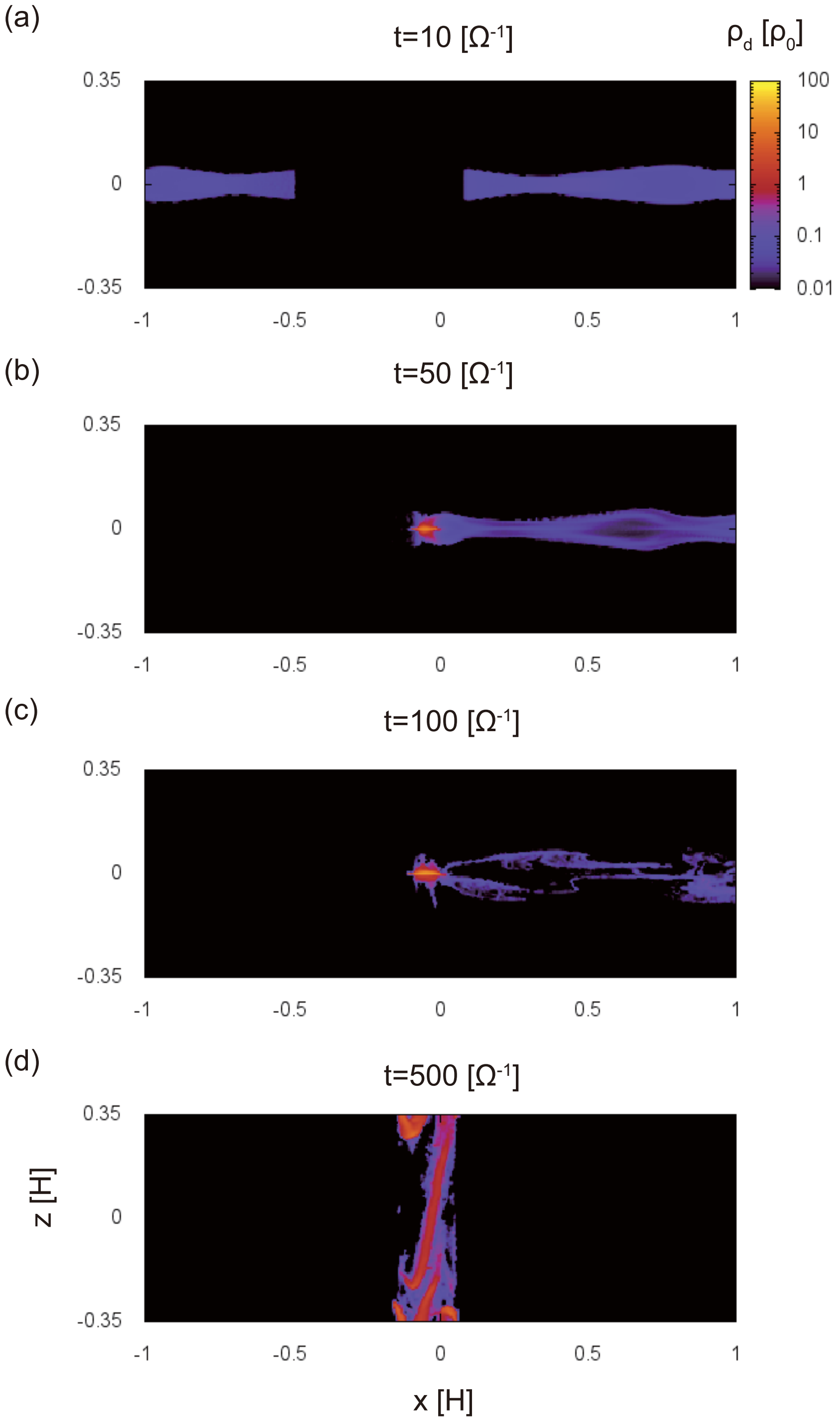

FIGURE 3.10: Same plots as Fig. 3.2 but for run – (case with no dust particles at the pressure bump). There are an asymmetric dust radial flow due to the global pressure gradient (see panel (a), (b), (c)). The shape of the dust dense region is almost same with the result of run – (case without global pressure gradient), run – (case with global pressure gradient).

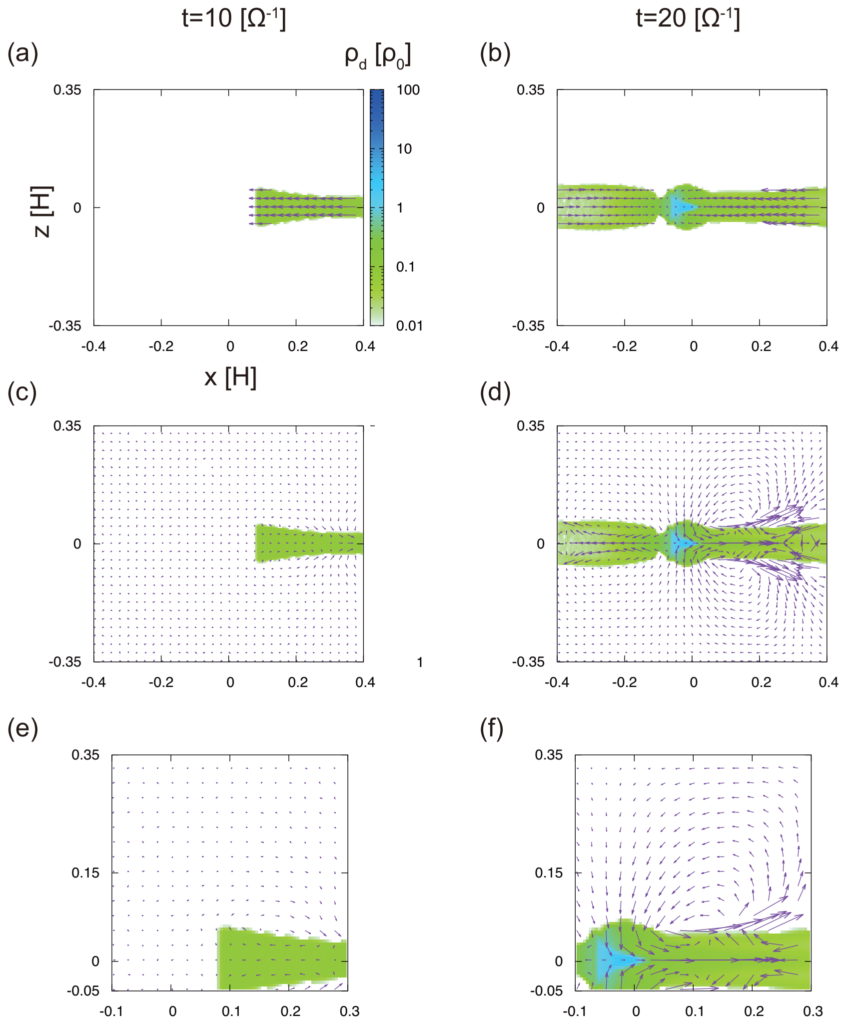

Figure 3.11: Dust and gas velocity field in run –. Left (right) column shows snapshots at $t\Omega = 10$ (20). Top panels are the dust velocity, middle panels are the gas velocity, and bottom panels are enlarged view of the gas velocity near the midplane. Contours represent the dust density distribution in each panels. Panel (e) shows that the midplane gas moves inwardly due to the dust drag force in initial phase of the bump evolution. After forming the dust dense region, where the dust-to-gas ratio is ~ 1, the gas velocity field becomes almost same with run – (see panel (f)).

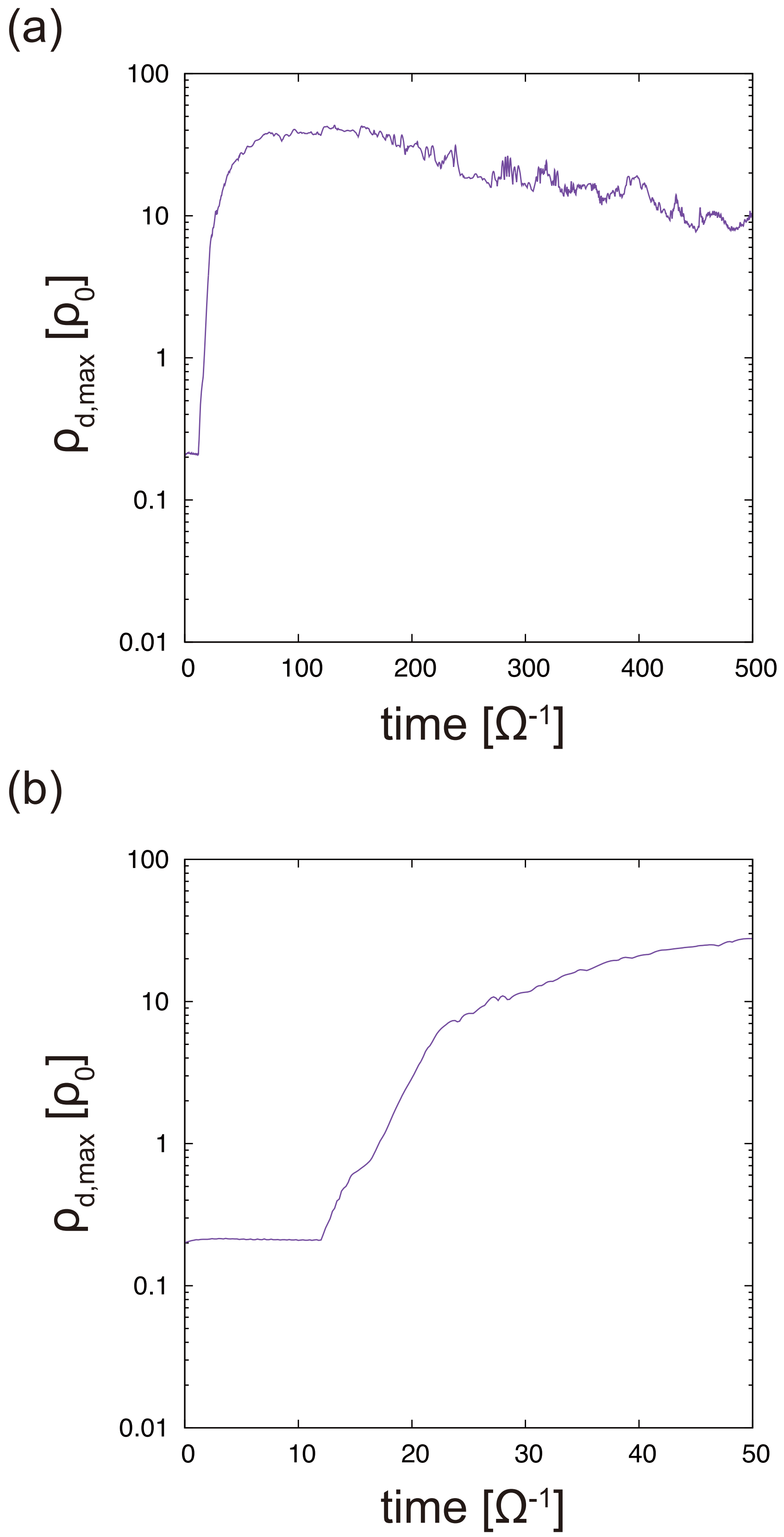

FIGURE 3.12: Same plots as Fig. 3.5 but for run –. The peak value is slightly smaller than the run –, –. Panel (b) is the enlarged view of the initial phase of the panel (a). Dust particles arrive at the point of the pressure maximum in $t\Omega \sim 12$. Then the maximum dust density starts to increase.

3.2.4 Effect of the Dust Surface Density

When the dust surface density is small, the peak density of dust might become small at the pressure bump. In this case, the angular momentum brought by dust accretion becomes small. The gas outward flow from the pressure bump is induced by the angular momentum exchange between the dust. So the timescale of the pressure bump deformation becomes slower than the fiducial case. The dust density enhancement is produced by the vortex like structures of gas flow, and vortices is induced by the bump deformation (see Sec. 3.3.1). If the gas vertical flow also weakens in this case, the peak dust density might be small. We should confirm the effect of the dust surface density to the gas vertical flow and dust density enhancement. In this subsection, we set the surface density of dust as $0.005\Sigma_{\rm d}$ which is two times smaller than the fiducial run.

Fig. 3.13 and 3.14 show that snapshots of dust density and the dust/gas velocity fields. Indeed dust dense region is narrower than fiducial run at same snapshot. This is because the dust mass flux is smaller than the fiducial run. Then the entirely deformation of the pressure bump requires more time. The gas vertical velocity at the dust dense region, however, seems to be not particularly changed (panel (b) of Fig. 3.14) In addition, the evolution of the maximum dust density is similar to the fiducial run (Fig. 3.15). A mechanism of this feature is discussed in Sec. 3.3.3.

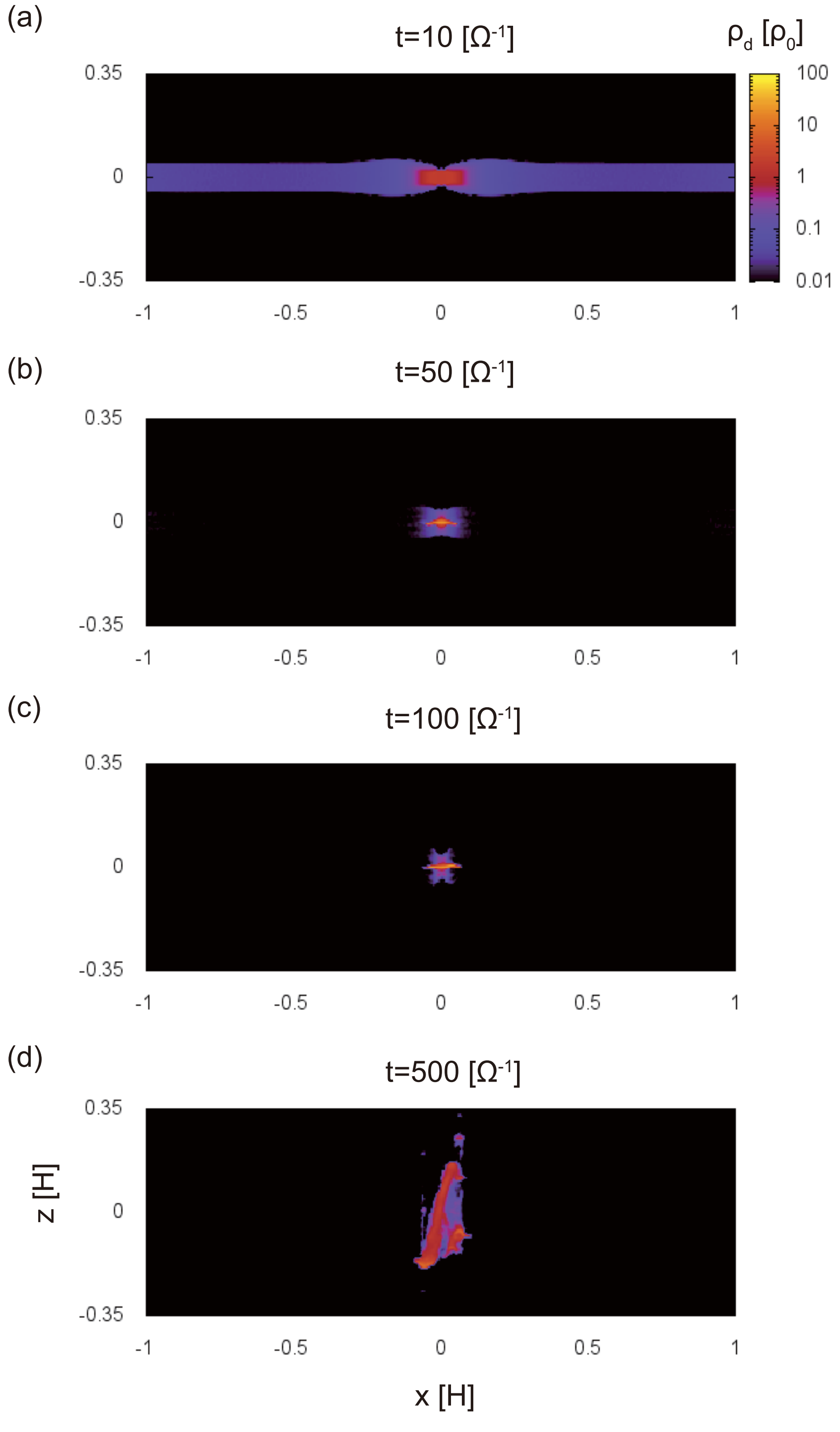

FIGURE 3.13: Same plots as Fig. 3.2 except that the dust surface density $\Sigma_d = 0.005\Sigma_g$.

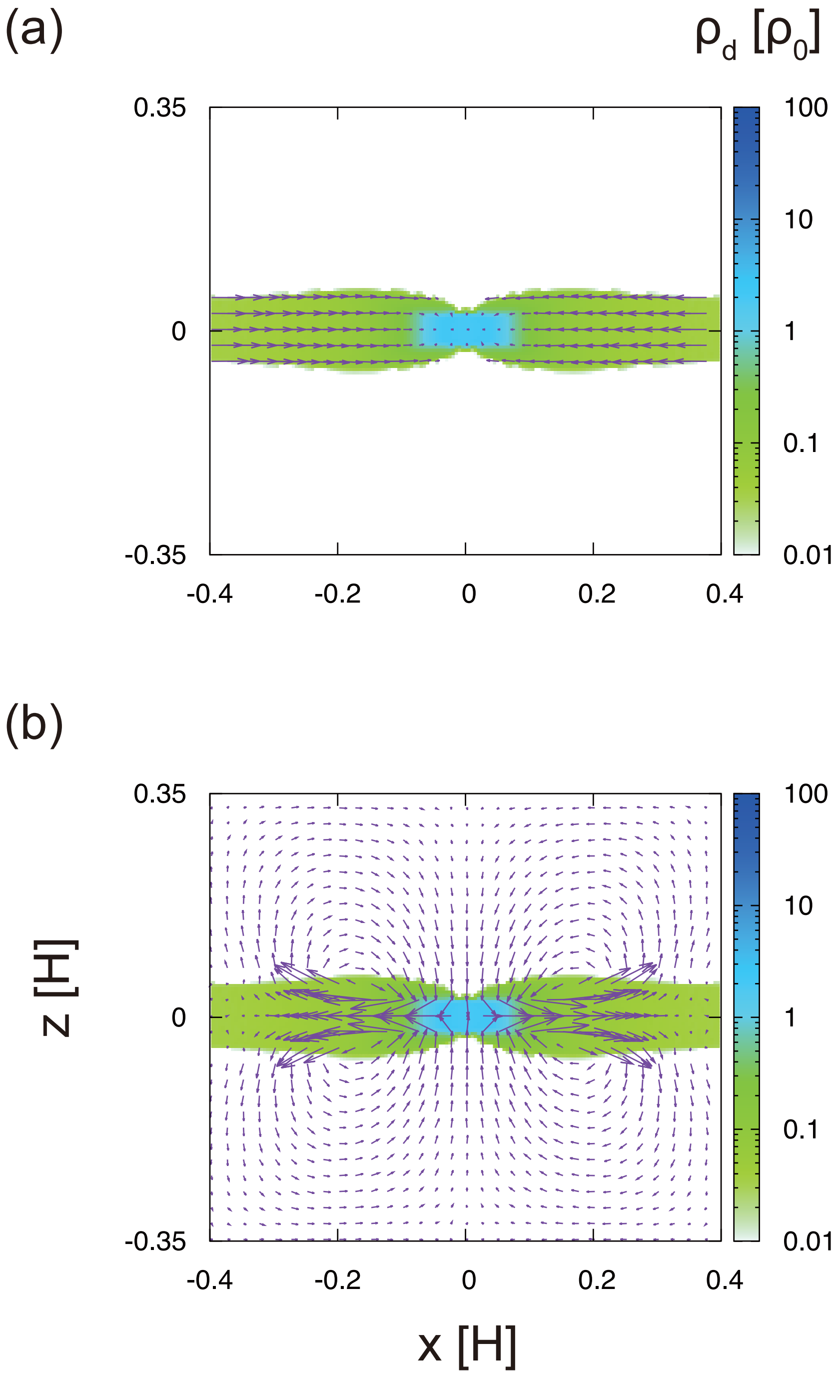

FIGURE 3.14: Same plots as Fig. 3.3 except that the dust surface density $\Sigma_d = 0.005\Sigma_g$.

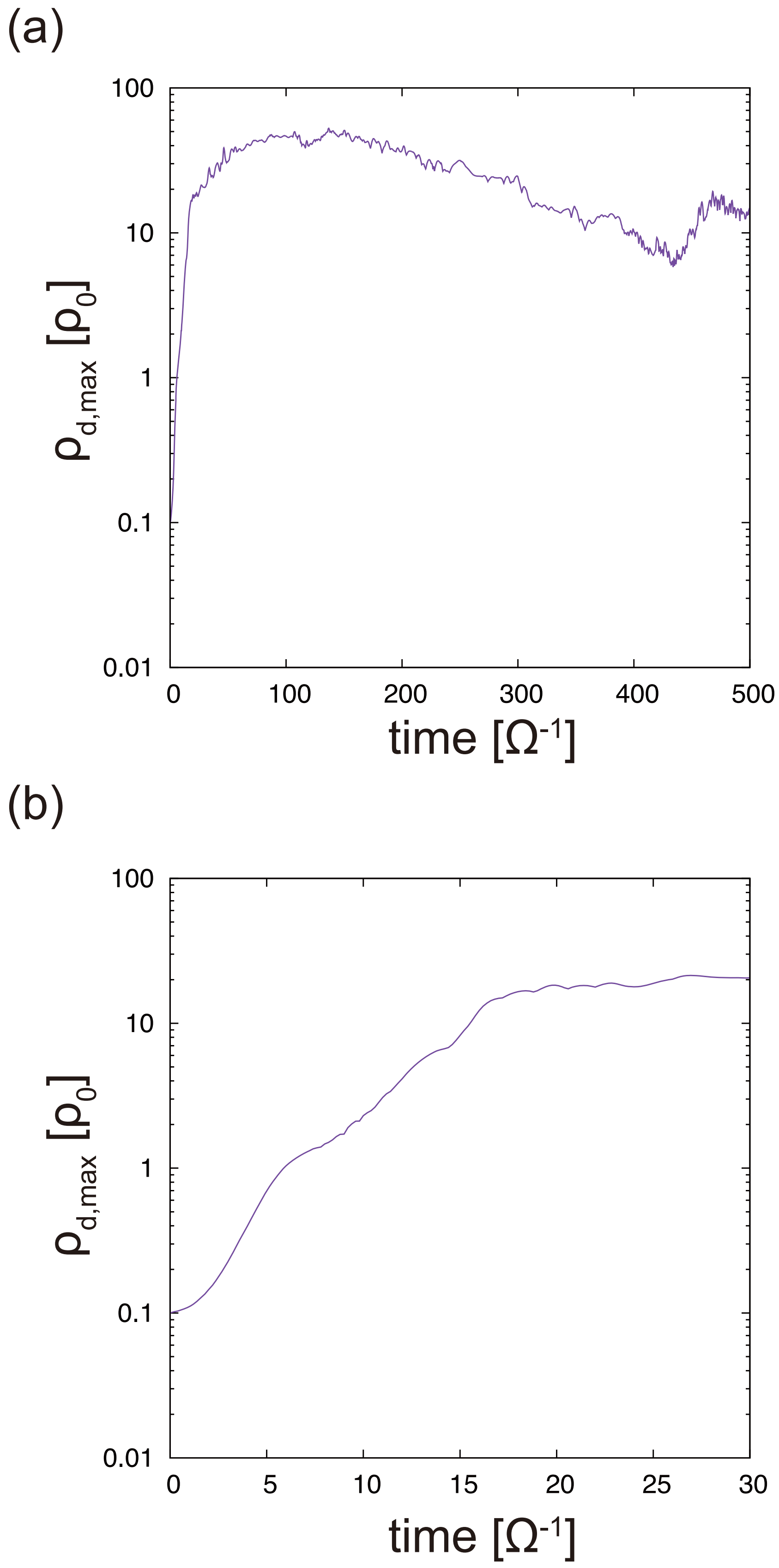

FIGURE 3.15: Same plots as Fig. 3.5 except that the dust surface density $\Sigma_d = 0.005\Sigma_g$. The peak value of the maximum density is slightly lower than run – (case with $\Sigma_d = 0.01\Sigma_g$).

3.2.5 Effect of the Width of the Dust Layer

Width of the dust layer should affect the dust and gas density evolution at the pressure bump. This is because that the case with the wider dust layer may converge to the case with $H_{\rm d} = H_{\rm g}$ which may accord to the result of the 1-D case (see run β04-1D of Chap. 2). In previous calculations, the width of the dust layer is fixed at $0.1H$ which corresponds to the result of Youdin and Lithwick (2007) at turbulent parameter $\alpha = 10^{-3}$. The larger value of α means the larger dust scale height. Now we test the case that the width of the dust layer $L_{\rm p}$ is $0.2H$.

Fig. 3.16 shows that the evolution of the maximum dust density for run C4-05 (purple line) and C4-06 (green line). Since the run C4-06 is computationally expensive, the total run time $t_{\rm end}$ of this case is $\sim 200\Omega^{-1}$ which is shorter than other runs. However the $t_{\rm end} = 200\Omega^{-1}$ is enough to investigate the peak value of the maximum dust density. The peak value in run C4-06 is $\sim 50\rho_0$ which is same with the fiducial run. The result of run C4-05 is not converged due to the small box size. So the peak value of run C4-05 may be incorrect, but qualitative evolution of the maximum dust density is not changed (see also Sec. 3.3.2). The qualitative trend is same with the fiducial case.

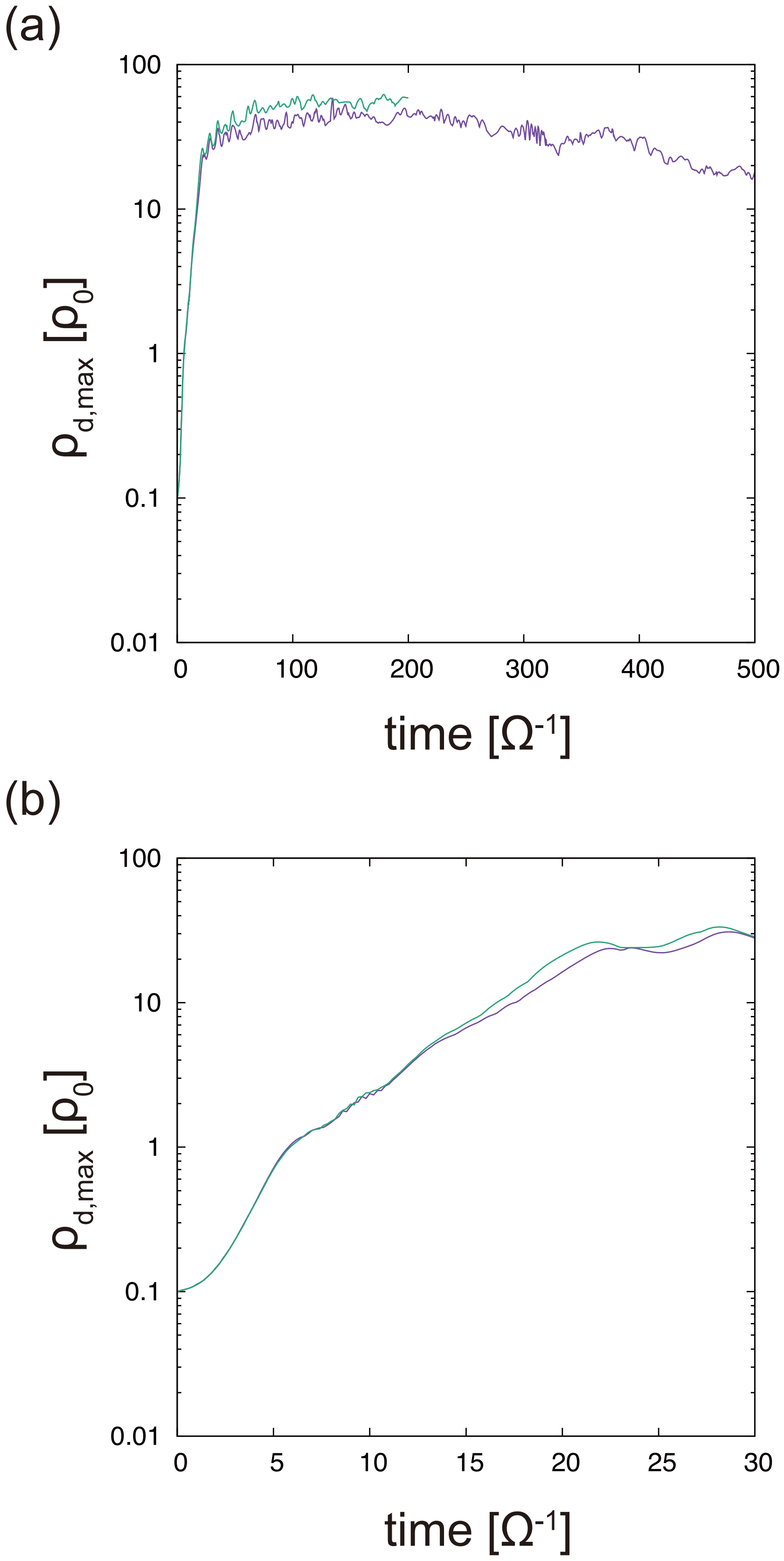

FIGURE 3.16: Same plots as Fig. 3.5 but for cases with broad dust layer. Panel (b) is an enlarged view of panel (a). The purple and green lines represents the result of run – and –, which has the vertical box size $L_z = 0.7H$ and $1.0H$, respectively.

3.2.6 Case with Small Dust Particles

For simplicity and saving of the computational cost, the stopping time of dust particles are fixed as $\tau_{\rm s}\Omega = 1.0$ in previous runs. However, a main component of the accreting dust flow is smaller dust particles as $\tau_{\rm s}\Omega \lesssim 0.1$ (Okuzumi et al. 2012; Birnstiel et al. 2012). The smaller particles have the smaller stopping time, then these particles are kicked by gas turbulence more effectively. In addition, the smaller particles have the smaller radial drift velocity (Nakagawa et al. 1986). These two effects prevent the dust accumulation and delay the pressure bump deformation. In this subsection, we conduct simulations for two test cases as $\tau_{\rm s}\Omega = 0.1,\ 0.01$ and compare their results with a fiducial stopping time $\tau_{\rm s}\Omega = 1.0$.

Fig. 3.17 is a comparison of the maximum dust density evolution for three cases. The purple curve represents a result of the fiducial stopping time (run C4-09). Other two curves (green, cyan) correspond to the case with $\tau_{\rm s}\Omega = 0.1, 0.01$, respectively. It is easy to see that the maximum dust density for small stopping time are significantly smaller than the fiducial case. Especially, in the case with $\tau_{\rm s}\Omega = 0.01$, the dust-to-gas mass ratio does not increase even to the unity.

These significant differences can be understood by the dust density patterns. Fig. 3.18 and 3.19 shows that the snapshots of the dust density pattern for $\tau_{\rm s}\Omega = 0.1$ and 0.01, respectively. In the case with $\tau_{\rm s}\Omega = 0.1$, the dust dense region where the dust-to-gas ratio ~ 1 is certainly formed and following vertical compression occurs. A vertical width of the dust dense region is larger than the fiducial case, i.e., the vertical compression is weak. Besides, in the case with $\tau_{\rm s}\Omega = 0.01$, the dust dense region is not formed any more. The pressure bump intend to accumulate the dust particles. But the dust particles are diffused in radial and vertical direction. This is because the small dust particles strongly couple with the disk gas. The radial drift of thin dust layer drives the gas turbulence. The small particles are strongly mixed by this self-regulated turbulence due to the small stopping time.

Note that the vertical box sizes are smaller than the size of the fiducial run R4-01 in this sub-section for saving of a computational cost. We discuss the convergence of maximum dust density due to the vertical box sizes in

Sec. 3.3.2. We only show that the qualitative result of the small stopping time cases in this subsection.

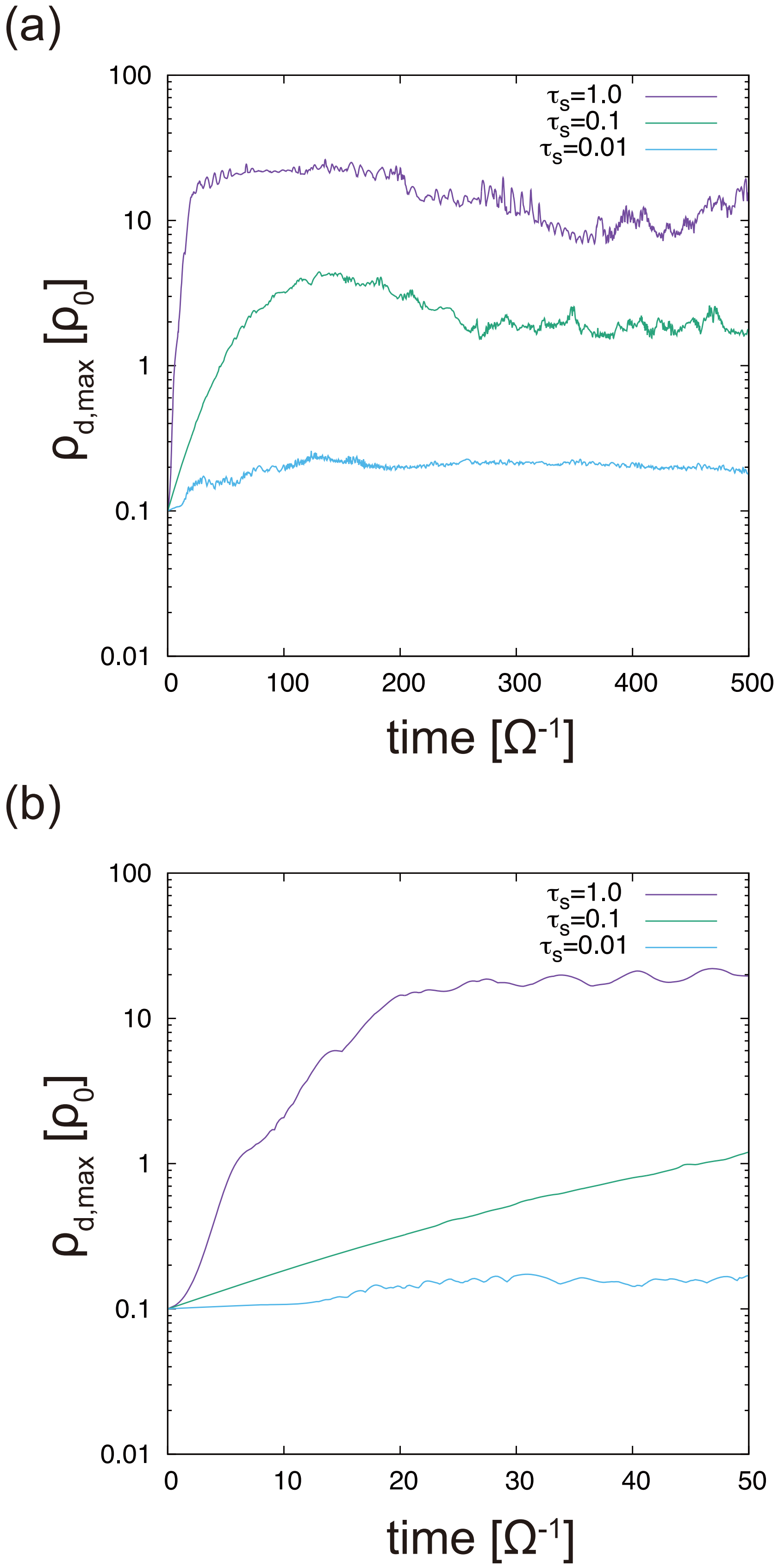

FIGURE 3.17: Comparison of the maximum dust density evolution between the different stopping times, $\tau_s = 1.0$ (fiducial model; purple line), 0.1 (run –; green line), 0.01 (run –, cyan line). A case in smaller stopping time achieves smaller peak value of the maximum dust density. Especially, in run –, the peak value is obviously smaller than 1. Panel (b) is the enlarged view of the initial phase of the panel (a).

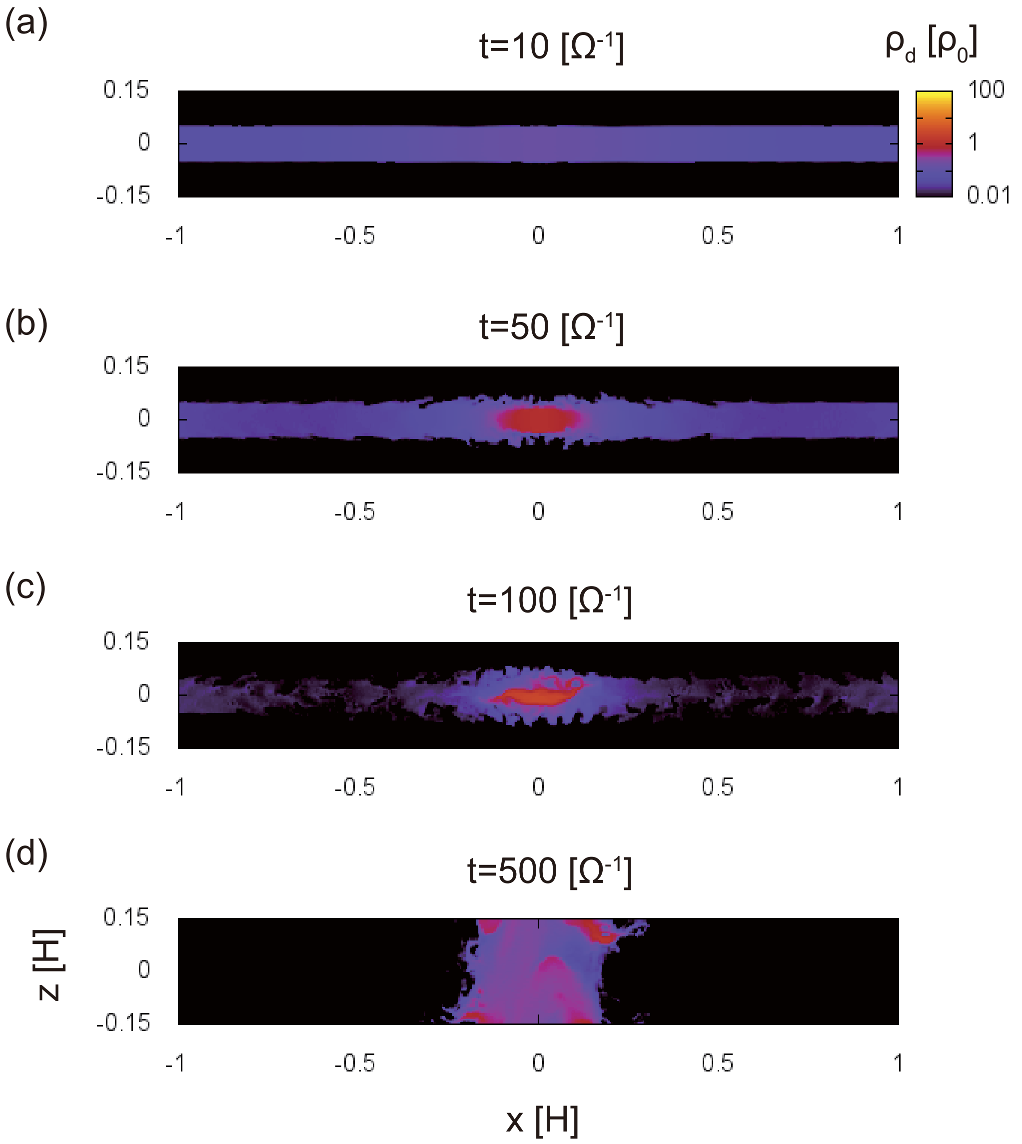

FIGURE 3.18: Same plots as Fig. 3.2 but for $\tau_s = 0.1$.

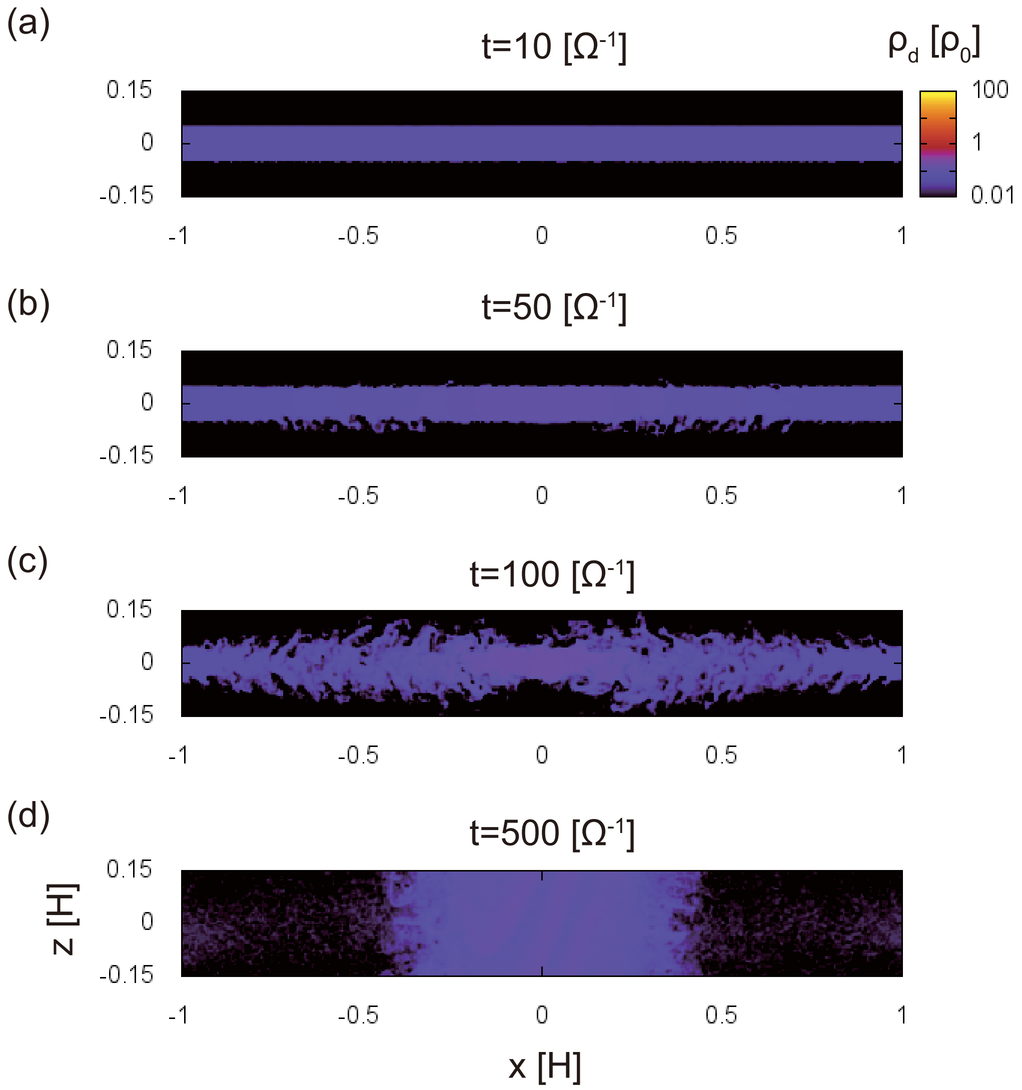

FIGURE 3.19: Same plots as Fig. 3.2 but for $\tau_s = 0.01$.

3.3 Discussion

3.3.1 Schematics of Pressure Bump Evolution

We found that the vertical compression of dust dense region in the previous section. In this subsection, we explain the formation mechanism of the vortices. We also discuss the formation mechanism of the vertically compressed dust dense region.

The gas vortices are naturally induced by the angular momentum exchange between dust and gas at the midplane dust layer. When the angular momentum exchange only occurs near the midplane, the gas outward flow from the pressure bump exists only near the midplane dust layer. Then the midplane gas density decreases due to the outward gas flow, the vertical force balance is broken. The negative pressure gradient forces which face to the midplane are induced in vertical direction. So the gas flow pattern at the pressure bump is radially outward and vertically inward flow which represented in Fig. 3.3. Note that the gas velocity is smaller than the sound speed of the gas, so the gas flow behave as an incompressible fluid.

While the gas flow pattern liked vortices, the dust dense region is compressed unilaterally but not diffused in radial direction. This is because the conservation of the angular momentum inhibits the dust particles from diffusing radial direction. The angular momentum which produces the gas outward flow supply from the dust particles. Therefore the radial dust flow should be alternating with the gas flow. On the other hand, the vertical flow is independent to the angular momentum redistribution process. Then the dust particles are dragged by gas inward flow in vertical direction. As a result, the dust dense region is compressed by the vortices like gas flow and the density increases significantly.

Note that, after bump deformation is finished, the dust particles are mixed in vertical direction. It is observed that the gas turbulence does not dissipate after forming the dust dense region, especially the edge of the dust dense region. This continuous gas turbulence mixes the dust particles at the dust dense region. In our calculations, we neglect the vertical gravity of host star. When the vertical gravity is included, the dust mixing may become more inefficient.

3.3.2 Convergence Test for the Vertical Length of of the Computational Domain

The largest size of vortices which are able to form in simulations is confined by sizes of computational domain. When the computational domain is smaller than the actual vortices size, the wrong gas flow pattern may be observed. The compression of the dust dense region is induced by the gas flow pattern. Therefore the wrong flow pattern might affect the peak value of the dust density at the dust dense region.

On the other hand, the actual largest size of vortices is loosely confined by the gas scale height of the protoplanetary disk. So maximum size of computational domain should be $L_z \sim 2H$. However, from the aspect of the computational cost, we conduct the convergence test of the vertical box size for $L_z/H = 0.3, 0.5, 0.7, 0.9, 1.1, 1.3$.

Fig. 3.20 shows that the comparison of the maximum dust density evolution. These results are almost converged at $L_z = 0.7H$. We confirm the gas flow pattern for various box seizes in Fig. 3.21. It seems that the larger computational box forms the larger vortices like pattern. However the flow pattern around the dust layer is almost converged at $L_z = 0.7H$. This indirectly suggest that the gas flow pattern around the midplane define the maximum dust density of the dust dense region certainly.

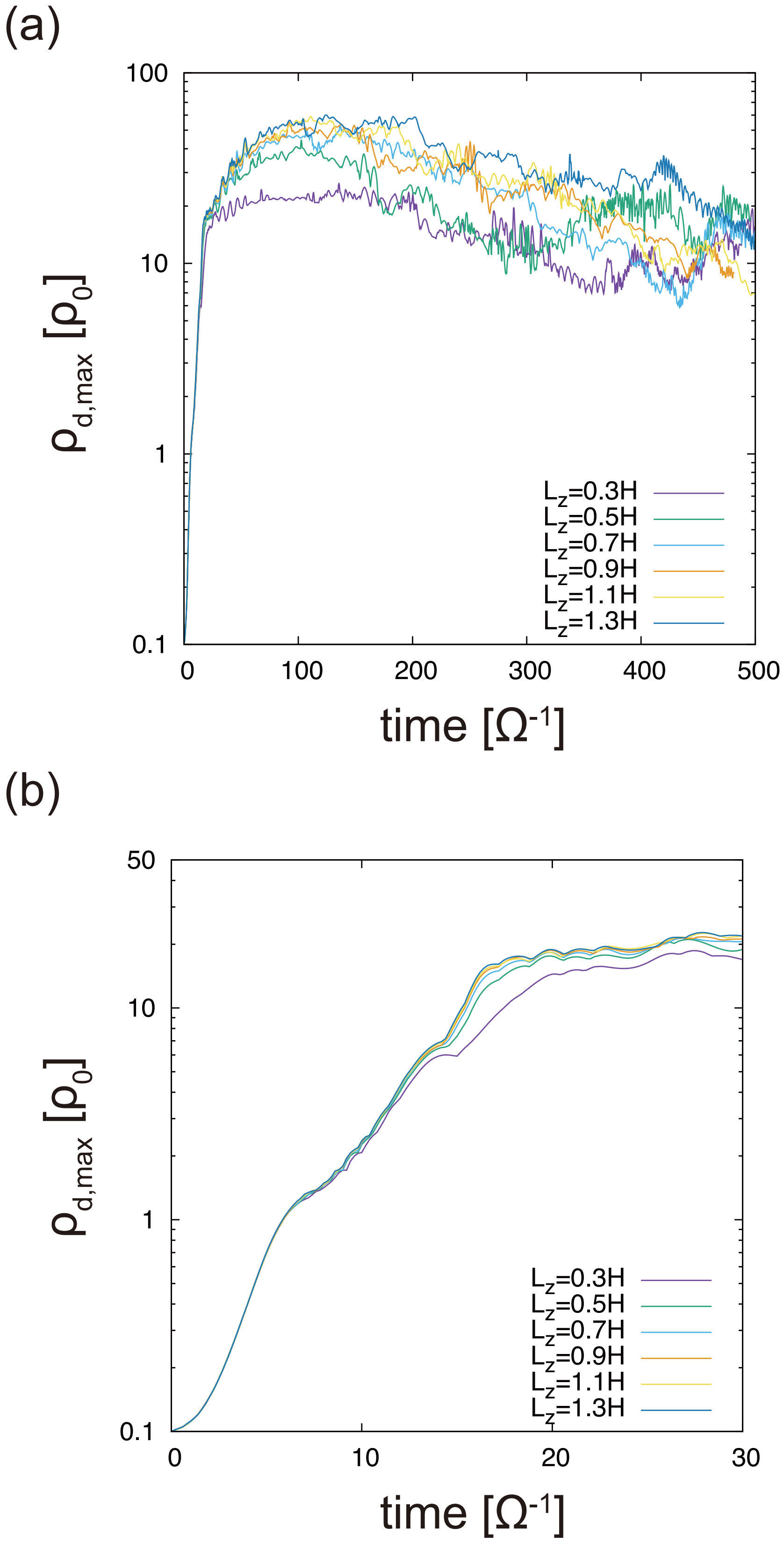

FIGURE 3.20: Convergence test of the maximum dust density. Panel (b) is the enlarged view of the initial phase of the panel (a). All lines represents the maximum dust density explained in Fig. 3.5. The different lines show the different box sizes in vertical direction. Final state of the dust density is almost same in all runs, $\rho_{\rm d,max} \sim 10$. Initial phase of time evolution is almost converged at $L_z \geq 0.7H$.

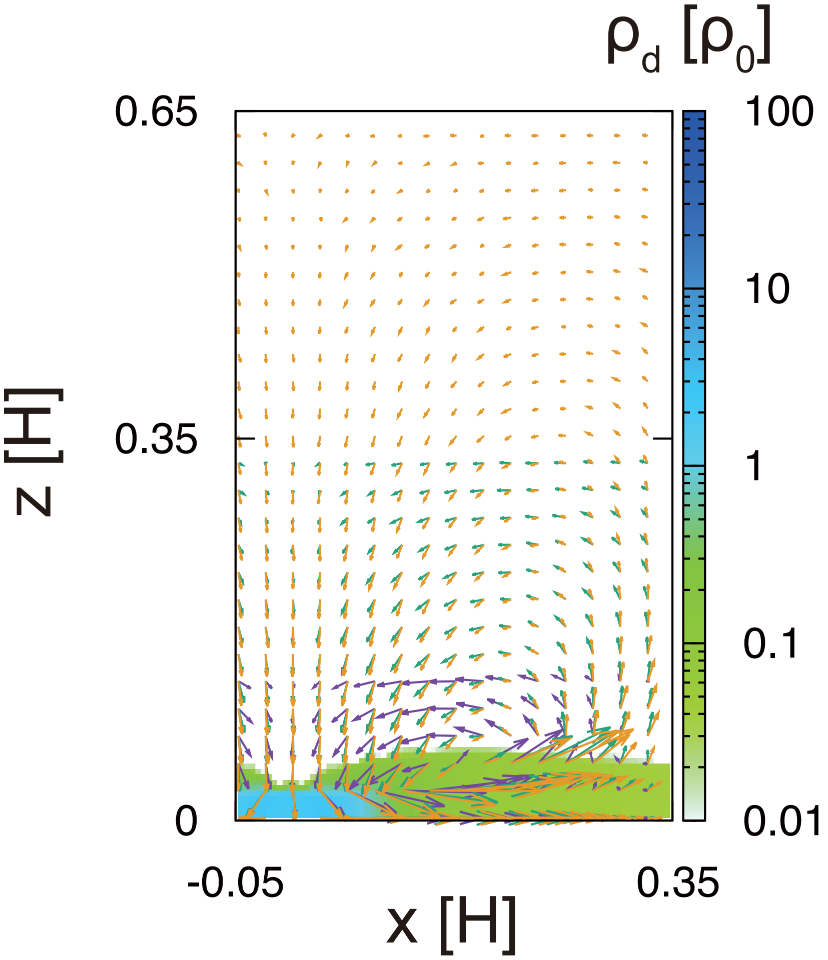

FIGURE 3.21: Comparison of the gas velocity field between different box sizes. Arrows represent the gas velocity in run – ($L_z = 0.3H$; purple arrows), run – ($L_z = 0.7H$; green arrows), and run – ($L_z = 1.3H$; yellow arrows), respectively. Contour shows the dust density distribution in run – ($L_z = 0.3H$). While the larger computational box forms the larger vortex, the direction of gas flow near the dust layer is almost converge in $L_z = 0.7H$.

3.3.3 Effect of the Initial Condition to the Maximum Dust Density

We conduct the simulations for various settings in Sec. 3.2. We found that the existence of global pressure gradient does not affect the vertical compression process. The existence of dust particles at initial pressure bump is also confirmed that the initial condition has no relation with the dust accumulation process.

The effect of the initial width of the dust layer is as follows. We calculated the case with $L_{\rm p} = 0.2$ corresponds to relatively strong turbulence. At this situation, the vertical compression occurred. However small particles which are strongly coupled with gas and have the large scale height $\sim H_{\rm g}$ is unfavorable for this process. At strong coupling or strong turbulent limit (i.e. at a case with $H_{\rm p} = H_{\rm g}$), the dust and gas density evolution might converge to simple 1-D model, presented in Sec. 2.2.

We also confirm the effect of the surface density. In Sec. 3.2.4, we test the case with small surface density of dust. The time evolution of the maximum dust density does not different from the result of fiducial run. In addition, the vertical flow is not changed significantly. This is because the deformation process is dominated by the evolution of the dust dense region, ~ 1. Therefore, once the dust-to-gas ratio achieves ~ 1 at the pressure maximum, the evolution of the maximum dust density does not depend on the initial dust surface density. On the other hand, required time of entirely deformation of pressure bump may depend on the dust surface density due to the small momentum flux of the dust.

The initial dust sizes affect the dust accumulation process strongly. For small stopping time case, the vertical compression is weaken. The dust particles are rather accumulated than diffused by the self-regulated turbulence. This diffusion is not observed in the case with uniform initial condition in vertical direction.

3.3.4 Vertical Homogeneity of the Gas Pressure Profile

When the vertical gravity is included, the following sedimentation of dust particles will occur. It is known that the thin dust layer required by the classical gravitational instability drives the shear instability due to the shear of the azimuthal velocity in vertical direction. Therefore the condensation of the dust layer is prevented by the turbulent diffusion.

Fig. 3.4 shows that the pressure bump flattened by the midplane dust layer has no vertical variation for the pressure. It means that the flattened pressure bump rotates as uniform azimuthal velocity in vertical direction.

In addition, in equilibrium state, the dust and gas azimuthal velocity is almost same as the Keplerian velocity. Therefore there is no azimuthal velocity shear in vertical direction at the pressure bump. This property may encourage the farther condensation of dust dense region.

Chapter 4

Growth of Dust Particles at a Radial Pressure Bump

4.1 Method

4.1.1 Basic Equations

We found that the radial pressure bump is a promising location for the dust growth in Chap. 2. Therefore, we include the dust coagulation process in our dynamical model and investigate the effect of the dust growth to the dust and gas density evolution at the radial pressure bump. The dust and gas dynamics are calculated by the same equations with Sec. 2.1. For simplicity, we use 1-D (radial) model. To consider the rocky planetesimal formation, the orbital radius of our local computational box is $r = 1\mathrm{AU}$ in this chapter. Various parameters of the protoplanetary disk model is employ the parameters of the MMSN model (Hayashi et al. 1985).

To couple a process of dust growth with a dynamics of dust and gas self-consistently, we should calculate the coagulation equation in each time steps of the computational fluid dynamics simulations. However the actual coagulation (Smoluchowski) equation is too expensive computationally. Sato et al. (2016) derived the simplified coagulation equations referred to as “the single size approach”. The original form of the vertically integrated coagulation equation (Brauer et al. 2008a) calculates the column number density of dust particles N as a function of the particle mass m and the dust scale height h_d. On the other hand, the single size approach calculates the evolution of the total dust surface density Σ_d and the peak mass m_p which are expressed as

$$\Sigma_\mathrm{d} \equiv \int_0^\infty S(m)\mathrm{d}m, \tag{4.1}$$

$$m_\mathrm{p} \equiv \frac{\int mS\mathrm{d}m}{S\mathrm{d}m}, \tag{4.2}$$

where S is the surface mass density of dust per unit particle mass as

$$S(r,m) = mN(r,m). \tag{4.3}$$

Then they employ two assumptions. The S is a unimodal function of m corresponds to the case when the S is approximately equal to the mass at the peak of S (Ormel and Spaans 2008). And the S is narrowly peaked at $m \approx m_\mathrm{p}$. Under this assumptions, they obtained the simplified equations from vertically integrated coagulation equation as (Sato et al. 2016)

$$\frac{\partial m_\mathrm{p}}{\partial t} + v_r \frac{\partial m_\mathrm{p}}{\partial r} = \frac{2\sqrt{\pi}a^2 \Delta v_\mathrm{pp}}{H_d}\Sigma_d, \tag{4.4}$$

$$\frac{\partial \Sigma_d}{\partial t} + \frac{1}{r}\frac{\partial}{\partial r}\left(r v_r \Sigma_d\right) = 0. \tag{4.5}$$

Fig. 4.1 shows that the comparison between single and full-size coagulation calculations. The single size approach is a good approximation to calculate the size and density evolution of the dust particles.

We rewrite these equations as the equations of Lagrangian method. In our simulations, the dust particles are treated as super-particles. Hence, Lagrangian method is compatible with our simulations. The size evolution equations are rewritten as

$$\frac{\mathrm{d}m_p}{\mathrm{d}t} = \frac{2\sqrt{\pi}a^2 \Delta v_{pp}}{h_d}\Sigma_d, \tag{4.6}$$

$$\Delta v_{pp} = \sqrt{(\Delta v_B)^2 + (\Delta v_r)^2 + (\Delta v_\phi)^2 + (\Delta v_z)^2 + (\Delta v_t)^2} \tag{4.7}$$

$$t_s = \begin{cases} \dfrac{\rho_\mathrm{int} a}{\rho_g v_\mathrm{th}}, & a < \dfrac{9}{4}\lambda_\mathrm{mfp}, \\ \dfrac{4\rho_\mathrm{int} a^2}{9\rho_g v_\mathrm{th} \lambda_\mathrm{mfp}}, & a > \dfrac{9}{4}\lambda_\mathrm{mfp}, \end{cases} \tag{4.8}$$

The equation of continuity is automatically fulfilled because of the particle approach.

The $\Delta v_{\rm pp}$ is relative velocity between dust particles. The relative velocities due to the dust motion in radial and azimuthal direction $\Delta v_r, \Delta v_\phi$ is obtained by the calculation of the particle dynamics. The vertical velocity of dust particles which marginally decoupled with gas is not unique. This is because that these dust particles move as the damped oscillation in vertical direction. However the order of the vertical velocity is nearly equal of lower than the radial or azimuthal velocity (see Fig. 4.2). So we neglect the vertical velocity in our simulations for simplicity.

Other components of the relative velocities are expressed as follows:

$$\Delta v_B = \sqrt{\frac{8(m_1+m_2)k_{\rm B}T}{\pi m_1 m_2}}, \tag{4.9}$$

$$\Delta v_t \approx \begin{cases} \delta v_g {\rm Re}_t^{1/4}\Omega|t_{s,1}-t_{s,2}|, & t_{s,1} \ll t_\eta, \\ (1.4\dots1.7)\times\delta v_g\sqrt{\Omega t_{s,1}}, & t_\eta \ll t_{s,1} \ll \Omega^{-1}, \\ \delta v_g\left(\dfrac{1}{1+\Omega t_{s,1}}+\dfrac{1}{1+\Omega t_{s,2}}\right)^{1/2}, & \Omega t_{s,1} \gg 1, \end{cases} \tag{4.10}$$

$\Delta v_{\rm B}$ is a relative velocity due to the Brownian motion of dust particles. A velocity of the Brownian motion is

$$\begin{aligned} v_B &\cong \sqrt{\frac{8k_BT\times 2m_d}{\pi m_d^2}} \\ &= 4.84\times\left(\frac{r}{1{\rm AU}}\right)^{-1/4}\left(\frac{L}{L_\odot}\right)^{1/8}\left(\frac{\rho_{\rm int}}{2.0\ {\rm g\ cm^{-3}}}\right)^{-1/2}\left(\frac{a}{0.1\mu{\rm m}}\right)^{-3/2}\ {\rm cm/s}. \end{aligned} \tag{4.11}$$

The order of this component is $\sim 10^{-5}$ cm/s for mm-sized particles. Since the value is significantly smaller than other components, we neglect this term in our simulations. The $\Delta v_{\rm t}$ is a relative velocity due to the turbulence. The expression is derived by Ormel and Cuzzi (2007). The turbulent Reynolds number is expressed as

$${\rm Re}_t = 2\alpha c_s h_g v_{\rm th}^{-1}\lambda_{\rm mfp}^{-1} \cong 5.7\times10^7\times\left(\frac{\alpha}{10^{-3}}\right)\left(\frac{r}{1{\rm AU}}\right)^{-3/2}. \tag{4.12}$$

The eddy turnover time of smallest vortices is

$$t_\eta = t_L/\sqrt{\mathrm{Re}_t} \cong 1.3 \times 10^{-4} \times \left(\frac{\alpha}{10^{-3}}\right)^{-1/2} \left(\frac{r}{1\mathrm{AU}}\right)^{3/4} \times \Omega^{-1}. \tag{4.13}$$

Then we rewrite the turbulent relative velocity as

$$\Delta v_t \approx \begin{cases} \sqrt{\alpha} c_s \mathrm{Re}_t^{1/4} \Omega |t_{s,1} - t_{s,2}|, & \Omega t_{s,1} \ll \Omega t_\eta, \\ (1.4 \ldots 1.7) \times \sqrt{\alpha} c_s \sqrt{\Omega t_{s,1}}, & \Omega t_\eta \ll \Omega t_{s,1} \ll 1, \\ \sqrt{\alpha} c_s \left(\dfrac{1}{1+\Omega t_{s,1}} + \dfrac{1}{1+\Omega t_{s,2}}\right)^{1/2}, & \Omega t_{s,1} \gg 1, \end{cases} \tag{4.14}$$

Since we consider the dust particles larger than the mm-sized bodies, the first regime of turbulent relative velocity is negligible. Finally, we obtain the turbulent relative velocity of our simulations as

$$\Delta v_t \approx \begin{cases} 1.7 \times \sqrt{\alpha St_1} c_s, & St_1 < 1, \\ \sqrt{\alpha} \left(\dfrac{1}{1+St_1} + \dfrac{1}{1+St_2}\right)^{1/2} c_s, & St_1 \geq 1, \end{cases} \tag{4.15}$$

We assume that the perfect sticking and compact growth for dust coagulation process (see Okuzumi et al. (2012)) The relation between the particle radius a and the peak mass m_p is $m_p = 4\pi\rho_{\mathrm{int}} a^3/3$. Therefore the coagulation equation is

$$\frac{\mathrm{d}a}{\mathrm{d}t} = \frac{1}{\sqrt{2}} \frac{\Delta v_{pp} \rho_d}{\rho_{\mathrm{int}}}. \tag{4.16}$$

The dimensionless stopping time is also rewritten as

$$t_s = \frac{\rho_{\mathrm{int}} a}{\rho_g v_{\mathrm{th}}} \max\left\{1,\ \frac{4a}{9\lambda_{\mathrm{mfp}}}\right\} = \sqrt{\frac{\pi}{8}} \frac{\rho_{\mathrm{int}} a}{\rho_g c_s} \max\left\{1,\ \frac{4a}{9\lambda_{\mathrm{mfp}}}\right\}. \tag{4.17}$$

The coagulation equation, the particle relative velocity, and the stopping time are new equations using our model.

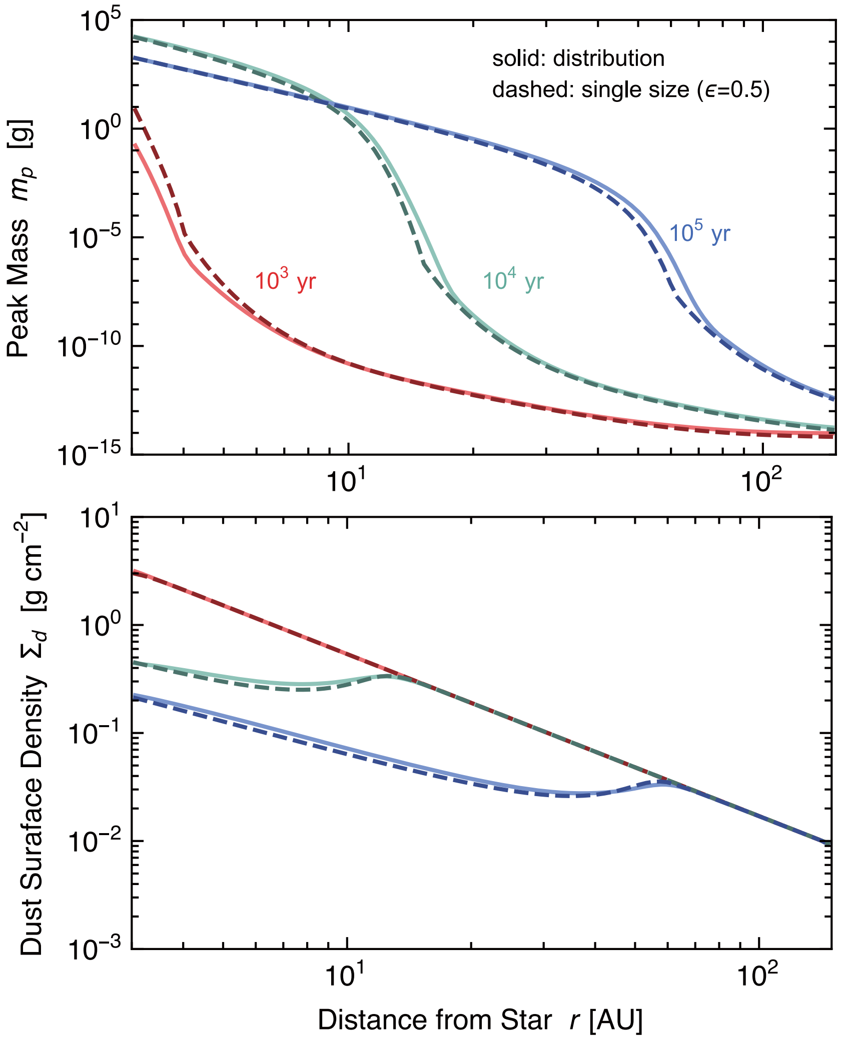

Figure 4.1: Comparison between results of single and full-size coagulation calculations. The calculations include the dust radial drift and compact coagulation. The solid lines show the snapshots of the peak mass m_p (upper panel) and total dust surface density (lower panel) at different times as a function of orbital radius r obtained from the full coagulation simulation for the compact aggregation model by Okuzumi et al. (2012). The dashed lines show the reproduction using the single-size approach. This figure is taken from Figure A.1 of Sato et al. (2016)

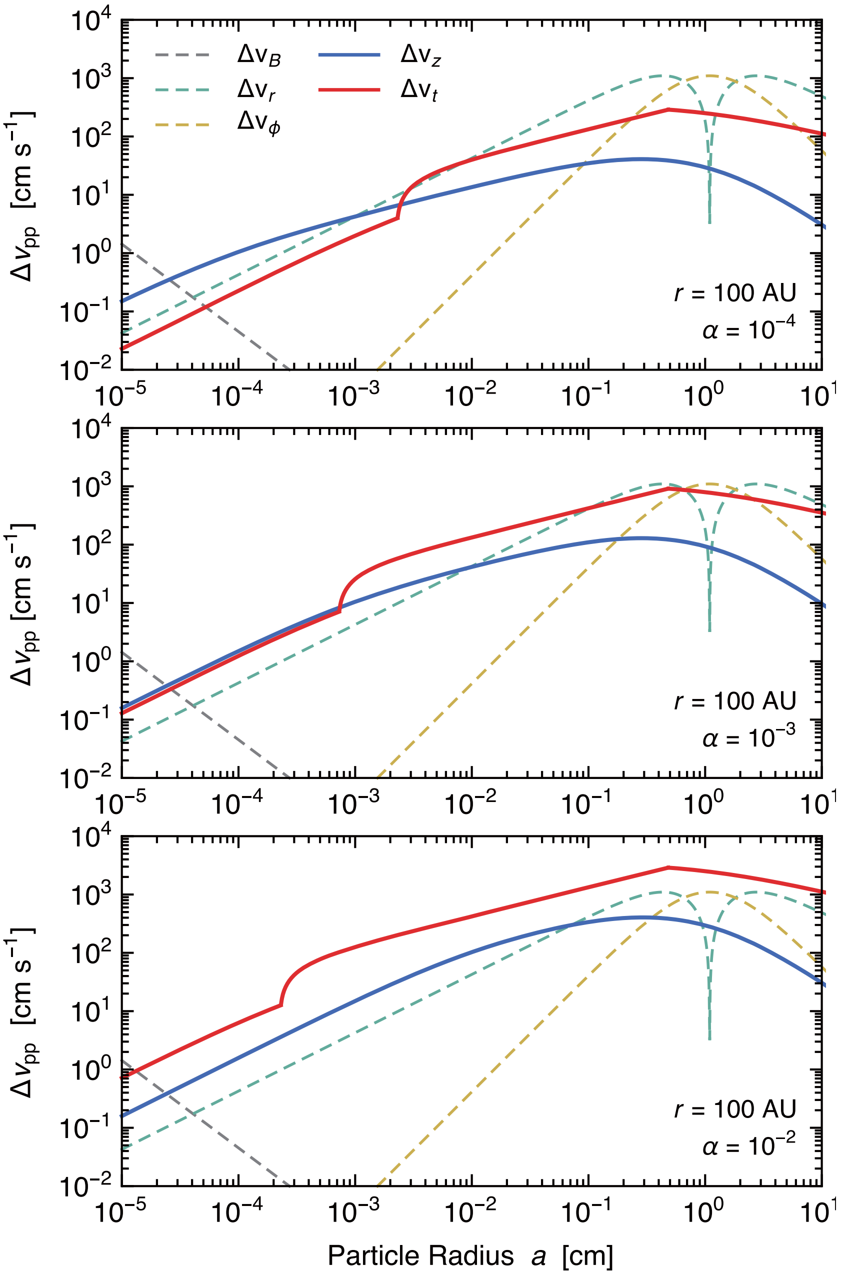

FIGURE 4.2: Comparison between components of the particle relative velocity $\Delta v_{\rm pp}$ at 100 AU as a function of particle radius a for three values of the turbulence parameter $\alpha = 10^{-4}$ (top panel), 10^{-3} (middle panel), and 10^{-2} (bottom panel). The velocity components that depend on α are shown by the solid curves. Note that the α parameter is fixed at 10^{-3} in this thesis. This figure is taken from Figure 2 of Sato et al. (2016).

Run	$L_x[H]$	ϵ_0	$\tau_{\rm s,ini}$	dust drag	supplemental particles
C5-01	5	0.1	~ 1.0	on	off
C5-02	5	0.1	~ 1.0	off	off
C5-03	5	0.1	$\sim 2.0 \times 10^{-4}$	on	off
C5-04	10	0.01	~ 1.0	on	off
C5-05	10	0.1	~ 1.0	on	off
C5-06	5	0.1	$\sim 10^{-3}$	on	on

TABLE 4.1: Setup of individual runs. L_x is the radial width of computational region. ϵ_0 is the initial dust-to-gas ration at the dust layer. $\tau_{\rm s,ini}$ is the initial value of the stopping time of dust particles. The"dust drag" represents the case with or without the dust drag force. When "supplemental particles" turns on, super-particles having the different size set in the simulation box at initial state (see Sec. 4.3.2). A size of the grid cell is fixed at $0.005H$ in all runs. The number of dust particles at each grid cells is also fixed in 10 particles. The total run time $t_{\rm end}$ is fixed in $500\Omega^{-1}$.

4.1.2 Initial Settings

The initial condition of the gas is almost same with the 1-D case of Chap. 2. We set the pressure bump as the initial condition. The azimuthal velocity profile sustain the bump structure (see also Sec. 2.1.2).

For simplicity, the initial dust radius is uniform for all super-particles in our fiducial run. The initial dust radius is ~ 100 cm which corresponds to the stopping time $\tau_{\rm s}\Omega \sim 1.0$. The dust spatial density is also uniform.

In previous chapters, the initial dust and gas velocities are the individual steady solution derived by the radial force balance of dust and gas, respectively. However, that settings have the unphysically large relative velocity between dust and gas at initial state. Since the coagulation equation depends on the relative velocity between dust particles, these artificial acceleration might be uncomfortable. Then, in this chapter, the initial velocities are given by the NSH equilibrium solutions (Nakagawa et al. 1986) for the sake of safety. Other parameters are summarized in Table 3.1

4.2 Results

4.2.1 Results of Fiducial Case

First, we show the results of the fiducial case (run R5-01). To understand the basic property of the dust and gas evolution with dust growth, we set the simple initial settings: no size distribution, the fastest radial drift, and small box size.

The dust dynamics is not so changed with the cases without dust growth. The panel (a) of Fig. 4.3 represents the dust density distribution at $t \approx 0, 16, 80$yr. The dust particles forms the dust dense region where the dust-to-gas mass ratio is ~ 1. This result is same with the previous chapters. The panel (b) of Fig. 4.3 represents the dust azimuthal velocity which is the deviation from the Keplerian velocity of each location. At dust dense region, the dust particles rotate near the Keplerian velocity. A restart of the dust inward drift does not occur in this case. The reason is discussed in Sec. 4.2.5.

At the dust dense region, the dust density is higher than the outside of the region, so the dust growth may be accelerated. Fig. 4.4 shows that the snapshot of the spatial distribution of the dust radius for the fiducial run. We can confirm that the radii of dust particles at the dust dense region are larger than the radii of outside dust particles. At the final state of our simulation, the maximum value of the dust radius is $\sim$ 10m.

The gas density evolution is represented in Fig. 4.5. The panel (a) of Fig. 4.5 represents the snapshots of the total gas pressure. The gas pressure gradient becomes nearly zero at the dust dense region. This tendency is also same with the result of cases without dust growth. On the other hand, the panel (b) shows the gas azimuthal velocity which is the deviation from the Keplerian rotation. It is confirmed that the gas also rotates as the Keplerian velocity nearly.

Fig. 4.6 shows the time evolution of the maximum dust radius which is the radius of the super-particle having the largest radius in whole computational domain. A quick growth at an early part of the evolution ($t \sim 1 - 10$yr) is produced by the dust accumulation at the pressure bump.

In this run, the dust particles continue their growth permanently at the dust dense region. The gradient of the growth curve at the late phase ($t \gtrsim 30$) is discussed in Sec. 4.3.1.

The radial drift velocity of the dust particles relate as the bump crossing time, the growth time. Whether the dust fragmentation occurs or not is also related with the radial drift velocity. Fig. 4.7 shows that the radial velocity of dust particles. At the outside of the dust dense region, the dust radial drift velocity is $\sim 0.01 c_s$ - $0.1 c_s$ which are $\sim$ 10m/s - 100m/s at orbital radius r = 1AU. The fragmentation velocity of rocky particles are $\sim$ 30m/s at a maximum. So the actual dust particles which fall into the pressure bump may be restricted by the fragmentation (Birnstiel et al. 2012). At the dust dense region, however, the dust radial velocity is significantly reduced as $\sim 10^{-5} c_s$-$10^{-4} c_s$ which are $\sim$ 1cm/s - 10cm/s at orbital radius r = 1AU This is comparable with or smaller than the hardest fragmentation velocity of rocky particles (Blum and Wurm 2008; Drazkowska and Dullemond 2014).

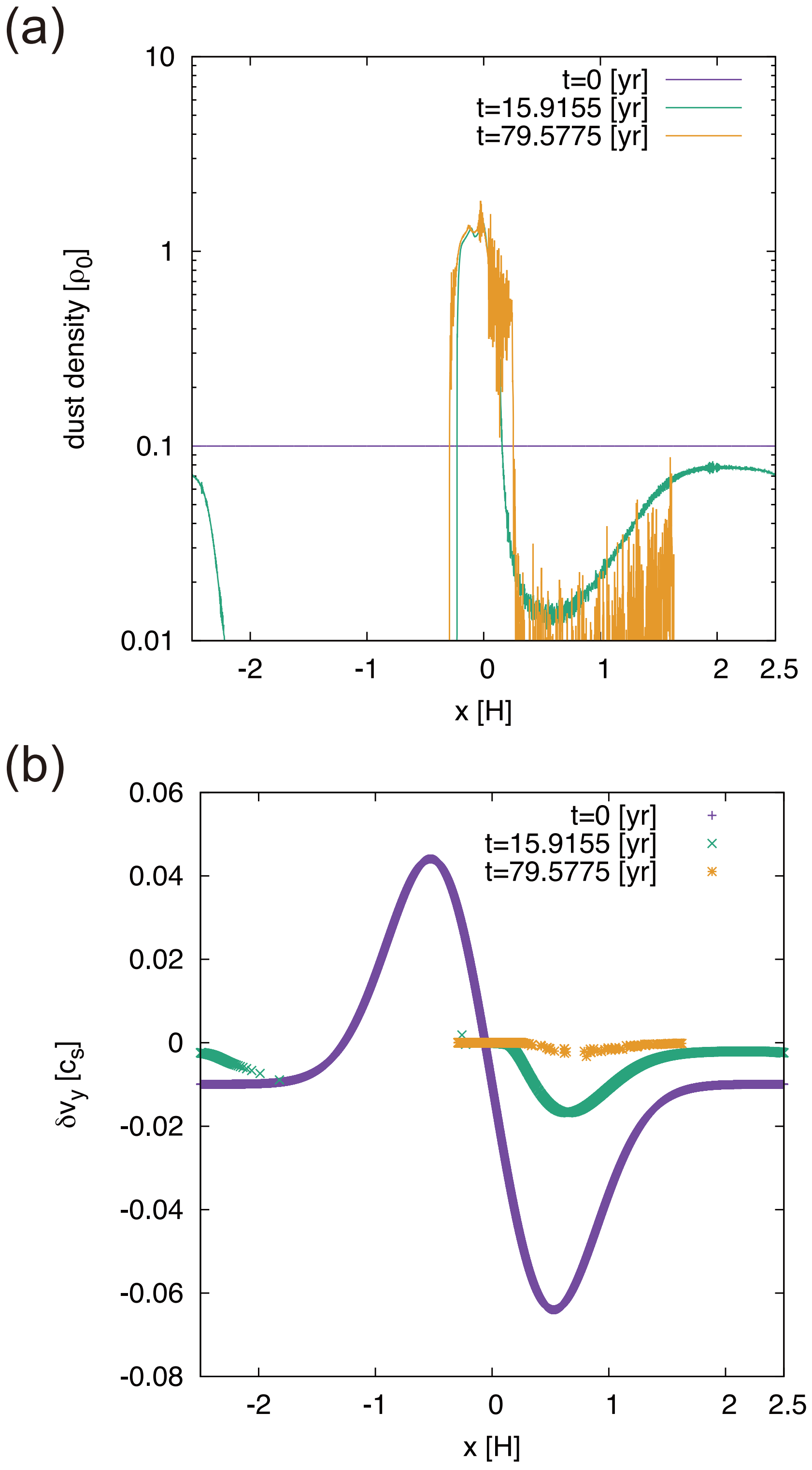

FIGURE 4.3: Result of the dust profile from the our fiducial model. (a) Dust density, and (b) dust azimuthal velocity (the deviation from the Keplerian velocity), respectively. The purple, green, yellow plots represent snapshots at $t \sim 0, 16, 80$ yr. The saturated dust density ~ 1 is same with the case with no growth (see Chap. 2). Note that the each points in panel (b) represent the each super-particles.

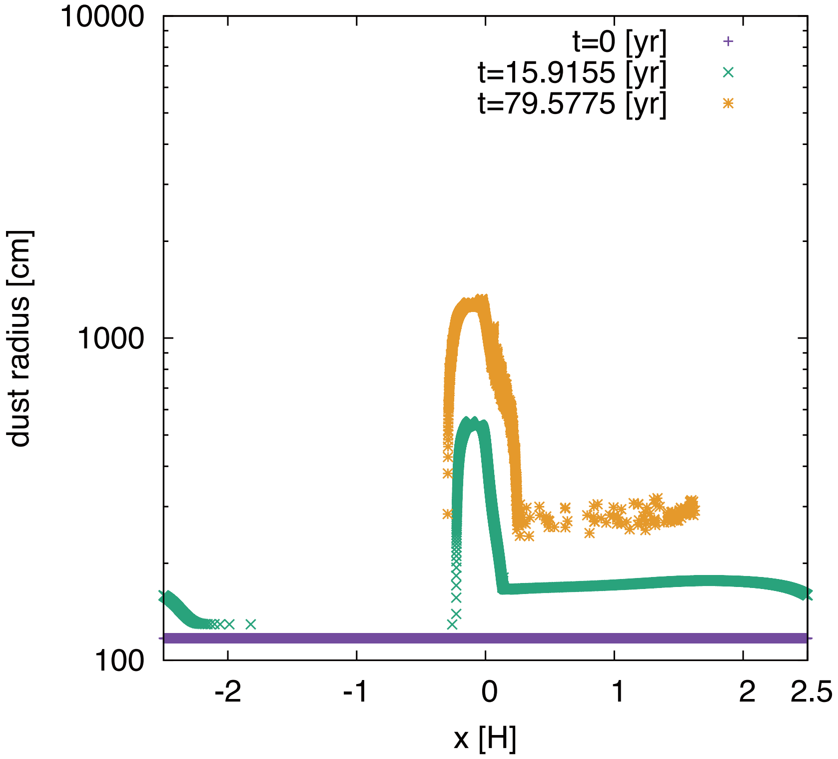

FIGURE 4.4: Snapshots of dust radius distribution in our fiducial model. The dust growth is encouraged at the dust dense region formed by the pressure bump (see around a center of the computational domain). Note that the each points in panel (b) represent the each super-particles.

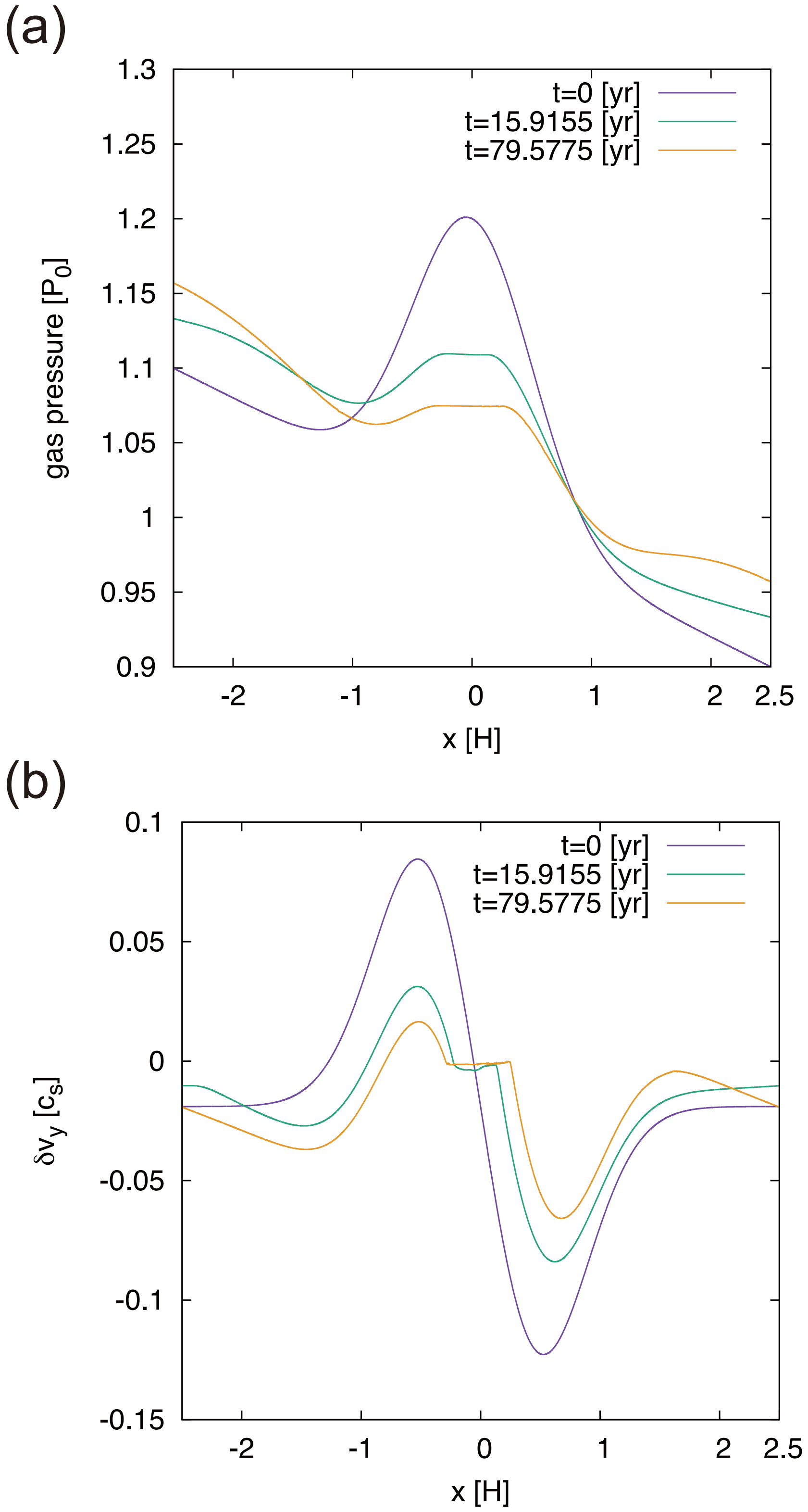

FIGURE 4.5: Result of the gas profile from the our fiducial model. (a) Gas pressure, and (b) gas azimuthal velocity (the deviation from the Keplerian velocity), respectively. The purple, green, yellow plots represent snapshots at $t \sim 0, 16, 80$ yr. The gas pressure is flattened at the dust dense region where the dust-to-gas ratio is ~ 1.

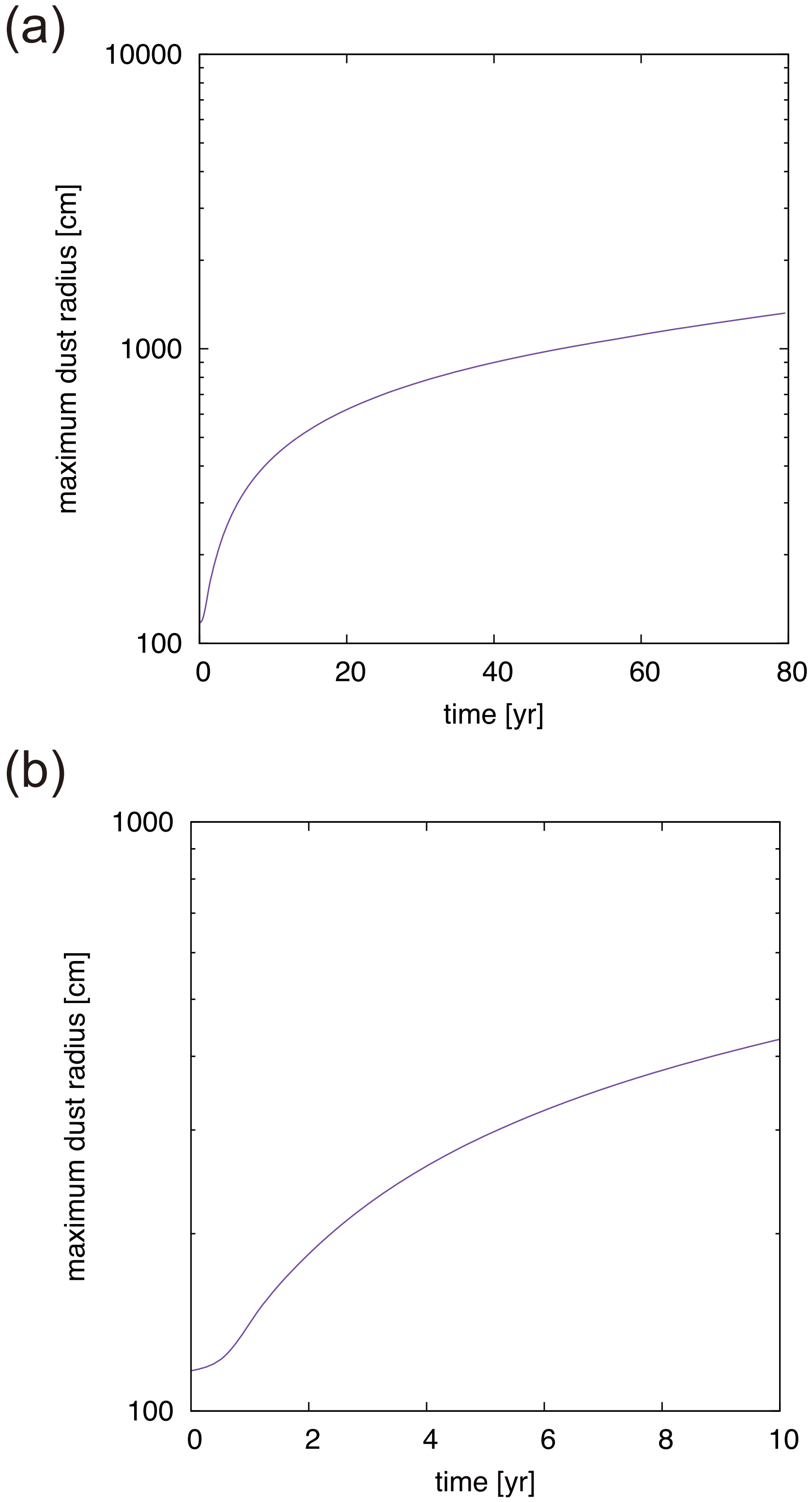

FIGURE 4.6: Time evolution of the maximum dust radius in run −. All lines represent the dust radius of the super-particle having the largest radius between all super-particles. Panel (b) is the enlarged view of the initial phase of the panel (a).

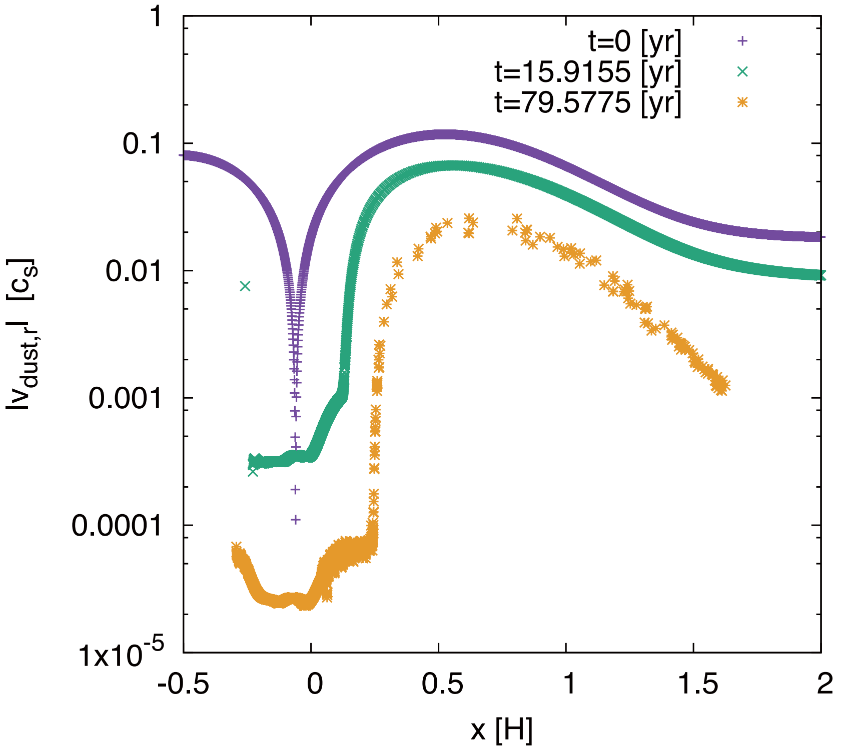

FIGURE 4.7: Absolute value of the dust radial velocity. The purple, green, yellow plots are snapshots at $t \sim 0, 16.80$yr, respectively. Each points represent each super-particles.

4.2.2 Case without the Dust Drag Force

Next, we test the case without dust drag force. This case corresponds to the case with quick restoration/formation of the pressure bump. Since the gas does not receive the angular momentum from dust particles, the gas profile is completely steady in this case.

Fig. 4.8 shows the spatial distribution of the dust density and the dust azimuthal velocity which is the deviation from the Keplerian velocity. Since the pressure bump is steady, the dust particles are accumulated at one or two grid cell which have the peak value of gas pressure. Until $t \approx 80$yr, almost all particles are trapped at the pressure maximum. The dust density achieves significantly high density. Note that the value of the maximum density is restricted by the size of the grid cell, so the absolute value of the dust density is determined by our numerical settings artificially.

Fig. 4.9 is the spatial distribution of the dust radius. At final state of the simulation, the all dust particles have the same position in radial direction and undergo the coagulation. The size range of these particles are determined by the order of the arrival at the pressure maximum, i.e., the particle trapped at first has the largest size and the latest particle has the smallest size.

The power of the evolution of the maximum dust radius is similar to the fiducial case (Fig. 4.10, see also Fig. 4.6) Since the dust density is significantly higher than the fiducial case, the absolute value of the radius is larger than the fiducial case. However, the dust density is saturated when all particles accumulated at the pressure maximum point exactly. The late phase of evolution can regard as the dust growth under the constant dust density and no drift velocity. Therefore the dust particles undergo the dust growth due to the turbulent relative velocity. The power of the size evolution corresponds to the power of the turbulent relative velocity as a function of the stopping time (see Sec. 4.1).

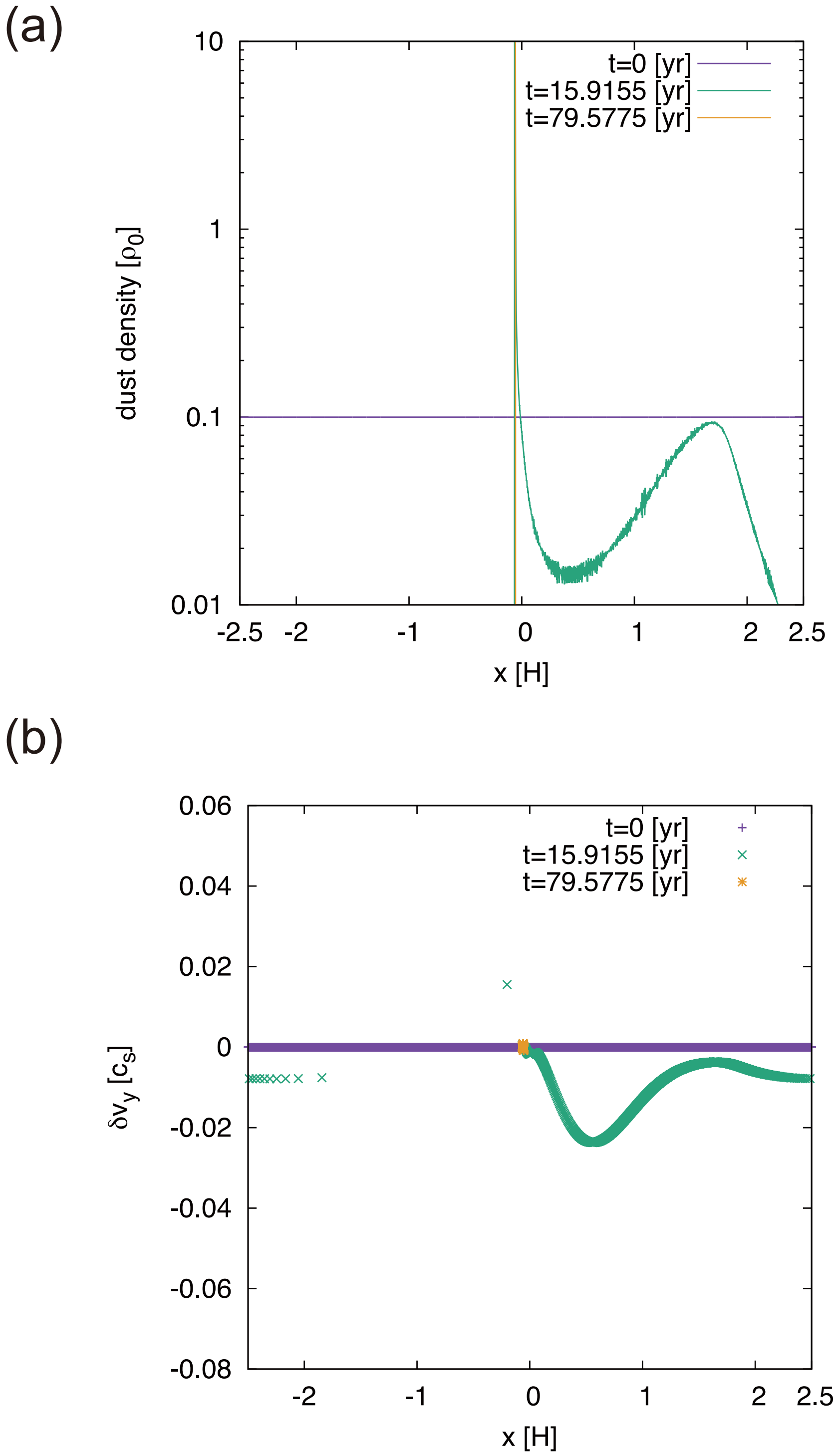

FIGURE 4.8: Same plots as Fig. 4.3 but for the case without the dust drag force. Since the pressure bump is strictly steady, the dust particles accumulate at *one* grid cell where the transition point of the super-Keplerian/sub-Keplerian flow.

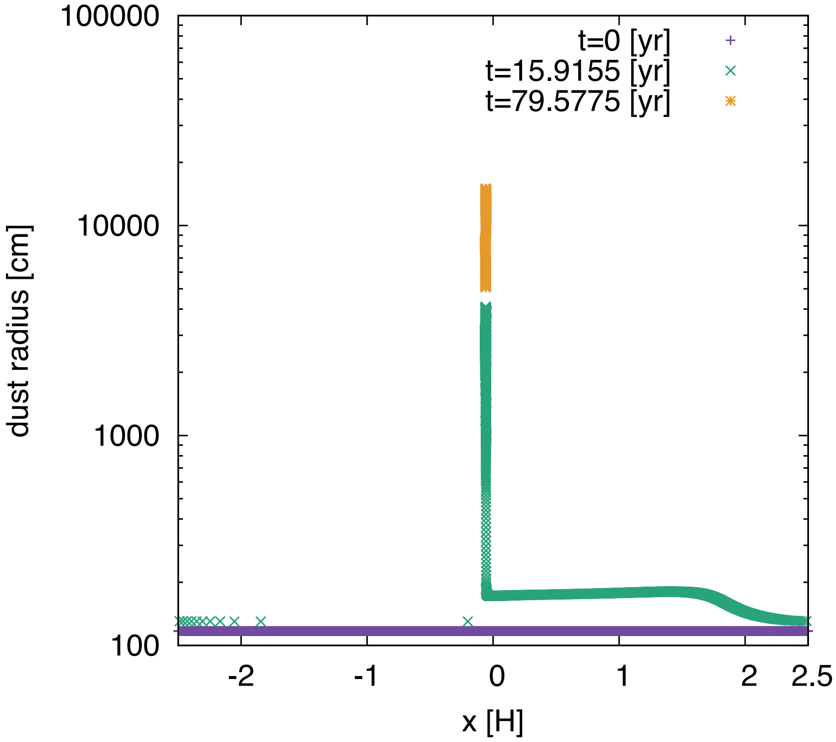

FIGURE 4.9: Same plots as Fig. 4.4 but for the case without the dust drag force. The difference in the dust radii at the dust accumulated point represent the difference in times when the dust particle achieves the point.

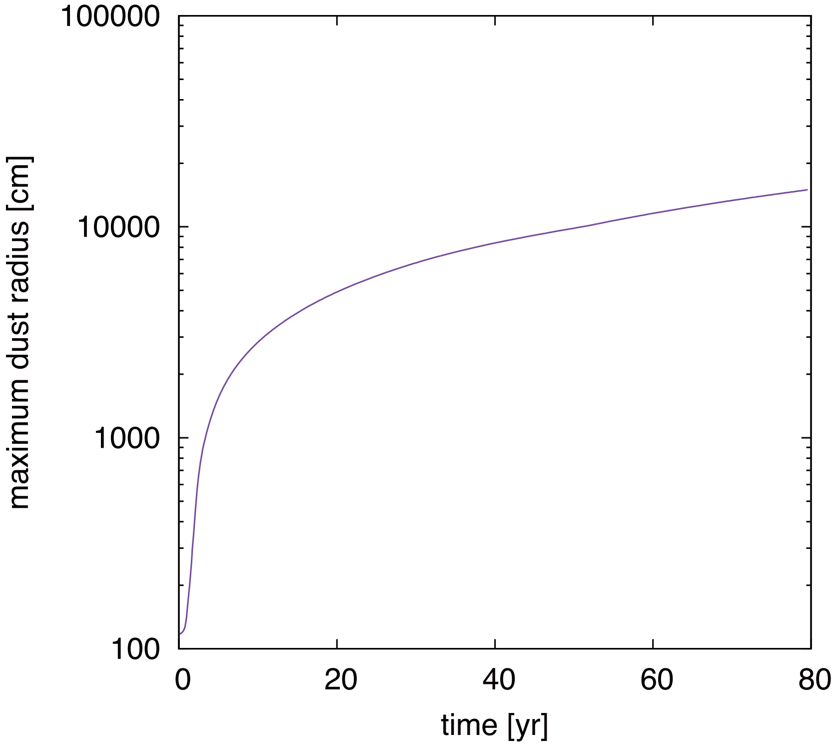

FIGURE 4.10: Same plot as Fig. 4.6 but for the case without the dust drag force.

4.2.3 Case with Small Dust Particles

The actual radius of dust particles which undergo the radial drift are smaller than the radius corresponds to $\tau_{\mathrm{s}}\Omega = 1$. The radius of rocky dust particles are determined by the fragmentation velocity (Birnstiel et al. 2012) The maximum size of dust particles is estimated as $\sim$ 1mm at $r = 1AU$ of the MMSN model (Birnstiel et al. 2012; Drazkowska and Dullemond 2014) Therefore we test the case with initial dust radius $a_{\mathrm{ini}} \equiv 1$mm which corresponds to the $\tau_{\mathrm{s}}\Omega \equiv 10^{-4}$.

The pressure bump evolution becomes slower than the fiducial case. This is because the small dust particles have the small radial drift velocity. Fig. 4.11 shows that the gas total pressure and azimuthal velocity distribution. The azimuthal velocity is the deviation from the Keplerian rotation. In this figure, we can confirm that the time evolution of the pressure bump is slower than the fiducial case. Note that the azimuthal velocity does not becomes Keplerian velocity at a part of the dust dense region.

Fig. 4.12 is the spatial distribution of the dust radius. The distribution has steeper peak near the center of the pressure bump. This is because the slower bump deformation forms the steeper dust dense region. The dust particles trapped by pressure bump at early part of the evolution grow selectively. The maximum dust radius is shown in Fig. 4.13. Because of the quick growth in early part of the evolution, the final radius is comparable to or slightly higher than the fiducial case.

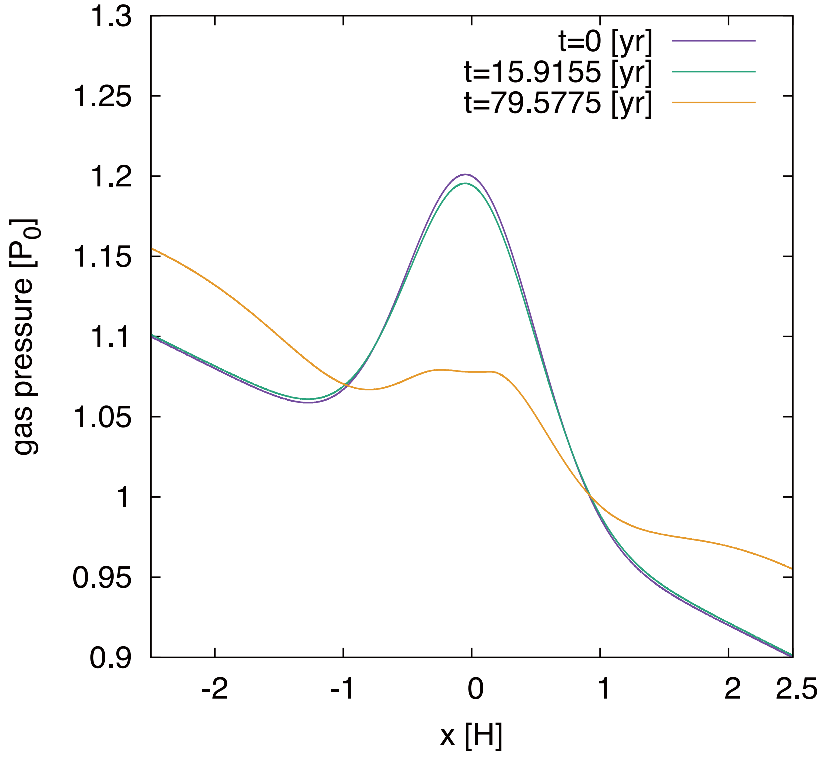

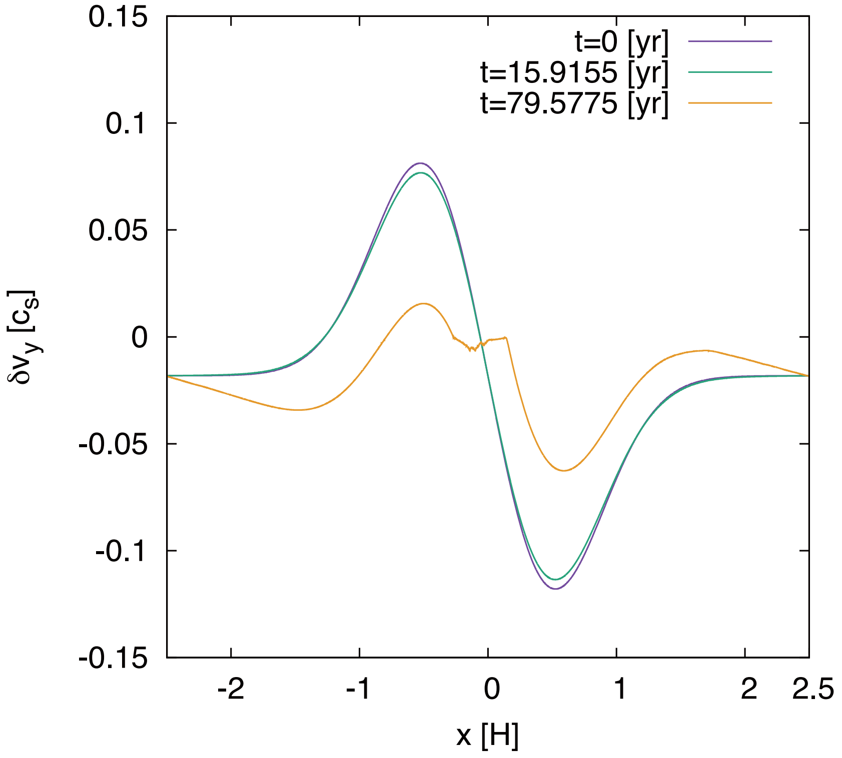

FIGURE 4.11: Same plots as Fig. 4.5 but for small dust particles at initial state, $a_{\rm ini} \sim 1$mm. Since the dust particles have small radii at initial state, the gas evolution is slower than our fiducial model.

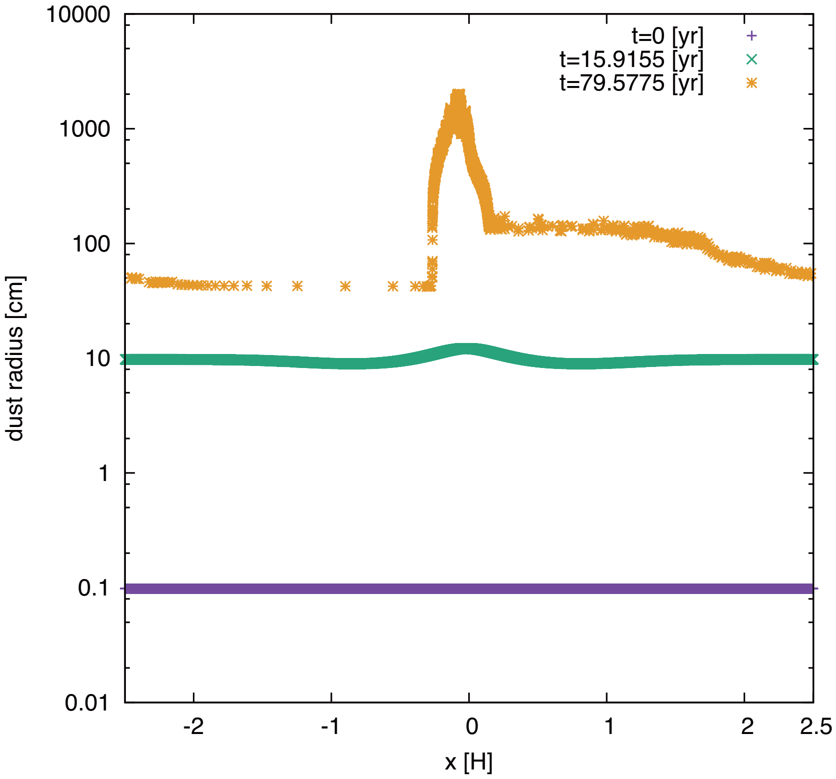

FIGURE 4.12: Same plots as Fig. 4.4 but for small dust particles at initial state, $a_{\rm ini} \sim 1$mm.

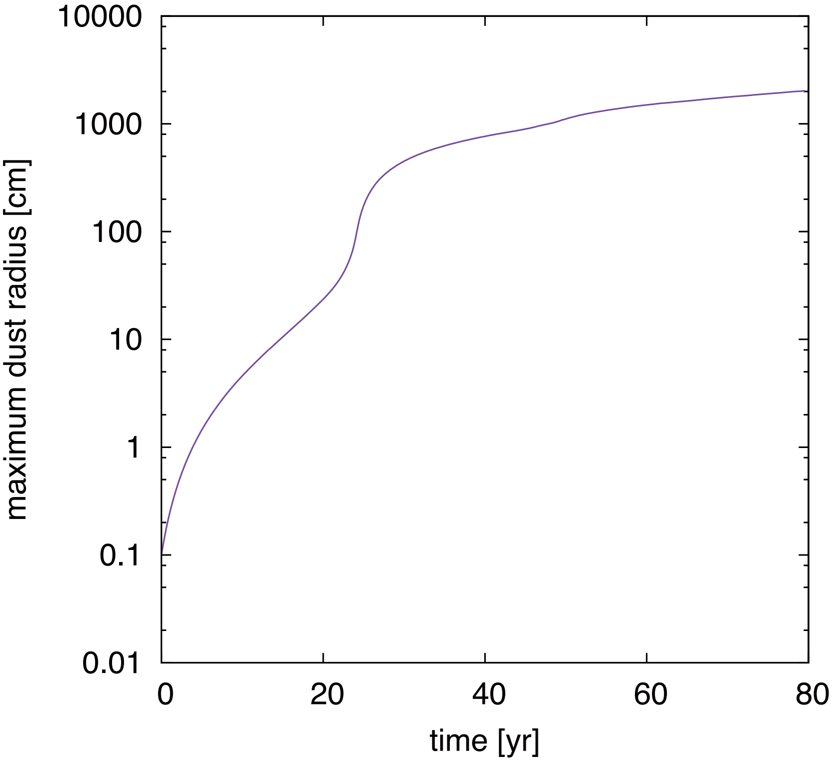

FIGURE 4.13: Same plot as Fig. 4.6 but for small dust particles at initial state, $a_{\rm ini} \sim 1$mm.

4.2.4 Case with Small Dust-to-Gas Ratio

In previous subsection, we found that the slower bump deformation might produce the quick dust growth. Another situation of slow bump deformation is the case with small dust-to-gas ratio. When the protoplanetary disk has small dust-to-gas ratio, the momentum flux brought by the dust accretion also becomes small. Then the gas density evolution becomes slow.

Fig. 4.14 shows that the spatial distribution of the gas total pressure and the gas azimuthal velocity which is deviation from the Keplerian velocity. The deformation of the pressure bump becomes slow and the dust dense region is narrower than the fiducial case. Fig. 4.15 represents the spatial distribution of the dust radius. The inner edge of the dust dense region is fixed and the particles located at the edge have the largest radius. The time evolution of the maximum dust density is shown in Fig. 4.16.

At the final state, the maximum dust radius is ~ 2 times larger than the fiducial case.

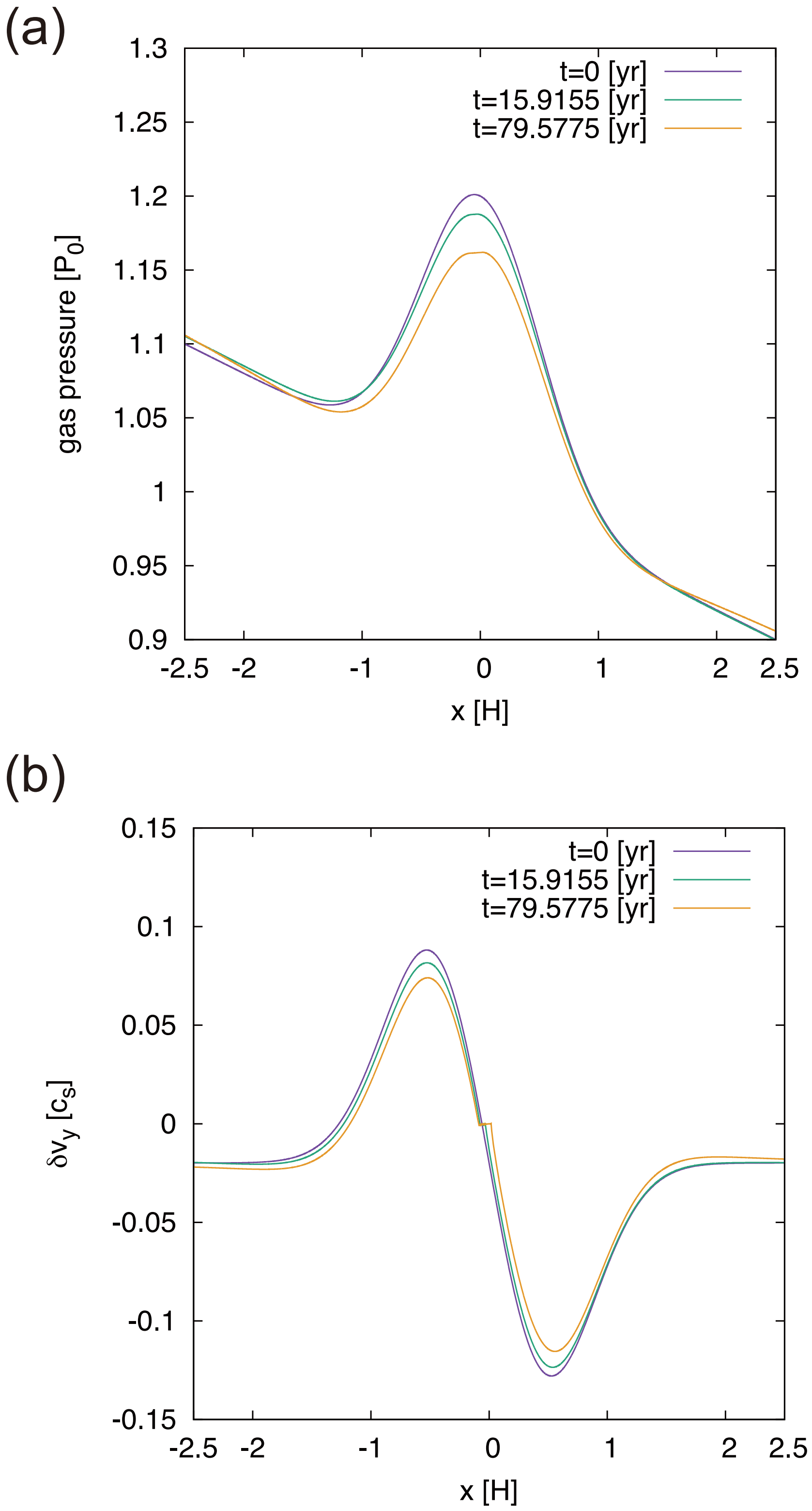

FIGURE 4.14: Same plots as Fig. 4.5 but for the case with the initial dust-to-gas mass ratio $\epsilon = 0.01$. Since the mass flux of the dust particles is smaller than the fiducial model, the evolution of the pressure bump is more slowly and the narrow dust dense region is formed.

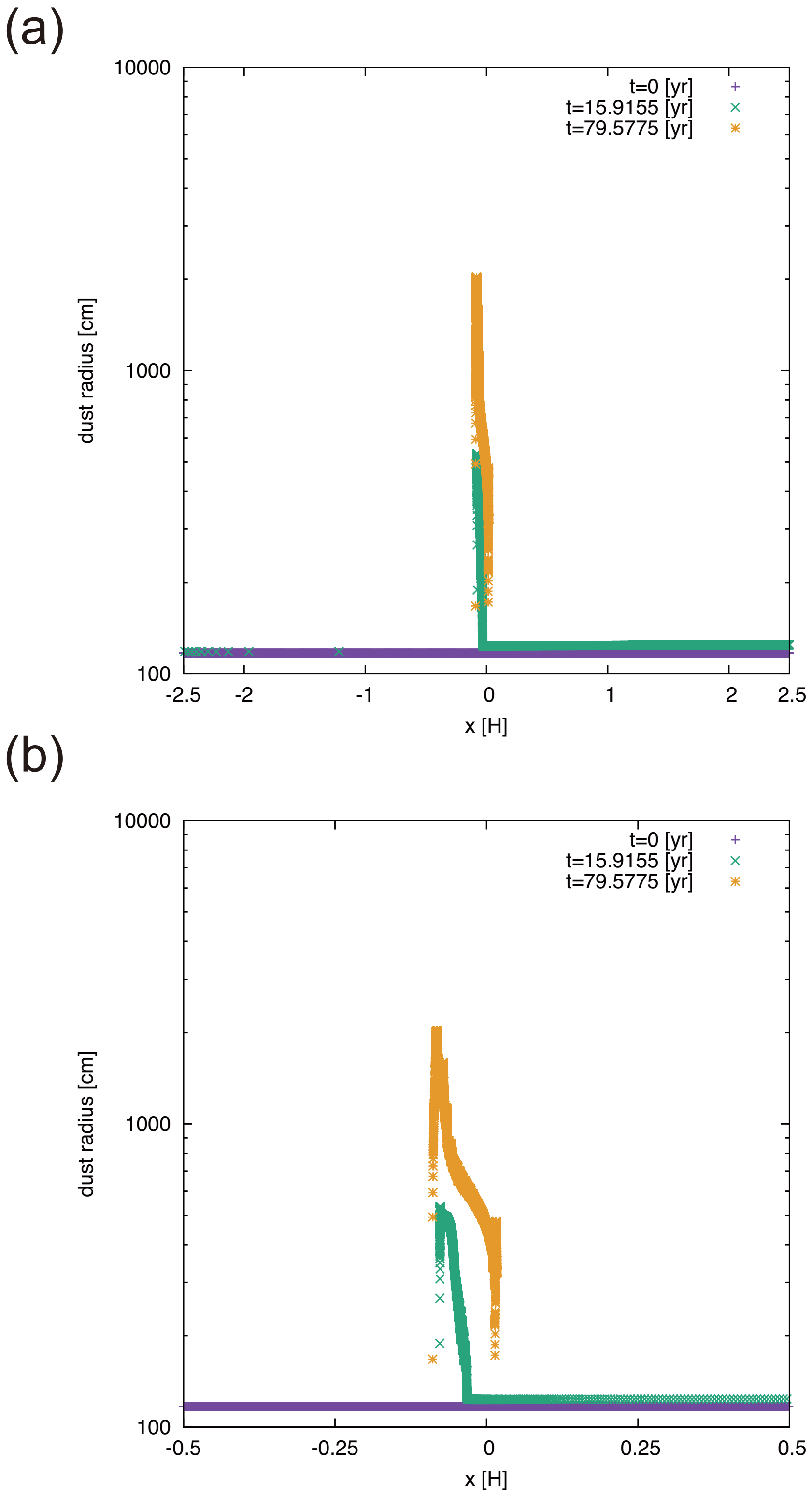

Figure 4.15: Same plots as Fig. 4.4 but for the case with the initial dust-to-gas mass ratio $\epsilon = 0.01$.

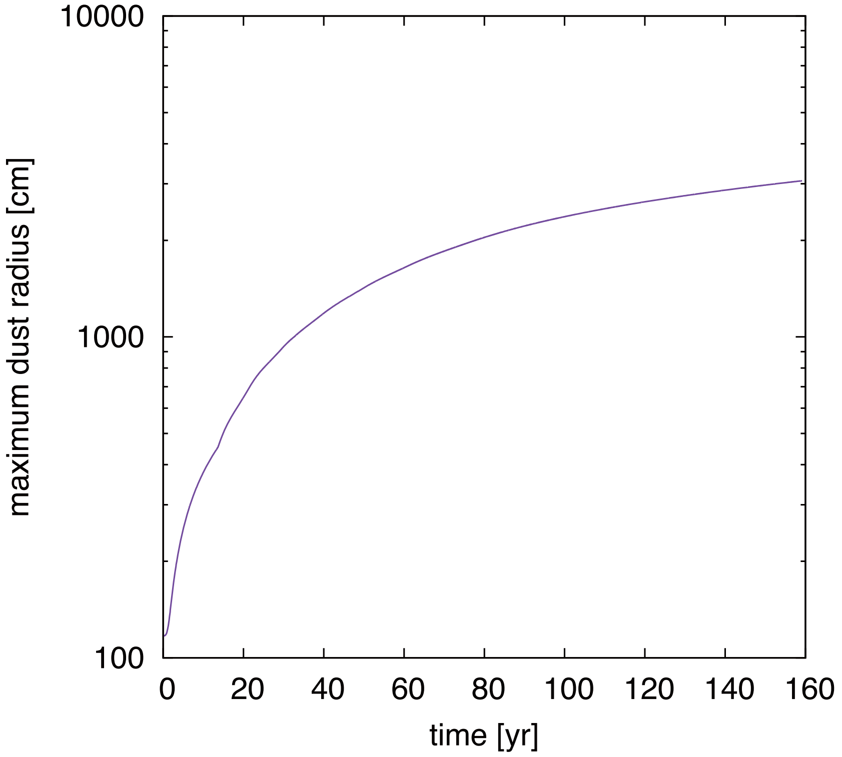

FIGURE 4.16: The same plot as Fig. 4.6 but for the case with the initial dust-to-gas mass ratio $\epsilon = 0.01$.

4.2.5 Effect of the Size of the Simulation Box

In Chap. 2, the pressure bump is completely deformed by the dust accumulation, but the pressure bump deformation is uncompleted in our fiducial run of this chapter. There may be two reasons of this. First, the grown dust particles have the large stopping time, so the angular momentum exchange becomes inefficient at the dust dense region. Second, in the fiducial model, the box size is smaller than the cases in Chap. 2, so the total angular momentum is lower than the case of Chap. 2. The continuous dust accretion may deform the pressure bump completely. Then we test the case with larger box size $L_x = 10H$ and compare with the case with no dust growth.

Fig. 4.17 is the time evolution of the maximum dust radius for run C5-05. The maximum dust radius is almost same with the fiducial case at the final state of simulations. However the gas profile evolution is significantly different from the fiducial case. Fig. 4.18 shows that the gas total pressure and the gas azimuthal velocity. Until $t \approx 80$yr, the pressure bump is completely deformed. This evolution is slightly slower than the case without dust growth. And the final state of the total pressure is relatively steeper than the Chap. 2. These are because the angular momentum exchange becomes inefficient. Fig. 4.19 shows the spatial distribution of the dust radius. We can confirm that the dust inward drift restart at the inner edge of the dust dense region. The radial drift velocity of dust particles are represented in Fig. 4.20. Since the dust dense region have the relatively large pressure gradient (but smaller than the outside of the pressure bump), the drift velocity also larger than the fiducial case. The drift velocity is $\sim$ 10cm/s to 1m/s.

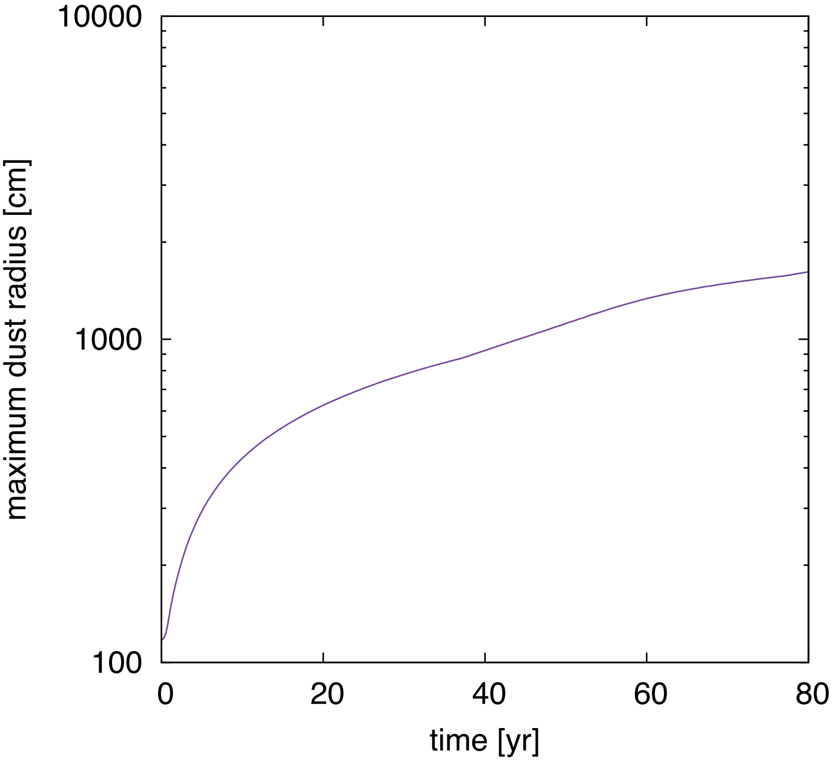

FIGURE 4.17: Same plots as Fig. 4.6 but for $L_x = 10H$. At $t \sim 40$ yr, the super-Keplerian region is completely flattened.

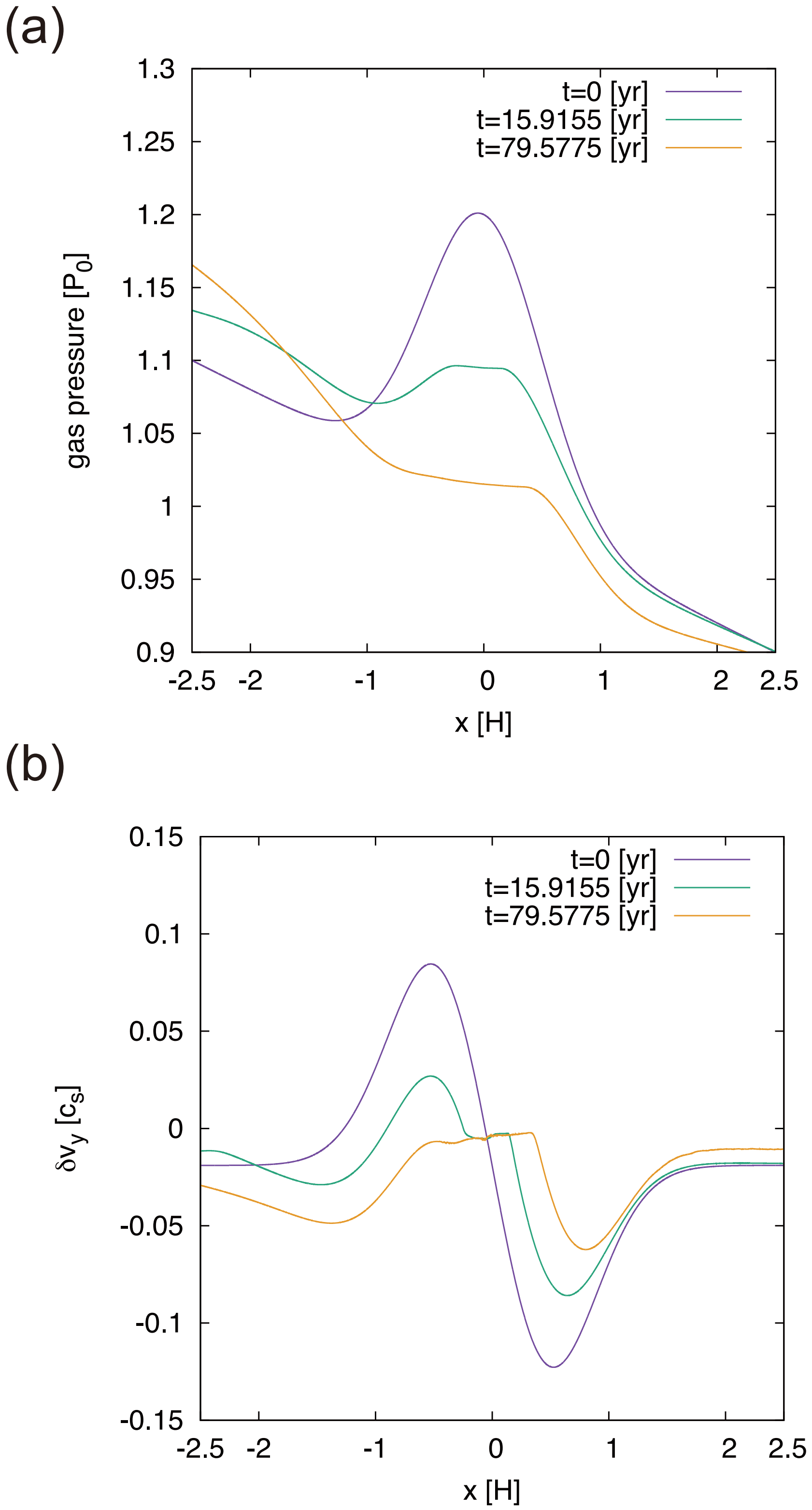

FIGURE 4.18: Same plots as Fig. 4.5 but for $L_x = 10H$. Panel (b) shows that the super-Keplerian region is completely flattened due to the dust accretion from the outer part of the disk.

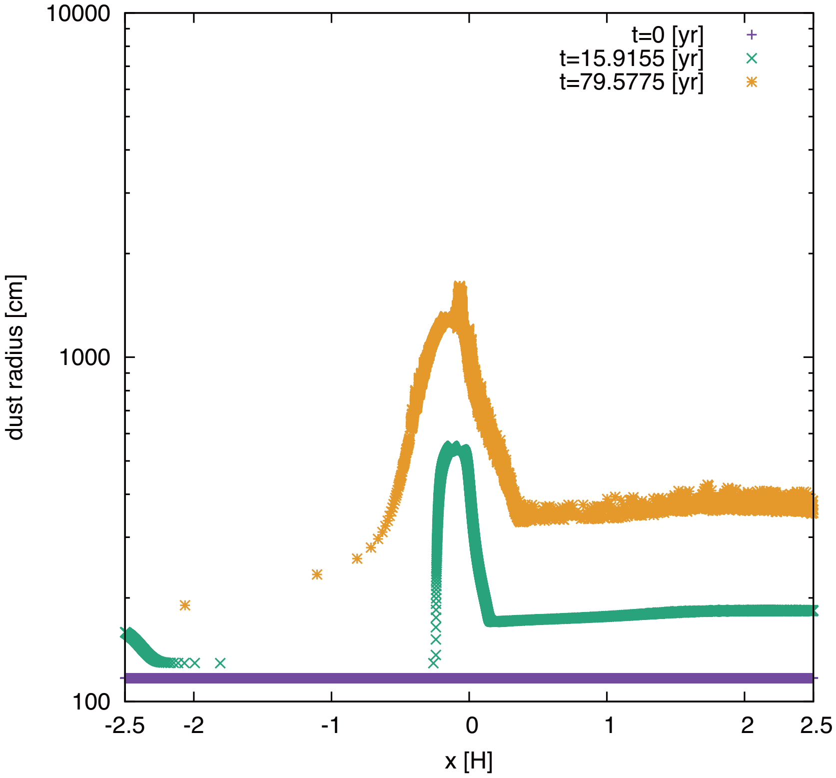

FIGURE 4.19: Same plots as Fig. 4.4 but for $L_x = 10H$. At $r \sim 80$ yr, since the super-Keplerian region had been broken, the relatively small dust particles restart the inward migration from the inner edge of the dust dense region.

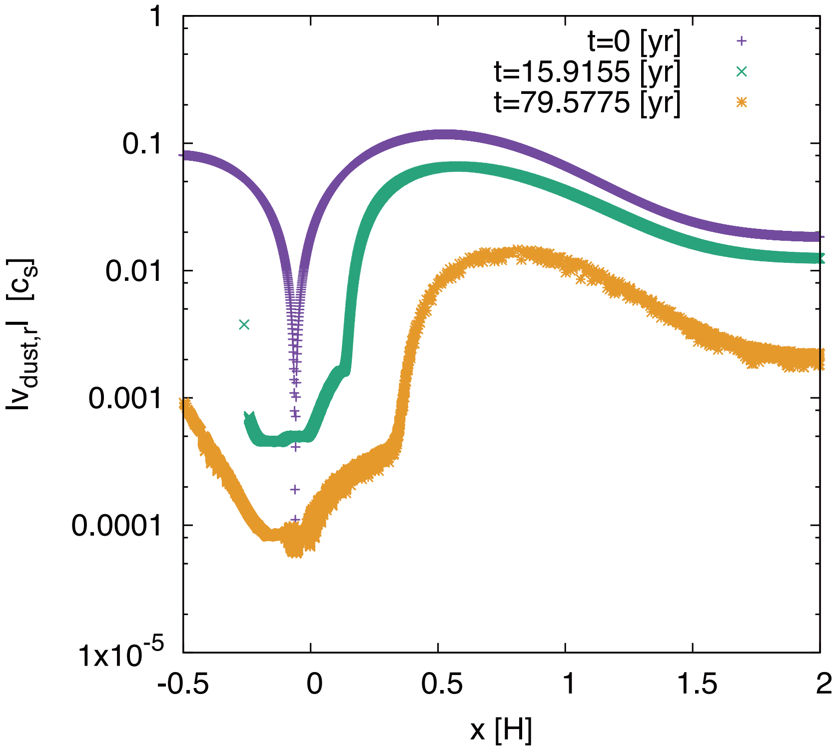

FIGURE 4.20: Same plots as Fig. 4.7 but for $L_x = 10H$. Since the continuous dust accretion drives outward flow of the gas, the radial velocities are few times larger than the fiducial model.

4.3 Discussion

4.3.1 Comparison of Components of Relative Velocities

At the dust dense region, it seems that the powers of the maximum dust radius are same in all cases. To understand this feature, we compare the component of the relative velocity between dust particles in Fig. 4.21. The red line of Fig. 4.21 represents the relative velocity due to the turbulence which is defined as Eq. (4.10). Other two lines are the dust radial drift velocity obtained by Nakagawa et al. (1986) for the case with $\epsilon_0 = 0.01, 0.1$, respectively. At the large Stokes number, the turbulent relative velocity is proportional to $\mathrm{St}^{-1/2}$, while the NSH equilibrium solutions are proportional to St^{-1} Hence the turbulent relative velocity is larger than the radial drift velocity at large Stokes number. In addition, after the dust density is saturated, the dust dense region has the small pressure gradient. Therefore the dust particles have the small radial drift velocity, and the relative velocity between dust particles are dominated by the turbulence.

After the maximum dust density is saturated, the coagulation equation under the constant dust density is only depends on the relative velocity. The dust relative velocity is dominated by the turbulent relative velocity which is the function of the stopping time. The stopping time is expressed by the Eq. (4.8). Then the coagulation equation can be solved analytically and we obtain the constant growth rate.

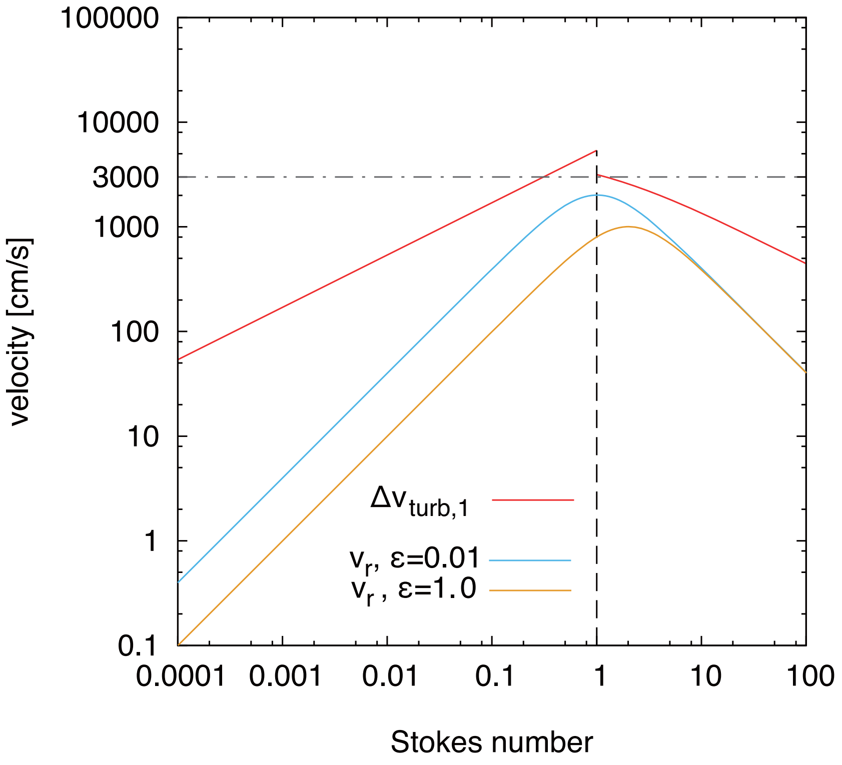

FIGURE 4.21: Comparison between the turbulent relative velocity and radial drift velocity of dust particles as a function of the Stokes number. The red line represents the dust relative velocity due to the turbulent stirring described by eq. (4.10), which switches at $\tau_s = 1.0$. The cyan, yellow lines represent the dust radial drift velocity derived by Nakagawa et al. (1986) in the case with dust-to-gas ratio $\epsilon = 0.01,\ 1.0$.

4.3.2 Case with the Supplemental Large Particles

When the evolution of the pressure bump is inefficient, we suggest that the trapped particles undergo the selectively growth. The inefficient bump deformation forms the narrow dust dense region. The steep gradient of dust density and dust radius may accelerate the dust growth.

To test this hypothesis, we conduct the run C5-06. In this run, the parameters are same with the fiducial run except that the stopping time $\tau_{\mathrm{s}}\Omega \sim 10^{-3}$ and there are small number of additional particles which have the large stopping time $\tau_{\mathrm{s}}\Omega \sim 1.0$. Fig. 4.23 shows that the spatial distribution of the dust radius. Initially large particles are quickly accumulated into the pressure maximum and grown selectively. Fig. 4.24 is the time evolution of the maximum dust radius. At the final state, the maximum dust density is slightly higher than other cases. If we include the turbulent diffusion, the small particles are prevented the accumulation. So the growth of large particles may become more quick and the bump deformation become more inefficient.

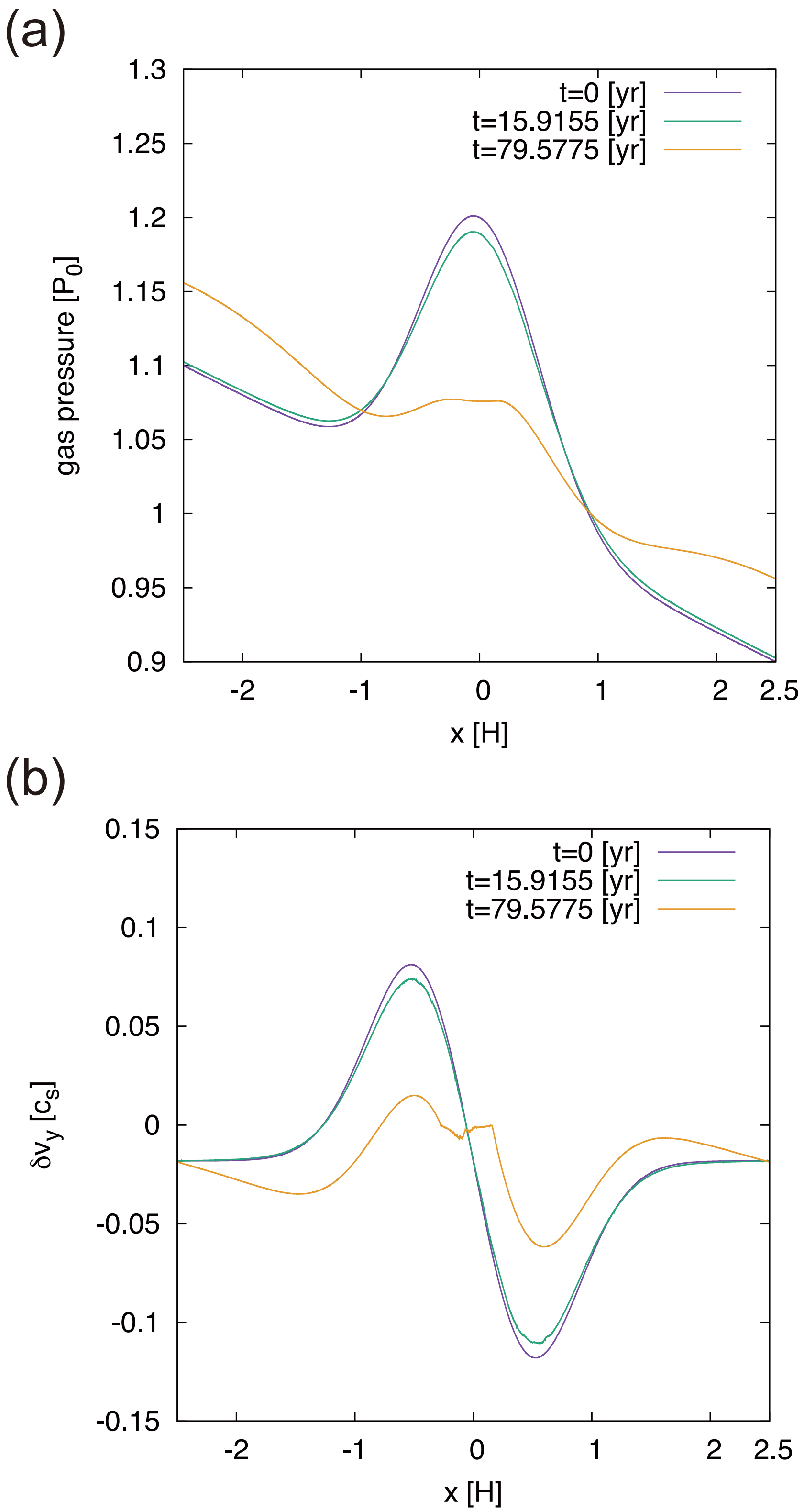

FIGURE 4.22: Same plots as Fig. 4.5 but for run –. Most particles have the small radii, the gas evolution is similar to Fig. 4.11.

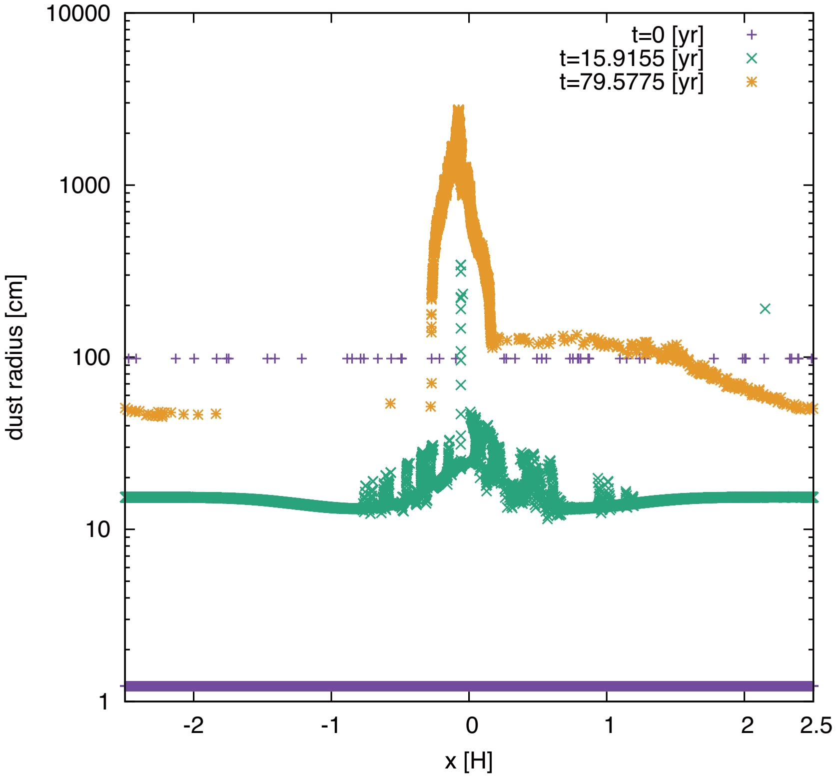

Figure 4.23: Same plots as Fig. 4.4 but for run –. The initially larger dust particles have larger drift velocity and accumulate faster than small particles.

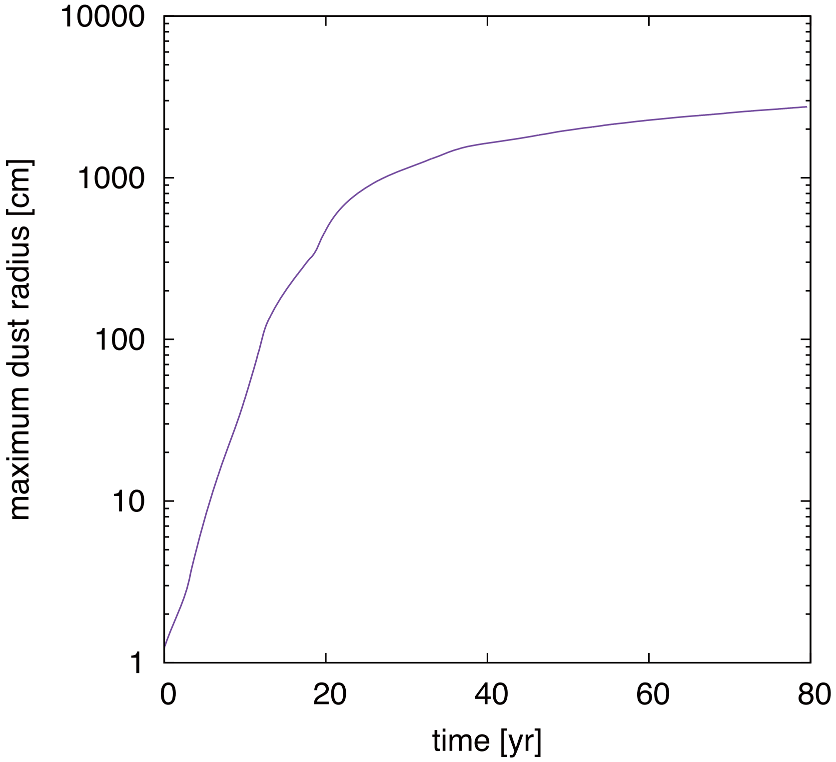

FIGURE 4.24: Same plots as Fig. 4.6 but for run –. Because of the quick accumulation of large dust particles, the maximum radius is several times larger than the result of our fiducial model.

4.3.3 Estimation of the Crossing Time vs Growth Time

In our simulations, the large particles have small radial velocity at dust dense region, so we cannot continue the simulation until the dust particles across the pressure bump. In this subsection, we estimate the bump crossing time and the growth time of the dust particles. The bump crossing time is the time required to pass through the pressure bump by typical size dust particles. The growth time is the mass doubling timescale of dust particles due to the direct sticking.

The bump crossing time is estimated as $t_{\rm cross} = H_{\rm bump}/u_r$, where $H_{\rm bump}$ is the radial width of the dust dense region and u_r is the dust radial velocity, respectively. The radial drift velocity at the dust dense region is $\sim 10^{-4} c_s$ (for fiducial case) or $\sim 10^{-3} c_s$ (for run C5-05) (see Fig. 4.7, 4.20). We assume that the radial width of the dust dense region is $\sim 0.5H$. Then we obtain the bump crossing time as

$$t_{\text{cross}}\Omega = \frac{H_{\text{bump}}}{u_r} \sim \{500 - 5000\}\,. \tag{4.18}$$

The growth time of the dust particle is estimated as

$$t_{\text{grow}}\Omega = \frac{4\sqrt{2\pi}}{3}\frac{h_d}{\Delta v}\frac{\rho_{\text{int}}a}{\Sigma_d}\Omega. \tag{4.19}$$

For the Stokes regime,

$$\rho_{\text{int}}a = \frac{\text{St}}{\Omega}\cdot\frac{9\lambda_{\text{mfp}}}{4a}\rho_g v_{\text{th}}. \tag{4.20}$$

And the turbulent relative velocity is $\sim \sqrt{\alpha/(\tau_{\text{s}}\Omega)}c_s$. Then we obtain the growth timescale as

$$t_{\text{grow}}\Omega \sim 3\sqrt{\frac{8}{\pi}}\cdot \text{St}^{3/2}\left(\frac{\rho_d}{\rho_g}\right)^{-1}\alpha^{-1/2}\,\frac{\lambda_{\text{mfp}}}{a}. \tag{4.21}$$

We assume the parameters as $\alpha = 10^{-3}, \rho_d/\rho_g = 1, \tau_{\text{s}}\Omega = 100, a = 1000\text{cm}$, and $\lambda_{\text{mfp}} = 1\text{cm}$, respectively. These values are taken from our simulations or MMSN model. Finally, the growth time is

$$t_{\text{grow}}\Omega \sim 10. \tag{4.22}$$

Then the ration of these two timescales is

$$\frac{t_{\text{grow}}}{t_{\text{cross}}} \sim \frac{1}{50} - \frac{1}{500}. \tag{4.23}$$

Therefore the dust particles can grow larger and larger surprisingly.

Chapter 5

Discussion

We set the radial pressure bump as the initial condition of our calculations. The various formation mechanisms of the pressure bump have been proposed (e.g. MRI zonal flows, edges of the MRI dead zone, a snow line, etc.). These mechanisms and the global disk evolution affect the bump deformation process. If the bump restoration/restructuring process is faster than the destruction process we discussed here, the radial pressure bump could accumulate more dust particles.

Dust self-gravity and vertical gravity of the host star are other important physical elements neglected in this study. Bai and Stone (2010) and Johansen et al. (2012) included these physical elements, and confirmed that gravitationally bound clumps are formed by SI at the midplane of dust layer. These physical elements may be also driven at pressure bumps.

Our calculations do not take into account Kelvin-Helmholtz Instability (KHI) by radial shear in azimuthal velocity and vertical shear in radial/azimuthal velocity. Johansen and Youdin (2007) and Bai and Stone (2010) found that SI is dominant over the KHIs. In general, small-scale instability can be damped by other perturbations. It is not clear if SI is ever dominant at the dust dense region. At the radial boundary of the dust dense region, there may be a larger shear than the Keplerian shear to cause strong KHI. So the actual property of the turbulence at the pressure bump is unclear. The investigation on the effect of KHI is left for future work.

This thesis is the first study of the dust growth with coupling to the dust and gas dynamics at the local structure of the protoplanetary disk. To investigate the basic property of the dust and gas evolution, the dust coagulation model is simplified, i.e., we assume the perfect sticking and compact growth. In an actual protoplanetary disk, the maximum size of rocky particles may be determined by the fragmentation velocity. Indeed the relative velocity induced in our simulations is larger than the critical fragmentation velocity. So the particles flow into the pressure bump have much smaller radius. However, we partly confirmed this effect. In run C5-03, the initial dust particles set as mm-sized body. When the dust particles arrive at the pressure bump, the dust particles have been grown but these sizes are the comparable to the maximum size determined by the relatively slack fragmentation velocity $\sim$ 10m/s.

In Chap. 4, we assume the turbulent relative velocity to be constant. Indeed, one of the possible energy source of protoplanetary disk turbulence is to release gravitational energy induced by the accretion of dust layer (Takeuchi et al. 2012). At the dust dense region formed by the pressure bump, radial velocity of dust layer is significantly smaller than that in nominal MMSN model. Therefore the turbulence in such regions tends to be weak. To consider the fragmentation of dust particles, this dependency of turbulent strength on the radial pressure support may play an important role.

Since the radial pressure gradient is small, the relative velocity of dust particles is also small at the dust dense region. Therefore the growth of dust particles becomes slower and is limited by the turbulent relative velocity. The growth time of dust particles is estimated in Sec. 4.3.3. If the dust dense region is destroyed by the disk evolution or other perturbations faster than dust growth, all dust particles which had been trapped at the pressure bump restart the inward migration. This inward migration may be favorable for dust growth. As seen in Sec. 4.2, at the dust dense region, dust particles quickly pass the size corresponding to St = 1 due to collisional growth. And the gas drag law also quickly changes into Stokes law. Under these conditions, the ratio of growth and drift timescale of dust particles $\tau_{\rm grow}/\tau_{\rm drift} \propto a^{-1}$. And these large bodies do not exceed the critical fragmentation velocity any more even for the rocky grains. Therefore dust particles undergo the runaway growth and grow into planetesimals even if the internal density evolution is not considered. In this context, the radial pressure bump does not form the planetesimals directly, but prepares the condition for the planetesimal formation.

Chapter 6

Summary

We numerically studied the dust and gas density evolution at a radial pressure bump in a protoplanetary disk. Disk gas dynamics is treated with grid hydrodynamics and dust components are treated with the particle-in-cell scheme. The gas drag force and its back-reaction are included in our simulations self-consistently. Computational regions are approximated by the local shearing-box model.

In Chap. 2, we unveil the general mechanism of the bump deformation process. We also investigate the property of the streaming instability at the dust dense region formed by the radial pressure bump. The overview of the dust and gas density evolution at the radial pressure bump as follows:

- The pressure bump accumulated dust particle, but gas outward flow created by back-reaction from the accumulated particles onto gas smooths out the bump when a dust-to-gas mass ration achieves ~ 1, if the bump restoration/restructuring is slower than the destruction process.
- The pressure bump creates a long-lived dust dense region where the vertically averaged dust-to-gas mass ratio is ~ 1. When dust inward drift continues to accumulate dust particles at the outer-edge of the pressure bump, the flattened part of the pressure profile in the dust dense region expands outward until the pressure bump is completely destroyed.

- As a result of the bump destruction, direct self-gravitational instability at the pressure bump is inhibited.
- The gas flow in pressure bumps is modulated to be close to the Keplerian one and the deviation from Keplerian velocity (η) is $\sim 10-100$ times smaller than the global value. Because the SI wavelength is scaled by η, the clumps formed by SI, even if the SI occurs, should be much smaller than the previously proposed size ($\sim 100-1000$ km).

We predict that streaming instability, if it occurs, forms *classic* planetesimals at the radial pressure bump.

In Chap. 3, we investigate the effect of the vertical inhomogeneity of the dust layer on the evolution of the pressure bump. We found that the vertical compression process of the dust dense region formed by the radial pressure bump. The accumulation of the thin dust layer located near the midplane naturally induces the vortices like structure of gas flow. This vortices like flow pattern of gas compresses the dust layer in vertical direction. The peak value of dust density attained by the vertical compression is $\sim 50\rho_0$, which is significantly higher than the case with vertically uniform dust density as shown in Chap. 2 In addition, the gas azimuthal velocity is completely uniform in vertical direction. It means that there are no vertical shear of the azimuthal velocity which might drive the Kelvin-Helmholtz instability when the further sedimentation occurs. This high density region is temporal feature in our simulations which neglect the vertical gravity of the host star. The effect of vertical gravity may be important to keep the high density of dust layer. Besides the transient high density may affect the dust growth well.

In Chap. 4, we include the effect of dust growth in the calculation of dust and gas dynamics. We develop the new simulation code including the dust coagulation process which is approximated as “single size approach”. We found that the pressure bump also forms the dust dense region in the same manner as Chap. 2. The dust dense region formed by the pressure bump encourages the dust coagulation due to the high dust-to-gas mass ratio. Dust particles quickly grow into 10 meter-sized bodies in our simulations. We estimate the ratio of growth and crossing timescale at the dust dense region as $t_{\mathrm{grow}}/t_{\mathrm{cross}} \sim 1/50-1/500$. If dust dense region does not destroyed by global disk evolution, dust particles can grow into planetesimals at there. In this case, the local planetesimal ring may be formed at the pressure bump. On the other hand, even when the pressure bump is vanished by the disk evolution or other perturbations earlier than the planetesimal formation, the pressure bump may prepare the condition for the planetesimal formation due to the runaway growth of particles having $\mathrm{St} \gg 1$ during the radial drift.

In this thesis, we renew the established prediction of planetesimal formation at the radial pressure bump. We find that the pressure bump deformation plays an important role in planetesimal formation theory. Direct self-gravitational instability at the pressure bump is inhibited by the bump destruction, and the large scale streaming instability observed in previous studies are also damped due to the small pressure gradient. On the other hand, the small pressure gradient allows a dust dense region to drive the small scale streaming instability which may form dense particle clumps corresponding to km-sized bodies. In addition, if streaming instability does not occur, the dust dense region encourages the dust growth due to the relatively high dust density and the small drift velocity of dust particles. We emphasize that the pressure bump is a favorable place for planetesimal formation in a different manner from previous studies.

Bibliography

Adachi, I., Hayashi, C., and Nakazawa, K. (1976). The Gas Drag Effect on the Elliptic Motion of a Solid Body in the Primordial Solar Nebula. *Prog. Theor. Phys.*, 56(6):1756–1771.

Bai, X.-N. and Stone, J. M. (2010). DYNAMICS OF SOLIDS IN THE MIDPLANE OF PROTOPLANETARY DISKS: IMPLICATIONS FOR PLANETESIMAL FORMATION. *Astrophys. J.*, 722(2):1437–1459.

Balbus, S. a. and Hawley, J. F. (1992). A Powerful Local Shear Instability in Weakly Magnetized Disks. IV. Nonaxisymmetric Perturbations. *Astrophys. J.*, 400:610.

Barge, P. and Sommeria, J. (1995). DID PLANET FORMATION BEGIN INSIDE PERSISTENT GASEOUS VORTICES? *Astron. Astrophys.*, 295(1):L1———L4.

Birnstiel, T., Klahr, H., and Ercolano, B. (2012). A simple model for the evolution of the dust population in protoplanetary disks. *Astron. Astrophys.*, 539:A148.

Blum, J. and Wurm, G. (2008). The Growth Mechanisms of Macroscopic Bodies in Protoplanetary Disks. *Annu. Rev. Astron. Astrophys.*, 46(1):21–56.

Brauer, F., Dullemond, C. P., and Henning, T. (2008a). Coagulation, fragmentation and radial motion of solid particles in protoplanetary disks. *Astron. Astrophys.*, 480(3):859–877.

Brauer, F., Henning, T., and Dullemond, C. P. (2008b). Planetesimal formation around the snow line in MRI-driven turbulent protoplanetary disks. *Astron. Astrophys.*, 4(1):1–4.

Carballido, A., Fromang, S., and Papaloizou, J. (2006). Mid-plane sedimentation of large solid bodies in turbulent protoplanetary discs. *Mon. Not. R. Astron. Soc.*, 373(4):1633–1640.

Casassus, S., van der Plas, G., M, S. P., Dent, W. R. F., Fomalont, E., Hagelberg, J., Hales, A., Jordán, A., Mawet, D., Ménard, F., Wootten, A., Wilner, D., Hughes, A. M., Schreiber, M. R., Girard, J. H., Ercolano, B., Canovas, H., Román, P. E., and Salinas, V. (2013). Flows of gas through a protoplanetary gap. *Nature*, 493(7431):191–194.

Dittrich, K., Klahr, H., and Johansen, A. (2013). GRAVOTURBULENT PLANETESIMAL FORMATION: THE POSITIVE EFFECT OF LONG-LIVED ZONAL FLOWS. *Astrophys. J.*, 763(2):117.

Drazkowska, J. and Dullemond, C. P. (2014). Can dust coagulation trigger streaming instability? *Astron. Astrophys.*, 572:A78.

Drazkowska, J., Windmark, F., and Dullemond, C. P. (2013). Planetesimal formation via sweep-up growth at the inner edge of dead zones. *Astron. Astrophys.*, 556:A37.

Dubrulle, B. (1995). The Dust Subdisk in the Protoplanetary Nebula. *Icarus*, 114(2):237–246.

Fromang, S. and Nelson, R. P. (2005). On the accumulation of solid bodies in global turbulent protoplanetary disc models. *Mon. Not. R. Astron. Soc. Lett.*, 364(1):L81–L85.

Guillot, T., Ida, S., and Ormel, C. W. (2014). On the filtering and processing of dust by planetesimals. *Astron. Astrophys.*, 572:A72.

Guttler, C., Blum, J., Zsom, A., Ormel, C. W., and Dullemond, C. P. (2010). The outcome of protoplanetary dust growth: pebbles, boulders, or planetesimals? *Astron. Astrophys.*, 513:A56.

Haghighipour, N. and Boss, A. P. (2003a). On Gas Drag–Induced Rapid Migration of Solids in a Nonuniform Solar Nebula. *Astrophys. J.*, 598(2):1301–1311.

Haghighipour, N. and Boss, A. P. (2003b). On Pressure Gradients and Rapid Migration of Solids in a Nonuniform Solar Nebula. *Astrophys. J.*, 583(2):996–1003.

Hawley, J. F., Gammie, C. F., and Balbus, S. a. (1995). Local Three-dimensional Magnetohydrodynamic Simulations of Accretion Disks. *Astrophys. J.*, 440:742.

Hayashi, C., Nakazawa, K., and Nakagawa, Y. (1985). Formation of the solar system. *Protostars planets II (A86-12626 03-90). Tucson*, pages 1100–1153.

Jacquet, E., Balbus, S., and Latter, H. (2011). On linear dust-gas streaming instabilities in protoplanetary discs. *Mon. Not. R. Astron. Soc.*, 415(4):3591–3598.

Johansen, A., Blum, J., Tanaka, H., Ormel, C., Bizzarro, M., and Rickman, H. (2014). The Multifaceted Planetesimal Formation Process. In *Protostars Planets VI*. University of Arizona Press.

Johansen, A. and Klahr, H. (2011). Planetesimal Formation Through Streaming and Gravitational Instabilities. *Earth. Moon. Planets*, 108(1):39–43.

Johansen, A. and Youdin, A. (2007). Protoplanetary Disk Turbulence Driven by the Streaming Instability: Nonlinear Saturation and Particle Concentration. *Astrophys. J.*, 662(1):627–641.

Johansen, A., Youdin, A., and Klahr, H. (2009a). ZONAL FLOWS AND LONG-LIVED AXISYMMETRIC PRESSURE BUMPS IN MAGNETOROTATIONAL TURBULENCE. *Astrophys. J.*, 697(2):1269–1289.

Johansen, A., Youdin, A., and Mac Low, M.-M. (2009b). PARTICLE CLUMPING AND PLANETESIMAL FORMATION DEPEND STRONGLY ON METALLICITY. *Astrophys. J.*, 704(2):L75–L79.

Johansen, A., Youdin, A. N., and Lithwick, Y. (2012). Adding particle collisions to the formation of asteroids and Kuiper belt objects via streaming instabilities. *Astron. Astrophys.*, 537:A125.

Kataoka, A., Tanaka, H., Okuzumi, S., and Wada, K. (2013a). Fluffy dust forms icy planetesimals by static compression. *Astron. Astrophys.*, 557:L4.

Kataoka, A., Tanaka, H., Okuzumi, S., and Wada, K. (2013b). Static compression of porous dust aggregates. *Astron. Astrophys.*, 554:A4.

Kato, M. T., Fujimoto, M., and Ida, S. (2010). DUST CONCENTRATION AT THE BOUNDARY BETWEEN STEADY SUPER/SUB-KEPLERIAN FLOW CREATED BY INHOMOGENEOUS GROWTH OF MAGNETO-ROTATIONAL INSTABILITY. *Astrophys. J.*, 714(2):1155–1169.

Kato, M. T., Fujimoto, M., and Ida, S. (2012). PLANETESIMAL FORMATION AT THE BOUNDARY BETWEEN STEADY SUPER/SUB-KEPLERIAN FLOW CREATED BY INHOMOGENEOUS GROWTH OF MAGNETOROTATIONAL INSTABILITY. *Astrophys. J.*, 747(1):11.

Kato, M. T., Nakamura, K., Tandokoro, R., Fujimoto, M., and Ida, S. (2009). MODIFICATION OF ANGULAR VELOCITY BY INHOMOGENEOUS MAGNETOROTATIONAL INSTABILITY GROWTH IN PROTOPLANETARY DISKS. *Astrophys. J.*, 691(2):1697–1706.

Kelling, T., Wurm, G., and Köster, M. (2014). EXPERIMENTAL STUDY ON BOUNCING BARRIERS IN PROTOPLANETARY DISKS. *Astrophys. J.*, 783(2):111.

Klahr, H. H. and Bodenheimer, P. (2003). Turbulence in Accretion Disks: Vorticity Generation and Angular Momentum Transport via the Global Baroclinic Instability. *Astrophys. J.*, 582(2):869–892.

Kretke, K. A. and Lin, D. N. C. (2007). Grain Retention and Formation of Planetesimals near the Snow Line in MRI-driven Turbulent Protoplanetary Disks. *Astrophys. J.*, 664(1):L55–L58.

Lesur, G. and Papaloizou, J. C. B. (2010). The subcritical baroclinic instability in local accretion disc models. *Astron. Astrophys.*, 513:A60.

Li, H., Colgate, S. A., Wendroff, B., and Liska, R. (2001). Rossby Wave Instability of Thin Accretion Disks. III. Nonlinear Simulations. *Astrophys. J.*, 551(2):874–896.

Li, H., Finn, J. M., Lovelace, R. V. E., and Colgate, S. A. (2000). Rossby Wave Instability of Thin Accretion Disks. II. Detailed Linear Theory. *Astrophys. J.*, 533(2):1023–1034.

Lovelace, R. V. E., Li, H., Colgate, S. a., and Nelson, A. F. (1999). Rossby Wave Instability of Keplerian Accretion Disks. *Astrophys. J.*, 513:805–810.

Lyra, W., Johansen, A., Klahr, H., and Piskunov, N. (2008a). Global magnetohydrodynamical models of turbulence in protoplanetary disks. *Astron. Astrophys.*, 479(3):883–901.

Lyra, W., Johansen, A., Klahr, H., and Piskunov, N. (2008b). Standing on the shoulders of giants: Trojan Earths and vortex trapping in low mass self-gravitating protoplanetary disks of gas and solids. *Astron. Astrophys.*, 493(3):1125–1139.

Lyra, W. and Klahr, H. (2011). The baroclinic instability in the context of layered accretion. *Astron. Astrophys.*, 527:A138.

Meru, F., Geretshauser, R. J., Schafer, C., Speith, R., and Kley, W. (2013). Growth and fragmentation of centimetre-sized dust aggregates: the dependence on aggregate size and porosity. *Mon. Not. R. Astron. Soc.*, 435(3):2371–2390.

Nakagawa, Y., Nakazawa, K., and Hayashi, C. (1981). Growth and sedimentation of dust grains in the primordial solar nebula. *Icarus*, 45(3):517–528.

Nakagawa, Y., Sekiya, M., and Hayashi, C. (1986). Settling and growth of dust particles in a laminar phase of a low-mass solar nebula. *Icarus*, 67(3):375–390.

Okuzumi, S., Tanaka, H., Kobayashi, H., and Wada, K. (2012). RAPID COAGULATION OF POROUS DUST AGGREGATES OUTSIDE THE SNOW LINE: A PATHWAY TO SUCCESSFUL ICY PLANETESIMAL FORMATION. *Astrophys. J.*, 752(2):106.

Ormel, C. W. and Cuzzi, J. N. (2007). Closed-form expressions for particle relative velocities induced by turbulence. *Astron. Astrophys.*, 466(2):413–420.

Ormel, C. W. and Spaans, M. (2008). Monte Carlo Simulation of Particle Interactions at High Dynamic Range: Advancing beyond the Googol. *Astrophys. J.*, 684(2):1291–1309.

Pérez, L. M., Isella, A., Carpenter, J. M., and Chandler, C. J. (2014). LARGE-SCALE ASYMMETRIES IN THE TRANSITIONAL DISKS OF SAO 206462 AND SR 21. *Astrophys. J.*, 783(1):L13.

Raettig, N., Lyra, W., and Klahr, H. (2013). A PARAMETER STUDY FOR BAROCLINIC VORTEX AMPLIFICATION. *Astrophys. J.*, 765(2):115.

Sato, T., Okuzumi, S., and Ida, S. (2016). On the water delivery to terrestrial embryos by ice pebble accretion. *Astron. Astrophys.* accepted

Seizinger, A. and Kley, W. (2013). Bouncing behavior of microscopic dust aggregates. *Astron. Astrophys.*, 551:A65.

Shakura, N. and Sunyaev, R. (1973). Black Holes in Binary System. Observational Appearance. *Astron. Astrophys.*, 24:337–355.

Simon, J. B., Beckwith, K., and Armitage, P. J. (2012). Emergent mesoscale phenomena in magnetized accretion disc turbulence. *Mon. Not. ...*, 18(March):18.

Takeuchi, T., Muto, T., Okuzumi, S., Ishitsu, N., and Ida, S. (2012). INDUCED TURBULENCE AND THE DENSITY STRUCTURE OF THE DUST LAYER IN A PROTOPLANETARY DISK. *Astrophys. J.*, 744(2):101.

van der Marel, N., van Dishoeck, E. F., Bruderer, S., Birnstiel, T., Pinilla, P., Dullemond, C. P., van Kempen, T. A., Schmalzl, M., Brown, J. M., Herczeg, G. J., Mathews, G. S., and Geers, V. (2013). A major asymmetric dust trap in a transition disk. *Science (80-.).*, 340(6137):1199–1202.

Wada, K., Tanaka, H., Okuzumi, S., Kobayashi, H., Suyama, T., Kimura, H., and Yamamoto, T. (2013). Growth efficiency of dust aggregates through collisions with high mass ratios. *Astron. Astrophys.*, 559:A62.

Wada, K., Tanaka, H., Suyama, T., Kimura, H., and Yamamoto, T. (2011). THE REBOUND CONDITION OF DUST AGGREGATES REVEALED BY NUMERICAL SIMULATION OF THEIR COLLISIONS. *Astrophys. J.*, 737(1):36.

Weidenschilling, S. (1980). Dust to planetesimals: Settling and coagulation in the solar nebula. *Icarus*, 44(1):172–189.

Weidenschilling, S. J. (1977). Aerodynamics of solid bodies in the solar nebula. *Mon. Not. R. Astron. Soc.*, 180(2):57–70.

Whipple, F. (1972). On certain aerodynamic processes for asteroids and comets. *From Plasma to Planet*, page 211.

Wisdom, J. and Tremaine, S. (1988). Local simulations of planetary rings. *Astron. J.*, 95:925.

Yabe, T. and Aoki, T. (1991). A universal solver for hyperbolic equations by cubic-polynomial interpolation I. One-dimensional solver. *Comput. Phys. Commun.*, 66:219–232.

Youdin, A. and Johansen, A. (2007). Protoplanetary Disk Turbulence Driven by the Streaming Instability: Linear Evolution and Numerical Methods. *Astrophys. J.*, 662(1):613–626.

Youdin, A. N. and Goodman, J. (2005). Streaming Instabilities in Protoplanetary Disks. *Astrophys. J.*, 620(1):459–469.

Youdin, A. N. and Lithwick, Y. (2007). Particle stirring in turbulent gas disks: Including orbital oscillations. *Icarus*, 192(2):588–604.